UNIVERSITÀ
DEGLI STUDI
DI PADOVA

Sede Amministrativa: Università degli Studi di Padova - Dipartimento di Ingegneria dell'Informazione

---

SCUOLA DI DOTTORATO DI RICERCA IN INGEGNERIA DELL'INFORMAZIONE
INDIRIZZO: Scienza e tecnologia dell'informazione
CICLO: XXVIII

RADIO COMMUNICATIONS USING ORBITAL ANGULAR MOMENTUM

Direttore della Scuola: Ch.mo Prof. Matteo Bertocco

Coordinatore d'indirizzo: Ch.mo Prof. Carlo Ferrari

Supervisore: Prof. Luca Palmieri

Dottorando: Fabio Spinello

There are only two possible outcomes: if the result confirms the hypothesis, then you've made a measurement. If the result is contrary to the hypothesis, then you've made a discovery.

– **Enrico Fermi**

God help us; we're in the hands of engineers.
– **Dr. Ian Malcolm - Jurassic Park**

Abstract

Orbital Angular Momentum (OAM) is a fundamental property of electromagnetic fields, associated to helicity of waves phase fronts. Like frequency and polarization, it represents a degree of freedom of an electromagnetic field and can be used for its identification. In fact, two waves with the same frequency but different OAM values can be distinguished from each other when their whole phase fronts are collected. Electromagnetic fields with nonzero OAM form an orthogonal basis and can be discriminated, without any digital post processing, at the physical layer. For this reason, they represent an interesting tool for the development of new multiplexing systems that better exploit the electromagnetic spectrum.

Within this context, this thesis presents the main results of theoretical and experimental studies on the application of OAM waves to radio multiplexing systems. It starts by considering the state-of-the-art of radio OAM waves, in order to identify features and applications concerning telecommunications. Then, it examines special parabolic antennas, also known as conformal antennas, that can generate and recognize electromagnetic waves at radio frequency with integer values of OAM. These antennas are then employed in practical experiments to test long-range multiplexing system prototypes, where three channels are transmitted and received on the same frequency and polarization state. The experiments study the difficulties of exploiting OAM modes orthogonality over long distances. In fact, due to diffraction, the size of field distributions increases more and more during propagation. Therefore, over long distances, it is necessary to use large antennas to collect their whole phase fronts. To overcome this problem and reduce the size of the received fields two interesting solutions are presented. The first one concerns a particular effect of field concentration that can be obtained superimposing electromagnetic waves with integer and consecutive values of OAM. The second one, on the contrary, studies the generation process for a special class of OAM fields, called higher order vortex beams, that are characterized by a more compact intensity distribution. Hence, the thesis considers the possibility of distinguish radio waves with different OAM values by receiving only a small portion of the phase fronts. This latter study, developed by using MIMO systems theory and theoretical models on OAM beams

propagation, focuses also in the comparison between general multiplexing systems based on today MIMO technology with the ones based on OAM waves. The analysis of long-range systems is then concluded by examining, both theoretically and experimentally, the superposition of waves with opposite values of OAM. These fields, in fact, are characterized by a more regular distribution and can be useful in simplifying the structure of OAM-based communication systems. In the end, the thesis considers short range communications where OAM waves are used not only for multiplexing purposes but also to increase, directly at the physical layer, the communication security.

Sommario

Il momento angolare orbitale, normalmente identificato con l'acronimo inglese OAM (Orbital Angular Momentum), é una proprietá fondamentale dei campi elettromagnetici legata alla loro distribuzione; campi con OAM diverso da zero sono infatti caratterizzati da intensitá a forma di ciambella e da fronti d'onda che si avvolgono a spirale. Al pari della frequenza, anche l'OAM rappresenta un grado di libertá di un'onda elettromagnetica e puó essere utilizzato per la sua identificazione. Infatti, due campi aventi la stessa frequenza ma diverso valore di OAM possono essere distinti quando i loro fronti d'onda vengono ricevuti interamente. Questa caratteristica fa sí che i campi elettromagnetici con OAM formino una base ortogonale e che possano essere distinti direttamente a livello fisico, senza il bisogno di post processing digitale. Le onde con OAM sono quindi particolarmente interessanti per lo sviluppo di nuovi sistemi radio multiplexing sia su lunga che su breve distanza, argomento esaminato sia teoricamente che sperimentalmente nella presente tesi.

Lo studio inizia con l'esame dello stato dell'arte sulle onde radio con OAM per individuarne caratteristiche ed applicazioni legate alle telecomunicazioni. Viene quindi studiato un particolare tipo di antenne paraboliche, dette anche "conformate", in grado di generare e di riconoscere onde radio con diversi valori di OAM. Usando queste antenne, viene quindi condotto uno studio sperimentale per valutare un prototipo di sistema multiplexing su lunga distanza, composto da tre canali isofrequenziali. L'esperimento evidenzia le difficoltá, precedentemente individuate nella fase di studio, riguardanti l'implementazione di un simile sistema. Durante la propagazione, infatti, i fronti d'onda si espandono a causa della diffrazione e risulta complicato riceverli interamente senza l'impiego di antenne ingombranti. Questo comporta una notevole difficoltá nello sfruttamento dell'ortogonalitá fra onde radio con OAM su lunghe distanze e costituisce un forte limite all'implementazione di un sistema multiplexing. Per ovviare a questo problema la tesi esamina tre possibili soluzioni. Nella prima considera un metodo per concentrare la distribuzione di un campo elettromagnetico con OAM mediante la sovrapposizione di modi interi e consecutivi. Nella seconda, studia la generazione di campi con OAM detti "di ordine superiore", (higher order vortex

beams), caratterizzati da una distribuzione di intensitá piú compatta. Nella terza, infine, esamina la possibilitá di distinguere due onde radio con diverso OAM mediante una ricezione parziale del loro campo elettromagnetico. Quest'ultima soluzione, analizzata mediante il formalismo dei sistemi MIMO e di modelli teorici sulla propagazione delle onde con OAM, consente anche di operare un confronto generale fra sistemi multiplexing basati sulle odierne tecniche MIMO e quelli basati su onde radio con OAM. Lo studio di sistemi a lunga distanza si conclude quindi esaminando le sovrapposizioni di campi elettromagnetici con valori opposti di OAM. Queste infatti, essendo caratterizzate da una distribuzione semplice e regolare, possono costituire un'interessante opzione per semplificare la struttura di sistemi di comunicazione basati su onde con OAM. Infine, nell'ultima parte, la tesi esamina sistemi multiplexing su breve distanza dove i campi elettromagnetici con OAM vengono utilizzati non solo per implementare un multiplexing ma anche per aumentare, direttamente a livello fisico, la sicurezza della comunicazione.

Contents

Introduction

Nowadays, electromagnetic (EM) waves are widely used in several contexts since they represent a fundamental resource for many application areas. They are profitably employed, for example, in industrial processes, in geo-location, in biomedical applications and especially in telecommunications. In particular, EM waves are the basis of wireless systems which are essential, by now, in everyday life. The use of such systems has increased more and more in recent years and the amount of information to be exchanged is always greater, especially with new smartphones. For this reason, scientists and engineers try to find new solutions to better exploit the electromagnetic spectrum. This is, in fact, the aim of new protocols and modulations techniques like OFDM, TDM, LTE, etc, which purpose is to boost the spectrum efficiency. This is also the goal of new MIMO systems, which are designed to take advantage on spatial diversity through the use of more and more complex antenna configurations [1].

Recently, another solution has been considered to overcome the saturation of frequency spectrum: a channel multiplexing technique based on the exploitation of electromagnetic waves carrying Orbital Angular Momentum [2, 3]. From fundamental physics [4], it is well known that an EM wave carries both linear and angular momentum. The linear momentum, proportional to the Poynting vector, is associated with the wave power and today radio systems are based on the exchange of this quantity. On the other hand, the angular momentum is composed by two contributions: Spin Angular Momentum (SAM) and Orbital Angular Momentum (OAM). The first one is related to wave polarization and it is already used to double the channel capacity; the second one, on the contrary, is associated with helicity of the wave phase front. OAM is a degree of freedom of an EM wave completely independent of frequency and polarization [5]. Therefore, it can be exploited to increase channel capacity since EM fields with different OAM values can propagate, in free space, without mutual interference. Moreover, they can be distinguished directly at the physical layer, without any post processing of the received signals, because OAM waves form a complete orthogonal basis [6]. Nevertheless, it must be underlined that to fully exploit the orthogonality property one has to receive the whole wave front, otherwise it can not correctly recognize

the transmitted OAM value [7, 8].

The use of OAM waves for channel multiplexing has already shown its potential at optical wavelength [9, 10]. In this domain, in fact, the EM fields are contained in small areas and it is easy to receive the entire field distributions in order to recognize the transmitted OAM values. While this requirement is reasonable at optical wavelengths, as proved in [9], it is more difficult to cope with at microwave frequencies [11, 12]. Therefore, the real efficiency of OAM-based multiplexing in the radio domain is still an open question.

The aim of this thesis is to continue, within this context, the investigation on OAM waves, with particular attention to their applications in the radio domain and for telecommunication purposes. More in detail, this work examines how OAM waves can be transmitted, manipulated and received in order to implement efficient multiplexing systems, both for long and short distances. The work, which presents new contributions on OAM-based communication area, is organized as follow:

the **fist chapter** contains an introduction on OAM fields. It looks at the huge literature on OAM waves examining the properties, the characteristics and the applications of such EM fields. It considers also the most common devices that transmit and receive OAM fields and the most important applications;

the **second chapter** examines conformal parabolic antennas that can be used for the generation and the reception of EM waves with an integer OAM quantity. The behavior and the characteristics of such devices are extensively studied by means of numerical simulations and experiments. Conformal parabolas are also used to experimentally verify, within the near field range, the separation between communication channels associated to different OAM modes, as a consequence of OAM waves orthogonality;

the **third chapter** reports an outdoor experiment in which conformal parabolic antennas are used to implement an OAM-based multiplexing system: a half duplex long range radio link, with three channels on the same frequency and polarization state. In a long range link, unless huge antennas are employed, it is complicated to receive the entire OAM field distributions and so to exploit OAM modes orthogonality. The target of the experiment is to investigate this issue in a practical way, searching also for possible solutions to overcome this problem;

the **fourth chapter** proposes a method that allows to reduce the size of an EM field with OAM. The method is based on the superposition of EM waves with integer and consecutive OAM values in order to concentrate the intensity distribution in a restricted domain and to embed a certain phase variation within the concentrated beam. This method may be useful to overcome the orthogonality exploitation difficulties on long range system, (like the one reported on chapter three), reducing the size of the received field;

the **fifth chapter** considers another way to reduce the size of an EM field with OAM: it examines higher order vortex beams which are characterized by an intensity distribution composed by concentric rings. In particular, the chapter focuses on the generation of such beams by means of

dielectric masks and conformal parabolae. Higher order beams are interesting because the main lobe of their field distributions is be more compact respect to other type of OAM waves;

the **sixth chapter** studies a new solution to implement an OAM-based multiplexing system: the discrimination of different OAM waves by measuring phase gradients over a limited part of the received field. Within this study also the techniques previously exposed in chapter three and four are examined, in order to quantify their efficiency in reducing the received field size. The mathematical models that are developed are finally employed to obtain one of the most important results of this thesis: a fair comparison between the performances of a generic OAM-based multiplexing systems and the ones of a MIMO-based multiplexing system;

the **seventh chapter** analyze the superpositions of EM waves with opposite values of OAM, which leads to simpler and more regular distributions of the EM fields. The use of such superpositions can simplify the structure of OAM-based communication systems;

the **eighth chapter** studies a near field communication system based on OAM waves. An experimental short range radio link, composed by circular arrays of patch antennas, is examined in order to determine the system performances with respect to antennas alignment. Moreover, the specific characteristics of OAM waves are applied to enhance the security level of communication directly at physical layer, without the use of digital processing.

In the end, the conclusions retraces all the topics that have been exposed highlighting the most important results.

Chapter 1

Theoretical background

In this chapter, a brief review of the main characteristics of electromagnetic waves with orbital angular momentum is proposed. OAM waves are examined from a theoretical point of view, in order to identify their properties and particularities. Within this frame, also some interesting mathematical tools to deal with OAM fields are presented. In the end, the most common devices that transmit and receive OAM fields are considered, together with their applications.

1.1 Historical overview

Electromagnetic (EM) waves are space disturbances that, originated from a source, propagates in time and space carrying both energy and momentum. Their discovery dates back to 1873: firstly they were theorized by James Clerk Maxwell [13] and afterwards they were experimentally detected by Heinrich Rudolf Hertz [14]. Thenceforth, the research on EM waves has evolved continuously and nowadays this property of the physical world is used and exploited in many applications: from medicine to geo-localisation. In particular, EM waves plays a crucial role on telecommunications: the need to exchange information is essential and EM waves are one of the most suitable and versatile tool to reach this purpose.

EM waves have been used in telecommunications, for the first time, by Guglielmo Marconi [15] to implement the wireless telegraph in 1895. Afterward, he introduced also the frequency division of the EM spectrum in order to have more than one communication channel at the same time. Since then, physicists and engineers focused their efforts on exploiting, always in a better way, the EM spectrum by considering different transmission techniques. Some examples [16] can be found considering analog and digital modulations, channel coding techniques, field polarization diversity and the Multiple Input Multiple Output (MIMO) technology which has become more and more important.

However, in recent times, another property of EM fields attracted the attention of telecommunication scientists: the *Orbital Angular Momentum* [17]. A complete description of this property, already discovered in 1936 [18] and exploited in optics since more than a decade [5], is presented below, together with some examples of its applications, especially for telecommunication purposes.

1.2 Electromagnetic waves

Electric and magnetic phenomena, in a non relativistic or non quantum context, can be fully described by the four Maxwell's equations [19]. They can be expressed, with respect to a Cartesian reference system $\mathbf{r} = (x, y, z)$ and at time t, as:

$$\nabla \cdot \mathbf{E}(\mathbf{r}, t) = \frac{\rho(\mathbf{r}, t)}{\epsilon} \tag{1.2.1}$$

$$\mu \nabla \cdot \mathbf{H}(\mathbf{r}, t) = 0 \tag{1.2.2}$$

$$\nabla \times \mathbf{E}(\mathbf{r}, t) = -\frac{\partial \mathbf{B}(\mathbf{r}, t)}{\partial t} \tag{1.2.3}$$

$$\mu \nabla \times \mathbf{H}(\mathbf{r}, t) = \mu \mathbf{J}(\mathbf{r}, t) + \mu \epsilon \frac{\partial \mathbf{E}(\mathbf{r}, t)}{\partial t} \tag{1.2.4}$$

where $\mathbf{E}(\mathbf{r},t)$ and $\mathbf{H}(\mathbf{r},t)$ are the electric and the magnetic fields, respectively. ϵ and μ are the dielectric and the magnetic constants while $\rho(\mathbf{r},t)$ and $\mathbf{J}(\mathbf{r},t)$ are charge and current densities, respectively.

If electric and magnetic fields are time dependent, they propagate through space as electromagnetic waves. This fact can be easily proved with straightforward algebra: the four Maxwell equation, for a time-varying field, can be properly combined to find the Helmholtz one, called also *wave equation*, which describes periodic phenomena both in time and space. Considering, for example, the electric field as independent variable it results that:

$$\nabla^2\mathbf{E}(\mathbf{r},t) = \mu\epsilon\frac{\partial^2}{\partial t^2}\mathbf{E}(\mathbf{r},t) \tag{1.2.5}$$

As stated before, an EM wave carries both energy and momentum [20, 21]. The energy is related with the capacity of the wave to make a work; it is a scalar quantity. On the contrary, the momentum is a vectorial quantity and can be of two types: Linear Momentum (LM) and Angular Momentum (AM). Moreover the AM is composed by two contributions: the Spin Angular Momentum (SAM) and the Orbital Angular Momentum (OAM). All these quantities are time dependent. However, when dealing with monochromatic fields of frequency equal to $\omega = 2\pi f$, it is meaningful to consider their averaged value by performing an integration average over a time period equal to $1/f$. From now on, dependence on time and space will be omitted for simplicity.

1.2.1 Energy and Linear Momentum

The energy carried by an EM field can be calculated starting from the *Poynting vector* which is defined as:

$$\mathbf{P} = \mathbf{E} \times \mathbf{H} \tag{1.2.6}$$

and describes the energy flux of an EM wave per surface and time unit. By its integration on a closed surface containing the field, it is possible to know the total energy carried by the wave:

$$W = \int_S \big(\mathbf{E} \times \mathbf{H}\big) \cdot \hat{\mathbf{n}} dS \tag{1.2.7}$$

On the other hand, as stated by fundamental physics [4], electromagnetic fields not only propagate by also interact with charged particles. To quantify these phenomena, it can be introduced a quantity called *linear momentum*, whose volumetric density $\mathbf{g}^{EM}$ is related to the Poynting vector by the Plank relation [22]:

$$\mathbf{g}^{EM} = \frac{\mathbf{P}}{c^2} = \epsilon\big(\mathbf{E} \times \mathbf{B}\big) \tag{1.2.8}$$

The electromagnetic linear momentum quantifies the force action of an EM field on charged particles, as the mechanical linear momentum quantify the action of a force on a body. In particular, the

interaction is regulated by the *continuity equation* [21] which links the variations of electromagnetic linear momentum $\mathbf{g}^{EM}$ with the ones of particles mechanical linear momentum $\mathbf{g}^{M}$:

$$\frac{\partial \mathbf{g}^{EM}}{\partial t} + \frac{\partial \mathbf{g}^{M}}{\partial t} + \nabla \cdot \mathbf{T} = 0 \tag{1.2.9}$$

where $\mathbf{T}$ is the Maxwell stress tensor which takes into account the interaction between electromagnetic forces and mechanical momentum of particles. It can be represented by a matrix whose elements are:

$$T_{i,j} = \epsilon E_i E_j + \frac{1}{\mu} B_i B_j - \frac{1}{2}\left(\epsilon |\mathbf{E}|^2 + \frac{1}{\mu}|\mathbf{B}|^2\right)\delta_{i,j} \tag{1.2.10}$$

where E_i and $B_i = \mu H_i$ are the components of electric field and magnetic field, respectively. On the other hand, $\nabla \cdot \mathbf{T}$ is a vector whose components can be calculated as the divergence of $\mathbf{T}$ columns. If an EM field is located within a volume V, its total linear momentum can be calculated as:

$$\mathbf{p}^{EM} = \int_V \mathbf{g}^{EM} dx^3 = \int_V \epsilon\big(\mathbf{E} \times \mathbf{B}\big)\, dx^3 \tag{1.2.11}$$

and, similarly, the conservation law within the same volume leads to:

$$\frac{\partial \mathbf{p}^{EM}}{\partial t} + \frac{\partial \mathbf{p}^{M}}{\partial t} + \int_S \mathbf{T} \cdot \hat{\mathbf{n}}\, dx^2 = 0 \tag{1.2.12}$$

The conservation law follows from Maxwell's equations. It states that if an EM field travels in a zone free of charge then the linear momentum (and so the field energy) are conserved during propagation. For this reason, the linear momentum is a suitable quantity for exchanging information. Present-day state-of-the-art radio science implementations are almost exclusively based on the principle of generating and detecting oscillating electric currents along a line, typically a linear dipole antenna, at the transmitter and the receiver, respectively. The dynamics of the electric charges, that constitute these currents, is determined by the interaction with EM generated and received fields as described by Eq. 1.2.12. The linear momentum radio technique has the advantage of being simple and easy to implement, but has also the drawback that each independent linear momentum transmission channel requires its own frequency and a finite bandwidth around it.

1.2.2 Angular Momentum

Also the *Angular Momentum* is related to the Poynting vector and to the energy flux of the EM field. However, it is appropriate to express its volumetric density in function of the linear momentum, in order to focus immediately on the connection between the two quantities. The angular momentum density $\mathbf{j}^{EM}$ is defined as [21]:

$$\mathbf{j}(\mathbf{r_0}) = \big(\mathbf{r} - \mathbf{r_0}\big) \times \mathbf{g}^{EM} = \big(\mathbf{r} - \mathbf{r_0}\big) \times \epsilon\big(\mathbf{E} \times \mathbf{B}\big) \tag{1.2.13}$$

where $\mathbf{r_0}$ is the origin of the reference system, (usually $\mathbf{r_0} = \mathbf{0}$), ad $\mathbf{r}$ is a general observation point. AM density is strictly dependent on the reference system origin.

From a practical point of view, the angular momentum is a quantity associated with rotational dynamics: it quantify the rotation action that an EM field have on a charged particle, analogously to the linear case. Also the angular momentum respects a continuity equation that, considering a field contained in certain volume, states that:

$$\frac{\partial \mathbf{j}^{EM}}{\partial t} + \frac{\partial \mathbf{j}^{M}}{\partial t} + \nabla \cdot \big((\mathbf{r} - \mathbf{r_0}) \times \mathbf{T}\big) = 0 \tag{1.2.14}$$

where $\mathbf{j}^M$ is the mechanical angular momentum of charged particles and $\mathbf{T}$ the Maxwell stress tensor. Similarly to the linear case, the total angular momentum of an EM field contained in a volume is:

$$\mathbf{J}^{EM} = \int_V \mathbf{j}^{EM} dV = \int_V \big(\mathbf{r} - \mathbf{r_0}\big) \times \epsilon\big(\mathbf{E} \times \mathbf{B}\big) dV \tag{1.2.15}$$

and the corresponding conservation law:

$$\frac{\partial \mathbf{J}^{EM}}{\partial t} + \frac{\partial \mathbf{J}^{M}}{\partial t} + \int_S \mathbf{K} \cdot \hat{\mathbf{n}} dx^2 = 0 \tag{1.2.16}$$

with $\mathbf{K} = (\mathbf{r} - \mathbf{r_0}) \times \mathbf{T}$. Also in this case $\mathbf{K}$ is a matrix whose elements are equal to:

$$K_{i,j} = \varepsilon_{ikl}(r - r_0)_k T_{l,j} \tag{1.2.17}$$

where $\varepsilon_{i,k,l}$ is the Levi-Civita symbol. This last equation states that also the angular momentum is conserved during propagation within space free of charges. For this reason, also AM is suitable for communication purposes: an example is given by the polarization diversity technique that exploits the AM conservation.

1.3 Angular momentum composition

The Angular Momentum, $\mathbf{J}^{EM} = \mathbf{S} + \mathbf{L}$, is composed by two contributions: the Spin Angular Momentum (SAM) $\mathbf{S}$ and the Orbital Angular Momentum (OAM) $\mathbf{L}$ [4, 20]. These two quantities are identical to the ones that can be found in a mechanical system and refer to revolution and rotation motions, respectively. In particular, the OAM quantity is associated with rotations around a center and depends on the reference system origin while the SAM is associated with revolutions.

SAM and OAM can be derived from the general AM definition. Considering the electric field $\mathbf{E}$ as independent variable and combining Eq. 1.2.13 with the Maxwell ones, it is possible to separate the components of the AM that not depends on the reference system origin, leading to the SAM expression [23]:

$$\mathbf{S} = \frac{\epsilon}{i\omega} \int_V \mathbf{E}^* \times \mathbf{E} dV \tag{1.3.1}$$

With a similar procedure, it is also possible to find the OAM expression [23]:

$$\mathbf{L}(\mathbf{r_0}=0)=\frac{\epsilon}{i\omega}\int_V \mathbf{E}^*\big(\mathbf{k}\times\nabla_{\mathbf{k}}\big)\mathbf{E}dV \tag{1.3.2}$$

where $\mathbf{k}$ is the wave vector.

In the following, it will be examined how these two quantities are connected with physical characteristics of EM fields.

1.3.1 AM of generic fields

A monochromatic EM field with an AM quantity different from zero can be described, in a cylindrical[1] reference system $\mathbf{r}=(\rho,\phi,z)$, highlighting its transversal longitudinal components, as [24]:

$$\mathbf{E}=\big(\alpha\hat{\mathbf{x}}+\beta\hat{\mathbf{y}}\big)E(\rho,z)e^{i\ell\phi}+\hat{\mathbf{z}}E_z \tag{1.3.3}$$

where α and β, that account for the field polarization in the (x,y) plane, can be used to determine the *polarization ratio* $\sigma=i\beta/\alpha$ parameter. The field propagates through $\hat{\mathbf{z}}$ and all its components along $\hat{\mathbf{x}}$, $\hat{\mathbf{y}}$ and $\hat{\mathbf{z}}$, satisfy the wave equation 1.2.5. The transversal field component $E(\rho,z)$ can be represented by means of an appropriate sum of plane waves, each one characterized by its wavenumber ξ, using the Angular Spectrum technique. More details about this mathematical tool can be found in Appendix A. It results that [24]:

$$E(\rho,z)=\int_0^k E(\xi)J_1(\xi\rho)\exp\big(i\sqrt{k^2-\xi^2}z\big)d\xi \tag{1.3.4}$$

where $k=2\pi/\lambda$ is the wavenumber of $E(\rho,z)$, $E(\xi)$ represents the plane wave in reciprocal space and $J_\ell(.)$ is the Bessel function of order ℓ. With straightforward algebra and considering that the field is in a space free of charges $(\nabla\cdot\mathbf{E}=0)$, the full field expression becomes:

$$\begin{aligned}\mathbf{E}=\int_0^k E(\xi)e^{i\ell\phi}\exp\big(i\sqrt{k^2-\xi^2}z\big)\cdot\Bigg(&\big(\alpha\hat{\mathbf{x}}+\beta\hat{\mathbf{y}}\big)J_1(\xi\rho)+\\&\hat{\mathbf{z}}\frac{\xi}{2\sqrt{k^2-\xi^2}}\Big[\big(i\alpha-\beta\big)e^{-i\phi}J_{\ell-1}(\xi\rho)-\big(i\alpha+\beta\big)e^{i\phi}J_{\ell+1}(\xi\rho)\Big]\Bigg)d\xi\end{aligned} \tag{1.3.5}$$

The time average energy carried by the field can be calculated as:

$$W=\frac{\pi\epsilon}{2}\int_0^k\frac{|E(\xi)|^2\big(2k^2-\xi^2\big)}{\xi\big(k^2-\xi^2\big)}d\xi \tag{1.3.6}$$

while the AM density can be determined from the time averaged Poynting vector as:

$$\mathbf{j}=\mathbf{r}\times\left(\epsilon\frac{\mathbf{E}\times\mathbf{B}^*}{2}\right) \tag{1.3.7}$$

[1] The same considerations can be done also in other reference systems. However, a cylindrical one allows to greatly simplify the calculations, without lose of generality.

Among all, the AM density $\hat{\mathbf{z}}$-component

$$j_z = \underbrace{\sum_{q=x,y,z} E_q^* \frac{\partial}{\partial \phi} E_q}_{OAM} + \underbrace{\left(E_x^* E_y - E_y^* E_x\right)}_{SAM} - \underbrace{\sum_{q=x,y,z} E_q^* \frac{\partial}{\partial x_q}\left(xE_y - yE_x\right)}_{OAM} \tag{1.3.8}$$

is particularly interesting for almost two reasons. First: it is the main and the most relevant since the field is propagating through $\hat{\mathbf{z}}$. Second: it is the only one in which an interaction between OAM and SPIN can be observed. On the contrary, the $\hat{\mathbf{x}}$ and $\hat{\mathbf{y}}$ components of AM density only depends on the SPIN.

OAM and SPIN densities can be identified by exploiting Eq. 1.3.1 to calculate the SPIN one. With the help of Fourier-Bessel integrals [25], the full densities components of OAM (l_z) and SPIN (s_z) along $\hat{\mathbf{z}}$ are equal to:

$$\begin{aligned} l_z &= \frac{\epsilon}{2i\omega} \int_0^\infty \int_0^{2\pi} \rho \left[\sum_{q=x,y,z} E_q^* \frac{\partial}{\partial \phi} E_q - \sum_{q=x,y,z} E_q^* \frac{\partial}{\partial x_q}\left(xE_y - yE_x\right) \right] d\rho d\phi \\ &= \ell \frac{\pi\epsilon}{2\omega} \int_0^k \frac{|E(\xi)|^2\left(2k^2 - \xi^2\right)}{\xi\left(k^2 - \xi^2\right)} d\xi + \sigma \frac{\pi\epsilon}{\omega} \int_0^k \frac{|E(\xi)|^2 \xi}{\left(k^2 - \xi^2\right)} d\xi \end{aligned} \tag{1.3.9}$$

$$s_z = \sigma \frac{\epsilon}{2i\omega} \int_0^\infty \int_0^{2\pi} \rho\left(E_x^* E_y - E_y^* + E_x\right) d\rho d\phi = \sigma \frac{\pi\epsilon}{2\omega} \int_0^k \frac{2|E(\xi)|^2}{\left(k^2 - \xi^2\right)} d\xi \tag{1.3.10}$$

Comparing Eq. 1.3.8 with Eq. 1.3.9 and 1.3.10 it is clear that the SAM contribution only depends on the field polarization by means of σ. Similarly, also the AM components j_x and j_y only depends on σ. On the contrary, since Eq. 1.3.9 contains both the σ and the ℓ terms, the OAM contribution is related with two properties of the field: polarization and phase front shape. In particular, the ℓ parameter characterizes the field phase dependence over the azimuthal coordinate describing a helical phase front.

In conclusion, while SAM is only related to field polarization, the OAM contribution depends on the entire field distribution.

1.3.2 AM for paraxial fields

The calculations just examined are quite different if the EM field is *paraxial*. This property concerns a particular evolution of the EM field during propagation in which the longitudinal components varies slowly with respect to the the transversal ones. From a mathematical point of view, this is equivalent to assume that the function $E(\rho, z)$ in Eq. 1.3.4 is sharply peaked for small values of ξ so that, in the integral process, all the values for which $\xi > k$ can be neglected. In other words, the field $E(\rho, z)$ can be expressed as a sum of plane waves all with wavenumber less or equal than k. As a consequence the field *z*-component is always weaker, at least of one order of magnitude, with respect to other ones, as shown in App. B. In order to measure if a field

is paraxial, it is possible to apply the so called *paraxial estimator*. This tool is used to calculate the *degree of paraxiality*, a parameter that for a fully paraxial field is equal to one while for a non paraxial field is equal to zero. Further details can be found in App. B.

Under the paraxial approximation, Eq. 1.3.9 and 1.3.10 considerably simplify, becoming [26]:

$$l_z = \ell \frac{\pi\epsilon}{2\omega} \int_0^k \frac{|E(\xi)|^2 \left(2k^2 - \xi^2\right)}{\xi\left(k^2 - \xi^2\right)} d\xi \tag{1.3.11}$$

$$s_z = \sigma \frac{\pi\epsilon}{2\omega} \int_0^k \frac{|E(\xi)|^2 \left(2k^2 - \xi^2\right)}{\xi\left(k^2 - \xi^2\right)} d\xi \tag{1.3.12}$$

Looking at Eq. 1.3.11, it is clear that, when dealing with paraxial fields, the OAM quantity only depends on the field phase distribution, in particular by its shape. The SAM, on the contrary, continue to depend only on field polarization. Because of this particular behavior, it is possible to construct a modified version of the Poincaré sphere [27] in order to classify the field properties with respect to the carried OAM quantity. Also the total AM z-component expression simplifies, becoming:

$$J_z = \frac{\ell + \sigma}{\omega} W \tag{1.3.13}$$

where W is the energy carried by the EM field calculated with Eq. 1.3.6.

All these relations are extremely important non only to understand the simplifications introduced by paraxiality but also to optimize numerical calculations: for paraxial fields the AM contributions can be easily determined only looking at the field polarization and at its phase front structure.

1.4 OAM fields example: LG beams

The simplest example of paraxial EM waves carrying a well defined quantity of OAM are *Laguerre-Gaussian* (LG) beams. They have been analyzed in 1992 by Allen et al. which proved, also experimentally, that they carry an integer OAM quantity [5]. LG beams are normally described, for simplicity, as approximated scalar fields, however, also a full vectorial expression can be found [28].

LG beams can be derived in several ways [29, 30]. The simplest is the scalar one which consist in combining Maxwell equations under the paraxial approximation [19]. In a Cartesian reference system $\mathbf{r} = (x, y, z)$, within a homogeneous medium, Maxwell equations for a monochromatic field polarized along $\hat{\mathbf{x}}$ can be combined to obtain Helmholtz equation (1.2.5)

$$\nabla^2 E(\mathbf{r}, t) = \mu\epsilon \frac{\partial^2}{\partial t^2} E(\mathbf{r}, t)$$

Now, it can be assumed that the electric field has the following expression:

$$E = A(x, y, z) e^{-ikz} e^{-i\omega t} \tag{1.4.1}$$

where $A(x, y, z)$ is the term describing the field intensity, $w = 2\pi f$ is the field frequency, $k = 2\pi/\lambda$ is the wave number and i the imaginary unit. Neglecting the time dependence and substituting Eq. 1.4.1 in Eq. 1.2.5 it results that:

$$\left(\nabla^2 + k^2\right)A = 0 \tag{1.4.2}$$

which can be transformed, with some algebra, in:

$$\left(\frac{\partial^2}{\partial x^2} + \frac{\partial^2}{\partial y^2} + \frac{\partial^2}{\partial z^2}\right)A(x, y, z) - 2ik\frac{\partial A(x, y, z)}{\partial z}e^{-ikz} = 0 \tag{1.4.3}$$

The *paraxial approximation* must now be applied. It consist in supposing that the longitudinal components of the field varies more slowly than the transversal ones. This hypothesis is not purely theoretical since such EM field can be found when dealing with lasers. The paraxial approximation can be expressed as:

$$\frac{\partial^2}{\partial z^2}A(x, y, z) \ll k\frac{\partial A(x, y, z)}{\partial z} \tag{1.4.4}$$

which equals to neglect the $\frac{d^2}{dz^2}$ term in Eq 1.4.3. In such a way, a new wave equation called *Paraxial Helmholtz Equation* can be obtained:

$$\left(\frac{\partial^2}{\partial x^2} + \frac{\partial^2}{\partial y^2}\right)A(x, y, z) - 2ik\frac{\partial A(x, y, z)}{\partial z}e^{-ikz} = 0 \tag{1.4.5}$$

Since LG beams are characterized by a circular symmetry, it is necessary to use a cylindrical reference system $\mathbf{r} = (\rho, \phi, z)$ in which the Paraxial wave equation becomes:

$$\left(\frac{\partial^2}{\partial \rho^2} + \frac{1}{\rho}\frac{\partial}{\partial \rho} - 2ik\frac{\partial}{\partial z} - \frac{1}{\rho^2}\frac{\partial^2}{\partial \phi^2}\right)A(\rho, \phi, z) = 0 \tag{1.4.6}$$

and also to use a new ansatz for the electric field distribution:

$$E(\rho, \phi, z) = A(\rho, \phi, z)e^{-ikz} = A\left(\frac{\rho}{w(z)}\right)e^{-i\left(P(z) + \frac{k\rho^2}{2q} + \ell\phi + kz\right)} \tag{1.4.7}$$

The full electric field expression for LG beams is obtained combining combining Eq. 1.4.7 within Eq. 1.4.6:

$$E_{p,\ell}(\rho, \phi, z) = \frac{w_0}{w(z)}e^{-\frac{\rho^2}{w^2(z)}}\left(\frac{\sqrt{2}\rho}{w(z)}\right)^{|\ell|} \cdot L_n^{|\ell|}\left(\frac{2\rho^2}{w^2(z)}\right) \cdot \Phi \tag{1.4.8}$$

where the field phase term is equal to:

$$\Phi = \exp\left[-i\left(P(z)\frac{k\rho^2}{2q} + \ell\phi - \left(2P(z) + |\ell| + 1\right)\arctan\left(\frac{kz}{w_0^2}\right)\right)\right] \tag{1.4.9}$$

The parameters of Eq. 1.4.8 are responsible for the field distribution. In particular, $w(z)$ quantify the beam width at different propagation length from origin, z_R is the Rayleigh distance (the range

within which the field has its minimum divergence) [31], $R(z)$ is the field front curvature radius, $\phi(z) = \arctan(z/z0)$ is the Gouy phase [32, 33] and $L_n^{|\ell|}(.)$ the generalized Laguerre polynomial. The parameter p is the so called *radial index* that, acting on the LG polynomial, determine the number of radial nodes of the beam intensity.

As can be noticed, the peculiarity of such beams can be found in the phase expression that linearly depends on the azimuthal coordinate, ϕ, as expressed in the term $exp(-i\ell\phi)$. This implies that such beams have a spiral phase front with the parameter ℓ, called *azimuthal index*, that determines the number of arms of the spiral and that is also equal to the OAM quantity carried by the beam [30]. The particular shape of the phase front and the characteristic doughnut intensity distribution can be observed in Fig. 1.1 for different values of ℓ. From Fig. 1.1, it is also clear

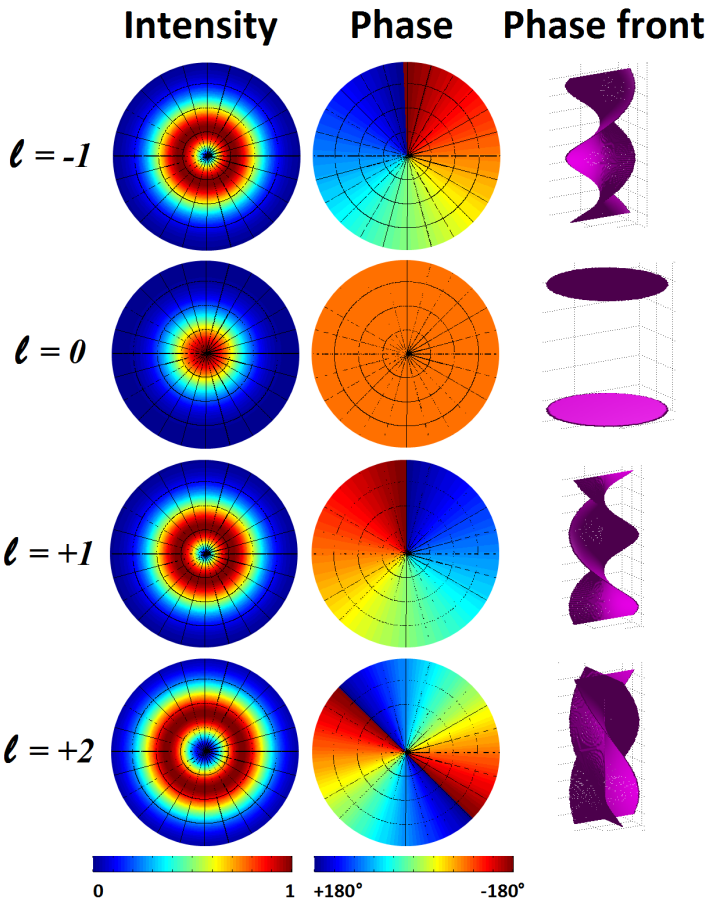

Figure 1.1: Intensity and phase distributions of LG beams with different values of ℓ.

that the helical phase front is responsible for the null intensity in the center on the field. In fact, in this point, the field phase assume, at the same time, all the values between 0 and 2π radiant.

For this reason, such point is called *singularity* and the whole beam is also called *vortex beam* [34]. The singularity represent a sort of physical paradox that, however, is simply resolved by nature keeping in its correspondence a field null [35]. The OAM value ℓ determine the size of the singularity since it controls the number of times that the phase assume all the values between 0 and 2π in the center of the beam. Moreover, also the field maximum intensity position r_{max} is controlled by ℓ:

$$r_{max} = w(z)\sqrt{\frac{\ell}{2}} \tag{1.4.10}$$

as can be easily deduced calculating the derivative of Eq. 1.4.8 with respect to ρ.

1.4.1 The singularity concept

The concept of singularity was introduced in 1974, for the first time, by Michael Berry and John Nye. They worked on a new description of waves and propagation studying, in particular, the so called *wavefront dislocations* [36, 37, 38]. Literally, they described singularities as:

"places where mathematical quantities become infinite, or change abruptly. In waves - of light, for example - there can be singularities in the intensity, in the phase, or in the polarization. This is a modern view, sharply different from the traditional approach where waves were simply the solutions of wave equations, and singularities - if considered at all - were regarded as awkward places where the usual treatments fail"

Berry and Nye classified also the dislocations type as: screw dislocations, edge dislocations or mixed dislocations (screw-edge). Naturally, the name depends on the shape of dislocation. For example, the LG beams are characterized by a screw phase dislocation but there are also other EM waves in which the phase singularities lie on a lines or on a planes, resulting in edge dislocations; an example is given by the superposition of opposite-sign OAM beams (Chap. 7). Sometimes, it is possible to find also mixed singularities type.

1.5 General paraxial OAM beams

LG beams are not the only description of paraxial EM fields carrying an integer quantity of OAM. Other expressions can be found in [39, 40, 41, 42], like Kummer beams, Hypergometrig Gaussian beams, Bessel beams, etc. In general, the electric field of a vortex beam, propagating along $\hat{\mathbf{z}}$ in a cylindrical reference system $\mathbf{r} = (\rho, \phi, z)$, can be described as:

$$\mathbf{E}(\mathbf{r}) = \mathbf{A}(\mathbf{r})e^{-i\ell\phi}\sigma e^{kz} \tag{1.5.1}$$

where $\mathbf{A}(\mathbf{r})$ is the field amplitude factor (also accounting for the field polarization) while k is the wave number. The fundamental fact is that the field description of any vortex beam always contains the factor $e^{-i\ell\phi}$, accounting for the OAM contribution, while the amplitude factor $\mathbf{A}(r)$

changes depending on the particular beam type that is considered. All these OAM beams are characterized by a similar structure of the Poynting vector, which can be calculated as [43, 44]:

$$P_\rho = \epsilon \frac{\omega k \rho z}{z^2 + z_r^2} \left|\mathbf{A}(\mathbf{r})\right|^2 \tag{1.5.2}$$

$$P_\phi = \epsilon \left[\frac{\omega \ell}{\rho} \left|\mathbf{A}(\mathbf{r})\right|^2 - \frac{1}{2} \omega \sigma \frac{\partial \left|\mathbf{A}(\mathbf{r})\right|^2}{\partial \rho} \right] \tag{1.5.3}$$

$$P_z = \epsilon \omega k \left|\mathbf{A}(\mathbf{r})\right|^2 \tag{1.5.4}$$

where ω is the field frequency and z_r the Rayleigh distance. The first component, along $\hat{\rho}$, relates to the spread of the beam during propagation. It depends only on $|\mathbf{A}(\mathbf{r})|$ so beams with different intensity distributions will spread with different rates. On the contrary, the second component, along $\hat{\phi}$, accounts for the rotational behavior of the energy flux. In this case, it depends not only on the intensity distribution but also on the OAM quantity carried by the beam and on the field polarization. In the end, the $\hat{\mathbf{z}}$ Poynting component, namely the linear momentum component along the propagation direction, is similar in behavior to the first one.

From the linear momentum density distribution, it is simple to calculate also the Angular Momentum z-componet using Eq. 1.2.13. The AM density is equal to:

$$j_z = \epsilon_0 \left[\omega \ell \left|\mathbf{A}(\mathbf{r})\right|^2 - \frac{1}{2} \omega \sigma \rho \frac{\partial \left|\mathbf{A}(\mathbf{r})\right|^2}{\partial \rho} \right] \tag{1.5.5}$$

and when integrated over the whole cross section of the beam

$$\frac{J_z}{W} = \frac{\int j_z \rho d\rho d\phi}{\int g_z \rho d\rho d\phi} = \frac{\ell + \sigma}{\omega} \tag{1.5.6}$$

it gives the general expression of Eq. 1.3.13.

1.6 OAM beams orthogonality

Beams carrying different quantities of Orbital Angular Momentum can be distinguished from each other like classical EM waves with different frequencies. In fact, because of the presence of the $e^{-i\ell\phi}$ term, OAM beams form an orthogonal set. Keeping the cylindrical reference system $\mathbf{r} = (\rho, \phi, z)$ previously introduced, it is easy to prove that, for $\ell_1 \neq \ell_2$:

$$\langle \mathbf{E}_{\ell_1} | \mathbf{E}_{\ell_2} \rangle = \int_0^\infty \int_0^{2\pi} \mathbf{E}_{\ell_1} \mathbf{E}^*{}_{\ell_2} \rho d\rho d\phi = \int_0^\infty \int_0^{2\pi} A_1(\rho) A_2(\rho) e^{-i\ell_1\phi} e^{i\ell_2\phi} \rho d\rho d\phi = 0 \tag{1.6.1}$$

As can be observed from Eq. 1.6.1, the orthogonality property can be exploited only if the entire azimuthal fields distributions is considered. In fact, the integration domain for the ϕ coordinate is $0 \rightarrow 2\pi$. OAM beams orthogonality is a direct consequence of sine and cosine trigonometric

functions orthogonality, (remember that $\exp(i\phi) = \cos(\phi) + i\sin(\phi)$), which can be exploited only considering the functions within a period. Moreover, the two field must share the same reference system and must be properly aligned in order that the $\exp(.)$ terms can be factored.

Since OAM beams form a complete orthogonal set [6], they can be used to describe a generic EM field. This technique, similar to the angular spectrum representation where the set is composed by orthogonal plane waves, is called *spiral spectrum representation*.

1.6.1 Spiral spectrum for scalar paraxial fields

A scalar paraxial field, propagating through $\hat{\mathbf{z}}$ in a cylindrical reference system $\mathbf{r} = (\rho, \phi, z)$, can be expressed by an appropriate sum of spiral harmonics (OAM modes) $\exp(i\ell_n\phi)$ [45]:

$$E(\rho, \phi, z) = \frac{1}{\sqrt{2\pi}} \sum_{n=-\infty}^{+\infty} a_n(\rho, z) e^{i\ell_n \phi} \tag{1.6.2}$$

where the $a_n(\rho, z)$ terms are complex amplitude factors. Their values can be determined, by using the properties of orthogonal basis, projecting the field in the corresponding harmonic:

$$a_n(\rho, z) = \frac{1}{\sqrt{2\pi}} \int_0^{2\pi} E(\rho, \phi, z) e^{-i\ell_n \phi} d\phi \tag{1.6.3}$$

The $a_n(\rho, z)$ coefficients determine the energy of each spiral harmonic within the spectrum which can be computed as:

$$W_n = \int_0^{\infty} \rho \left| a_n(\rho, z) \right|^2 d\rho \tag{1.6.4}$$

For this reason, applying Parseval theorem [46], the total energy carried by the field can be calculated as:

$$W = \sum_{n=-\infty}^{\infty} W_n = \sum_{n=-\infty}^{\infty} \int_0^{\infty} \rho \left| a_n(\rho, z) \right|^2 d\rho \tag{1.6.5}$$

where the relative weight of each harmonic is: $P_n = W_n/W$. An example of spiral spectrum decomposition for a generic EM field is shown in Fig. 8.5.

The spiral spectrum technique can be useful also to determine the exact OAM composition of a generic field. For this reason, it allows to calculate the z-component of the OAM [45] as:

$$L_z = \frac{2\epsilon}{\omega} \sum_{n=-\infty}^{\infty} n W_n \tag{1.6.6}$$

To correctly calculate the OAM spectrum it is fundamental to consider the whole field distribution, similarly to the exploitation of the orthogonality property. The reason can be found looking at the integral in Eq. 1.6.3 where the ϕ variable must be considered in all its domain [7, 47] together with the entire distribution of the electric field. Moreover, since OAM is a quantity that depends not only on the field distribution but also by the observation point [48, 49], it is fundamental to keep the

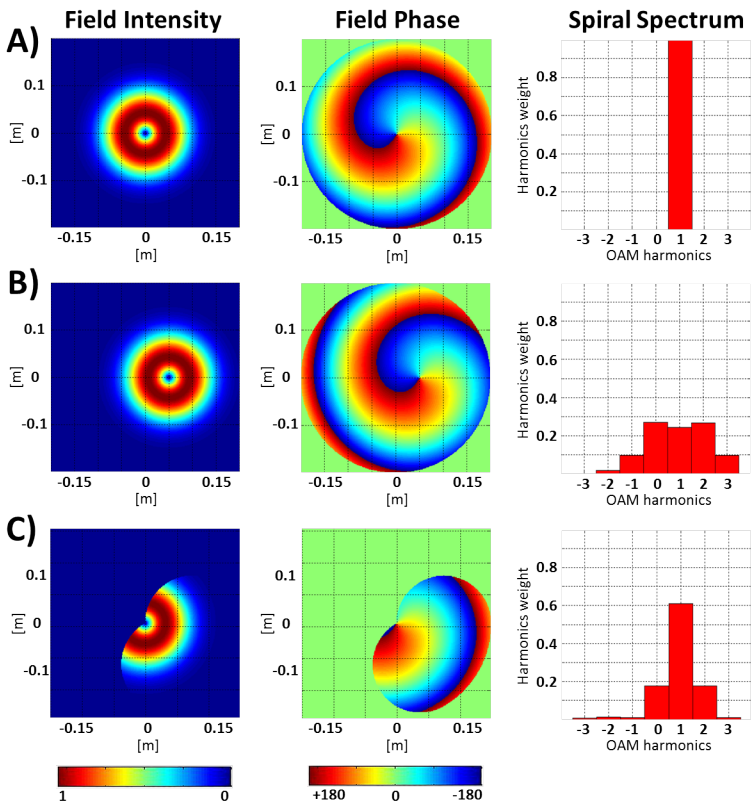

Figure 1.2: Spiral Spectrum calculation of: A) an $\ell = +1$ OAM beam, B) a translated $\ell = +1$ OAM beam, C) a partial $\ell = +1$ OAM beam.

field properly aligned with the reference system used by the spiral spectrum algorithm. Examples of erroneous spiral spectrum calculations due to a partial field consideration or misalignment are reported in Fig. 8.5.

1.6.2 OAM spectrum for vectorial non paraxial fields

The spiral spectrum calculation for vectorial non paraxial fields, (generic EM fields), is more complicate with respect to the previous case since, this time, the field is no more composed by a single component. Similarly to the previous algorithm, it is useful to consider the field distribution on a plane perpendicular to its propagation direction $\hat{\mathbf{z}}$ keeping the same cylindrical reference system. The field distribution on a $z = const.$ plane can be described as [50]:

$$\mathbf{E}(\rho, \phi) = F(\rho, \phi)\mathbf{e_1}(\phi) + G(\rho, \phi)\mathbf{e_2}(\rho, \phi) \tag{1.6.7}$$

where $F(\rho,\phi)$ and $G(\rho,\phi)$ are complex factors while $\mathbf{e_1}(\phi)$ and $\mathbf{e_2}(\rho,\phi)$ are unitary vectors accounting for a purely transversal and a purely longitudinal component, respectively. The two components can be expressed by means of spiral harmonics [50]:

$$F(\rho,\phi)=\frac{1}{\sqrt{2\pi}}\sum_{n=-\infty}^{\infty}f_n(\rho)e^{in\phi}$$
$$G(\rho,\phi)=\frac{1}{\sqrt{2\pi}}\sum_{n=-\infty}^{\infty}g_n(\rho)e^{in\phi} \tag{1.6.8}$$

where

$$f_n(\rho)=\frac{1}{\sqrt{2\pi}}\int_0^{2\pi}F(\rho,\phi)\exp(-in\phi)d\phi$$
$$g_n(\rho)=\frac{1}{\sqrt{2\pi}}\int_0^{2\pi}G(\rho,\phi)\exp(-in\phi)d\phi \tag{1.6.9}$$

leading to a new field expression by means of spiral harmonics:

$$\mathbf{E}(\rho,\phi)=\frac{1}{\sqrt{2\pi}}\left[\sum_{n=-\infty}^{\infty}f_n(\rho)e^{in\phi}\mathbf{e_1}(\phi)+\sum_{n=-\infty}^{\infty}g_n(\rho)e^{in\phi}\mathbf{e_2}(\rho,\phi)\right] \tag{1.6.10}$$

Similarly to the previous case, the field energy can be calculated as:

$$W=\frac{1}{8\pi k^2}\int_0^1\int_0^{2\pi}\sum_{n=-\infty}^{\infty}\left[\left|f_n(\rho)\right|^2+\left|g_n(\rho)\right|^2\right]\rho d\rho d\phi \tag{1.6.11}$$

where the ρ integration domain depends on the particular definition of the $\mathbf{e_1}(\phi)$ and $\mathbf{e_2}(\rho,\phi)$ [50]. Since for generic fields the AM contributions may not be separated, it is not possible to calculate a single Spiral Spectrum as in the paraxial case but only to observe the spiral harmonics composition of the longitudinal and of the transversal components of the field. This decomposition can again be useful to determine the AM z-component as [50]:

$$\begin{aligned}J_z=&\frac{1}{\omega}\sum_{n=-\infty}^{\infty}n\int_0^1\left[\left|f_n(\rho)\right|^2+\left|g_n(\rho)\right|^2\right]\rho d\rho+\\&+\frac{1}{\omega}\sum_{n=-\infty}^{\infty}\int_0^1\left[\left|f_n(\rho)\right|^2-\left|g_n(\rho)\right|^2\right]\left(\frac{\rho^2}{2\sqrt{(1-\rho^2)}}+1\right)\rho d\rho\end{aligned} \tag{1.6.12}$$

1.7 OAM beams generation

In this section, the main devices that are used to generate OAM waves in the radio domain are examined. Several solutions, as spiral phase masks, drilled masks or fork holograms, have been firstly developed in optics where OAM fields are used from more time and, at a later stage, adapted to the radio domain. Moreover, all the devices that are presented are reciprocal and can be used not only to generate but also to receive OAM waves.

1.7.1 Spiral phase mask

A Spiral Phase Mask (SPM), Fig. 1.3, is a dielectric device whose purpose is to imprint a fixed OAM quantity to an EM field [51]. To understand its behavior it is useful to adopt a ray optics model. Each input ray impinge the mask surface on a different point and travel along a different path within the mask. Since its thickness is not constant, each ray emerge after a different time, depending on its azimuthal position. Within the mask, the rays velocity is different from the outside and controlled by the mask refractive index n_m. So, by controlling the spiral height and the refractive index n_m, it is possible to imprint an azimuthal phase pattern identical to the one of an OAM beam [52].

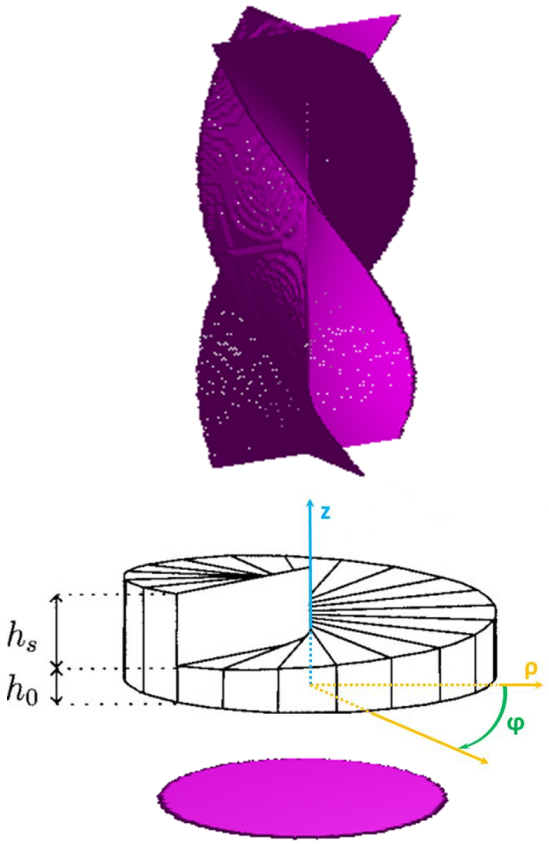

Figure 1.3: Example of a spiral phase mask. Source: [52].

The mask shape can be described, in a cylindrical reference system $\mathbf{r} = (\rho, \phi, z)$ as:

$$z(\rho, \phi) = \Big(h_s \frac{\phi}{2\pi} + h_0\Big)\Theta(\rho) \tag{1.7.1}$$

where $\Theta(x)$ is a step function equal to 1 if $x < \tilde{r}$ and to 0 otherwise; it is necessary to limit the

radial extension of the mask to $\tilde{r}$. The quantities h_0, h_s, shown in Fig. 1.3, quantify the minimum and the maxim spiral height, respectively. h_s has to be modified depending on the desired OAM value to be imprinted:

$$h_s = \frac{\ell\lambda}{\Delta n} = \frac{\ell\lambda}{\sqrt{\epsilon_m} - \sqrt{\epsilon_0}} \tag{1.7.2}$$

where ℓ is the desired OAM quantity and Δn is the difference between mask and air refraction indexes. Eq. 1.7.2 can be easy obtained considering the expression of the propagation velocity of rays into the mask and the air, respectively, and the relation between refraction index and dielectric constant: $n = \sqrt{\epsilon}$.

SPM can be used to generate OAM beams by converting input plane waves into OAM ones and also for the opposite process. They can be employed both in radio [53] and optics [54].

1.7.2 Drilled phase mask

Drilled masks are dielectric devices designed to imprint, once again, a fixed OAM quantity to an EM field. They are, however, quite different from spiral masks because of their planar geometry (Fig. 1.4). These particular tools are obtained drilling a planar dielectric surface with a specific

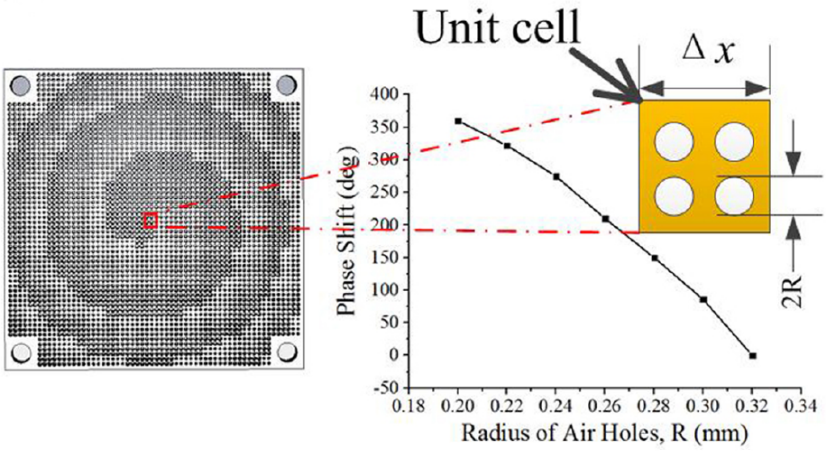

Figure 1.4: On the left: example of a drilled mask designed to generate a $\ell = +1$ OAM field. On the right: detail of a cell of the drilled mask. Source: [55].

pattern in order to change, locally, its refraction index n. Since the propagation velocity of an EM field depends on n, it is possible to induce local phase delays to the EM field impinging the mask, thus imprinting a particular field phase front [55].

To better understand this behavior, an example is shown in Fig. 1.4. The mask is divided in little square cells, each characterized by four holes. Each cell acts like a pixel in a digital image and represents the minimum unit with controllable refraction index n_{cell}. To change n_{cell}, it

is sufficient to act on the holes diameter. Up to now, however, it is not possible to derive with an analytical expression the cell's refraction index with respect to its geometry; numerical simulations are necessary.

To design a mask that imprint an integer OAM quantity it is fundamental to induce, in the impinging field, a linear phase delay in the azimuthal direction. For this reason, cells with the same refraction index must be radially placed. On the contrary, the cells placed in the azimuthal direction must vary their refraction index from a minimum to a maximum value, depending on the desired OAM value.

1.7.3 Conformal parabolic antennas

OAM radio waves can be produced also using suitably modified parabolic antennas called *conformal* antennas. It is well known, in fact, that a standard parabolic antenna is composed by two main elements: a feeder and a reflector. The feeder, typically a little horn or similar, generates a field with spherical phase fronts that is focused, towards infinity, by the reflector. In such a way, the feeder field is converted into a plane wave. Conformal parabolic antennas, on the contrary, are characterized by a modified parabolic reflector, which is deformed to assume a screw shape. An example of a conformal off axis parabolic reflector is shown in Fig. 1.5. Helical parabolic reflectors

Figure 1.5: A conformal off axis parabolic reflector. Source: [56].

are designed to impinge to the feeder field a desired quantity of OAM. Their behavior is similar to the one of dielectric masks: the surface of the reflectors is deformed to cause local delays in the field propagation and so to induce the desired phase pattern. An accurate analysis of conformal parabolic prime focus antennas is reported in Chap. 2.

1.7.4 Fork holograms

Another way to produce OAM waves is by means of holograms [57, 58]. Holograms are synthetic images of objects, generated by an interference process, as depicted in Fig. 1.6. They was introduced, for the first time, in 1948 by Gabor [59] in optics, however, they can be used also in radio [60]. An image hologram of a generic object is obtained by the interference between a

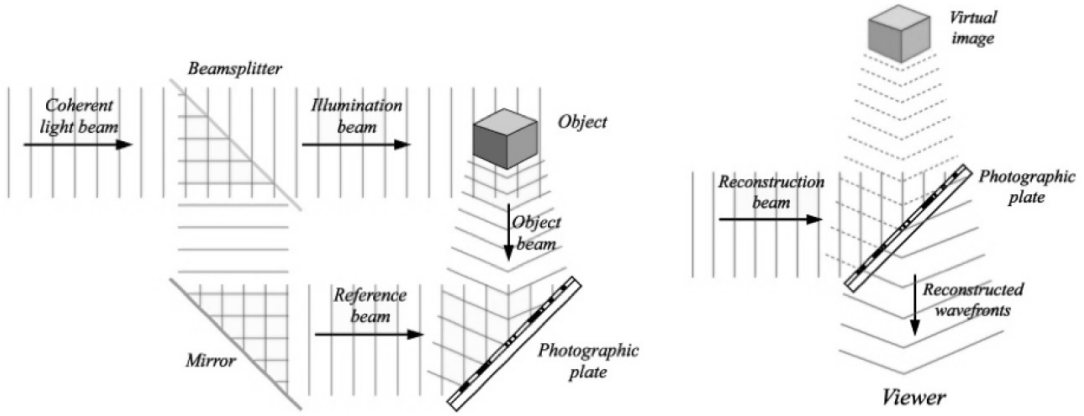

Figure 1.6: On the left: hologram generation process. On the right: reconstruction of an image by means of an hologram. Source [61].

reference plane wave and by the one scattered by the object, (Fig. 1.6). Thus, when the hologram is illuminated with a proper wave, the image of the object will be reproduced. Because of their behavior, holograms are classified as diffractive devices.

A hologram generation can be made also usign a virtual object. It is sufficient to simulate the image to be reproduced by means of computer calculations and so to directly determine the interference patter. In such a way, holograms can be employed to generate images of not existing object and hence also to reproduce EM fields with a desired distributions. Further information about holograms synthesis can be found in [62, 63].

Computer generated holograms (CGH) used to produce OAM fields are characterizes by a fork dislocation and, for this reason, are called *fork-holograms* (FH). An example can be observed in Fig. 1.7. When a FH is perpendicularly illuminated by a plane wave it produces m different diffraction orders, whose propagation directions form an angle α_m with respect to the incident field direction. Moreover, each order carries a different OAM quantity and is described as:

$$\Gamma \sin(\alpha_m) = m\lambda \tag{1.7.3}$$

with λ the field wavelength and Γ the FH grating spatial period.

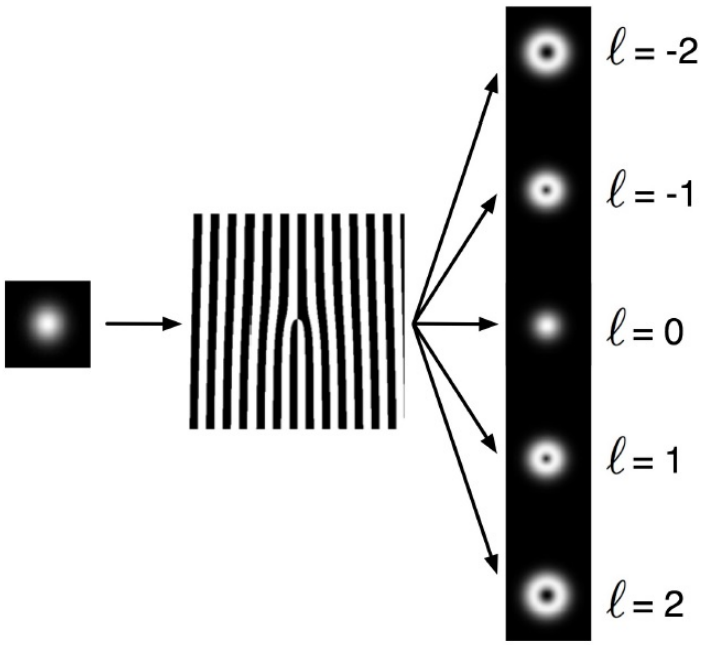

Figure 1.7: Example of a fork hologram for the generation of OAM waves. When illuminated by a plane wave, a FH generates various beams with different quantities of OAM. Source [61].

As example of FH synthesis, it can be considered the interference between an OAM wave and a planar one. For simplicity, the two waves are referred to Cylindrical (ρ, ϕ, z) and Cartesian (x, y, z) coordinates, respectively. In particular, the planar wave propagates through the (x, y) plane, as the OAM one:

$$u_{oam}(\rho, \phi, z) = A \exp(i\ell\phi) \tag{1.7.4}$$

$$u_{pl}(x, y, z) = B \exp(-\frac{i2\pi x}{\Gamma}) \tag{1.7.5}$$

A and B are amplitude coefficients while ℓ is the OAM value. The interference process, assuming $A = B$, results in the hologram pattern whose intensity is described by:

$$I(x, \phi) = \left|u_{OAM} + u_{PL}\right|^2 = 2A^2 \left[1 + \cos\left(\frac{2\pi x}{\Gamma} + \ell\phi\right)\right] \tag{1.7.6}$$

1.7.5 Circular antenna array

EM fields with OAM can be generated and received by means of antennas array [2, 64]. In particular, circular arrays are preferred [65] especially for their similarity with the circular intensity shape of OAM beams. To generate an EM wave with an OAM quantity equal to ℓ, a circular array,

centered in a cylindrical reference system $\mathbf{r} = (\rho, \phi, z)$, must be composed by N_a antennas:

$$N_a > 2\ell + 1 \tag{1.7.7}$$

Eq. 7.2.3 is the Nyquist sampling theorem applied to the angular space domain described by the ϕ variable; it ensures that the phase profile $\exp(i\ell\phi)$ is correctly reproduced [66]. Moreover, two conditions on the antennas feed signals must be fulfilled. First: all signals must be equal in amplitude. Second: the signals of two adjacent antennas must be out of phase of $2\pi\ell/N_a$. In other words, called ϕ_n the azimuthal position of the n-th radiating elements, its phase term must be equal to $\exp(i\ell\phi_n)$. An example of antennas arrays, set to generate $\ell = 1$ and $\ell = 2$ fields, are shown in Fig. 1.8 together with the generated radiation patterns. As can be noticed, the field

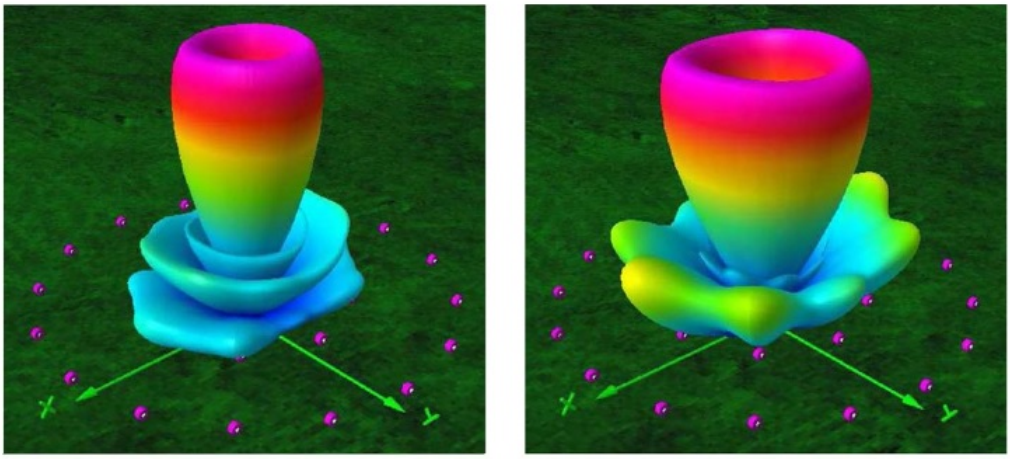

Figure 1.8: Generation of an $\ell = +1$ (left) and an $\ell = +2$ (right) OAM field by means of a circular arrays composed by dipole antennas. Source [66].

distributions contains secondary lobes. For this reason, antennas arrays ca be used to produce only approximated versions of LG beams and not their exact field distributions.

Intensity and geometry of primary and secondary lobes can be controlled by changing the array radius and the number of radiating elements, as suggested by traditional array theory [67]. Moreover, the paraxiality degree of the main lobe can be ensured by taking the array diameter greater than λ, (see App. A).

OAM arrays can be implemented with different radiating elements, from patch antennas [68, 69] to Vivaldi ones [70]. Also the feeding networks, necessary to generate the right phase delays, can be developed with different technologies. It is possible to act on the structure of the guiding elements [71] or to introduce signal delays [72] or to use microwave photonics techniques [73, 74, 75]. In the end, notice also that the behavior of circular arrays can be imitated with slot-antennas characterized by a circular structure, as [76].

1.7.6 Other methods

Up to now, the most used techniques to generate and receive OAM beams in the RF domain have been examined. However, it necessary to mention also other two methods, not used in radio yet. The fist is represented by Q-plates [77, 78], which are non homogeneous dielectric masks. The second is the conversion of Hermite-Gauss beams into Laguerre-Gauss ones [79, 80] by means of cylindrical lenses. These techniques are not adopted in RF because of scaling problems; a future technology improvement can, however, make them suitable.

1.8 OAM waves and telecommunications

Nowadays, telecommunication systems are essential to everyday life and the amount of exchanged information is growing continuously. For this reason, it is necessary to find better ways to exploit the electromagnetic (EM) spectrum. An interesting way consists in implementing a channel multiplexing scheme based on OAM waves [2, 3]. The main reason of this particular interest is OAM modes orthogonality that, in principle, allows channel discrimination directly at the physical layer, without post processing of the received signals. Up to now, however, OAM based multiplexing is still under examination [81, 82, 83, 84, 85], no commercial applications are available.

1.8.1 Experimental solutions for the optical domain

An interesting experiment on the use of OAM modes for optical multiplexing has been performed in 2012 by Wang et al [9]. Four monochromatic lasers, each one modulated with a different information channel, were transformed in four different OAM beams. The transformation process was made by using Spatial Light Modulators (SLM) [86] which can be considered as computer reconfigurable phase masks. The four laser beams were then combined into a single beam which was propagated in free space for 1m. Hence, the beam was split and each OAM channel was recovered by using other SLM, configured as inverse phase masks. In this way, the information carried by the four channels was recovered. In the end, the signal quality of each channel was evaluated by means of digital post processing. An overview of the experimental setup can be found in Fig. 1.9.

This experiment is particularly interesting for many reasons. First, it proves the feasibility of free space optical OAM-based channels multiplexing. Second, it allows to evaluate the OAM beams structure modification during free space propagation. Third, it allows to estimate the performances of an optical OAM-based multiplexing system.

Also other multiplexing experiments have been performed [87, 88, 89] to explore the potentiality of OAM multiplexing. In particular, Zeilinger et al. [90] investigated the effects of atmospheric

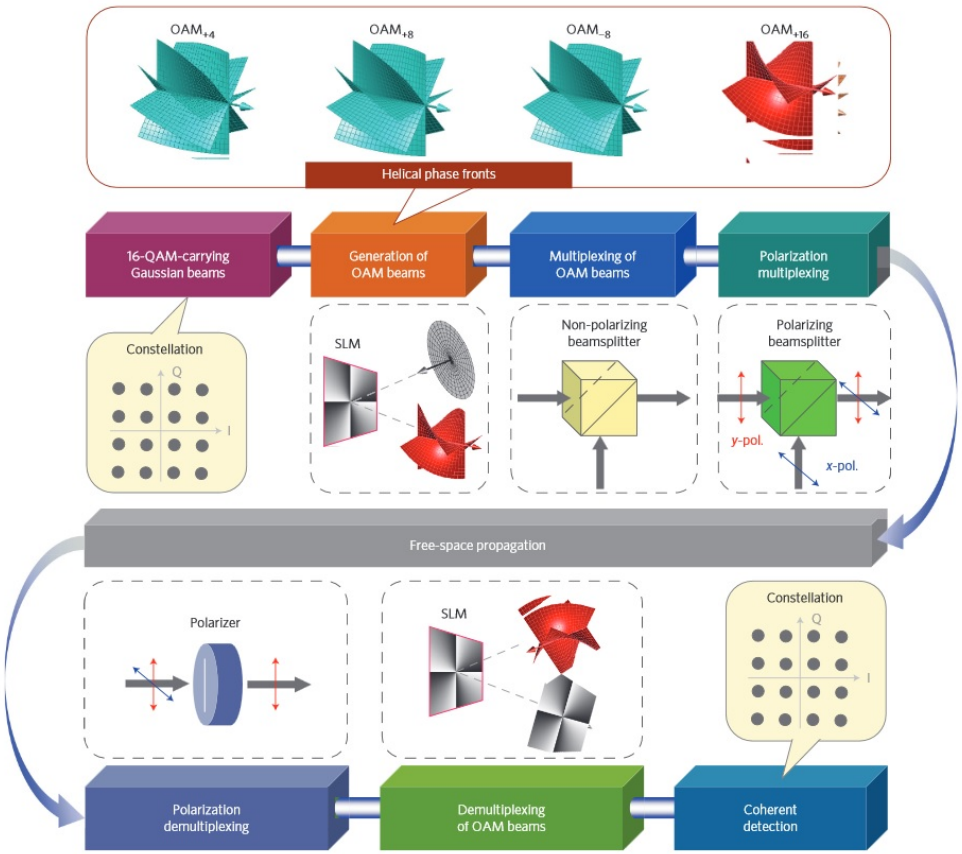

Figure 1.9: Block diagram of the optical OAM-based multiplexing experiment performed by Wang et al. Source: [9].

turbulence on OAM modes propagation. They tested an optical communication link, over a distance of about 100m, in a real urban environment between the roofs of two palaces in Vienna. On the other hand, Bozinovic and Yue [91, 92, 93] tested OAM modes multiplexing after propagation on optical fibers.

1.8.2 Experimental solutions for the RF domain

The use of OAM to implement channel multiplexing has been considered and tested also for the radio domain. The first communication experiment was conducted at the frequency of 2.4GHz, into the Venetian lagoon, by Tamburini et al [94]. OAM waves were used to implement a double channel half duplex link, using the $\ell = 0$ and $\ell = 1$ modes together. The radio link was established over a distance of about 440m. The two electromagnetic modes were transmitted, from the same point, by a standard Yagi antenna and by a modified off axis parabolic reflector (Fig. 1.5), respec-

tively. On the other hand, the reception was realized exploiting wave interferences. In particular, the EM field was sampled by two Yagi antennas spaced of about 40cm. The experiment scheme is shown in Fig. 1.10 where the two Rx Yagi are represented as dipoles. To better understand the reception mechanism, the behavior of the two OAM modes must be considered separately. The two receiving antennas, placed perpendicularly to the incoming field, are aligned to probe

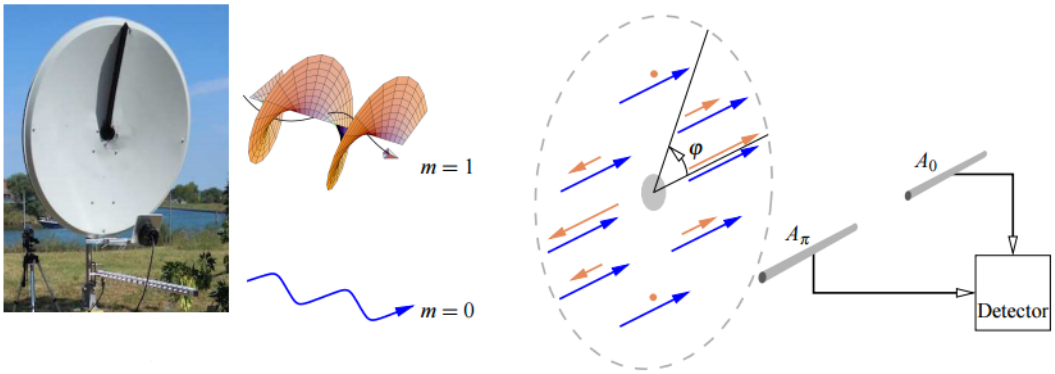

Figure 1.10: Schematics of the radio OAM-based multiplexing experiment performed in the Venetian lagoon. Source: [95].

symmetrically the doughnut $\ell = 1$ mode, along a diameter, (Fig. 1.10). In such a way, considering its field distribution (Fig. 1.1), the two antennas collect two signals with the same intensity but out of phase of π. On the contrary, due to the symmetrical distribution of the $\ell = 0$ field, the two antennas collect, in this latter case, identical signals. Therefore, the antennas outputs were summed to reconstruct the signal associated to the $\ell = 0$ mode and subtracted to reconstruct the signal associated to the $\ell = 1$ one [94].

After this first experiment, other communication tests have been performed both in long and short ranges. For example: in [96] a microwave communication link based on generation and detection of OAM waves by means of fork hologram is studied. In [8], the same test is conducted in the millimeter wave range using spiral phase masks, while in [97] using circular arrays and intensity controlled masks. Iin [98] an OAM based multiplexing is implement in the THz frequency range while in [99] it is implemented by means of metasurfaces. Looking at these experiments, it has been defined also the concept of link budget for OAM links [100].

1.8.3 Limitations of OAM applications to the RF domain

The application of OAM waves to frequency reuse and channel multiplexing started a strong debate [101, 102, 103, 12, 104]. Several objections have been posed to the real efficiency of OAM based systems and on the equivalence between MIMO based and OAM based multiplexing

techniques.

The first criticism concerns the maximum length that can be reached with such systems [101]. In particular: OAM modes are characterized by a doughnut intensity distribution with a central notch that, due to diffraction, becomes more and more large with field propagation. For this reason, to catch the entire field distribution and exploit OAM modes orthogonality after long distances, for example in the far field domain, a huge antenna must be used (Fig. 1.11).

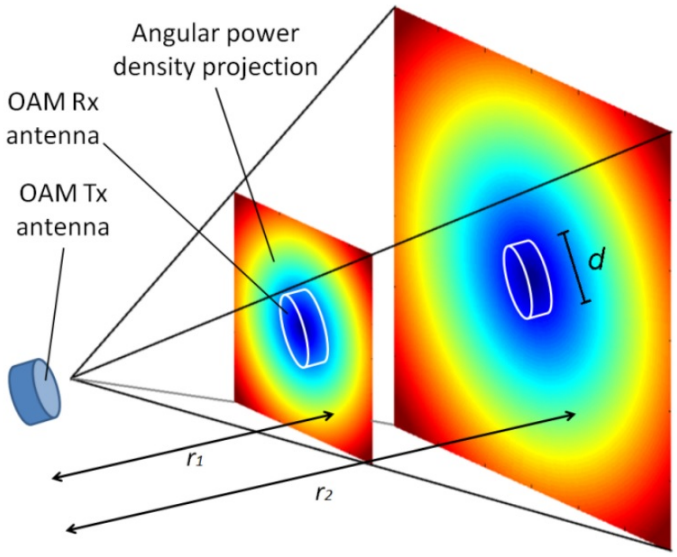

Figure 1.11: Reception of an OAM mode at different distances with a receiving antenna with the same size of the transmitting one. Source: [101].

The second criticism asserts that MIMO systems and OAM ones are equivalent. This fact has been derived, with a theoretical analysis performed by Edfors et al. [12], on circular single ring arrays. The authors analyzed, through linear algebra, the radiation modes of these structures when driven by a MIMO system [105] or by an OAM one and found that the MIMO radiation modes and the relative channels gains are equivalent to the OAM ones. This lead also to an other observation. From MIMO theory it is known that a multi-antenna radio link, without reflections contributions, can implement MIMO multiplexing only if its length is lower than the Fraunhofer one [12]. In other words, when a communication link is longer than its far field distance, only a single radiation mode ($\ell = 0$) can be exploited to transport information, as shown in Fig. 1.12. For this reason, considering the equivalence between OAM and MIMO solutions for circular arrays, Edfors et al. stated that OAM systems can not be employed for long range distances, (far field ones considering the dimensions of practical antennas). The analysis, howver, has been performed only for circular arrays.

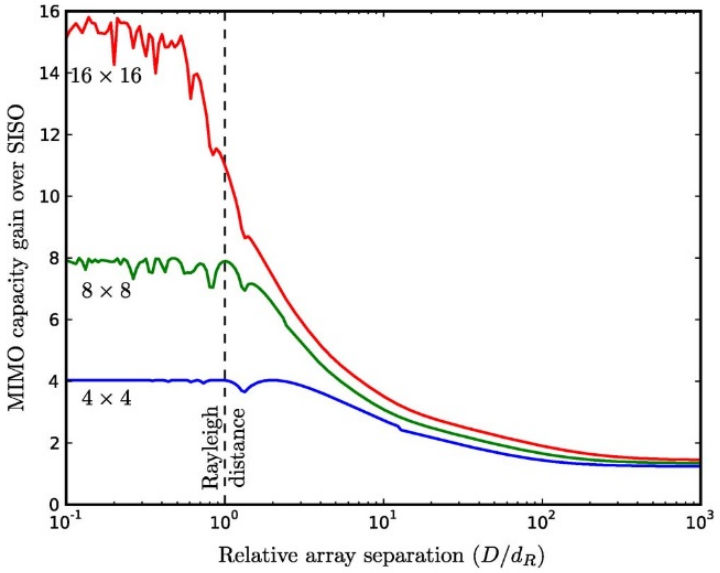

Figure 1.12: Capacity gain of a 4x4, 8x8, and 16x16 MIMO communication system while increasing the distance D between transmitting and receiving antennas. The capacity converges to a SISO system when D is greater than the Fraunhofer distance. Source: [12].

Despite these objections, the debate on this topic is still ongoing since, in the literature, a full and general comparative study on this theme does not yet exist. For this reason, one of the major goal of the thesis is to determine the real performances of long range OAM based communication systems in order to make a fair comparison with today MIMO technology.

1.9 Other applications of OAM waves

OAM waves can be applied not only to telecommunications. They are used also in other fields like: microscopy, astronomy, particle manipulation, electron lithography, etc. For example: OAM beams can enhance the resolution of STED microscopes by overcoming the Rayleigh criterion [106] or by enhancing the image contrast [107]. A similar effect can also be exploited in astronomy where OAM fields improve the resolution capacity of telescopes [108]; they are used, however, also as reference patterns to detect Kerr rotating black holes [109]. OAM fields can be useful also to make particle manipulation: their EM field with circular symmetry and the central null can move and trap nano-particle [110, 111, 112]. In the end, OAM beams can be used also in quantum physics [113, 114, 115] for quantum communications.

Chapter 2

Conformal parabolic antennas

This chapter reports new results on the examination of conformal parabolic antennas which are designed to generate and receive EM waves with integer OAM. The layout and the behavior of such devices, that strongly depend on the particular OAM quantity to be generated or received, are presented and examined by means of simulations and experiments. Conformal antennas are also used to verify, experimentally, the orthogonality between communication channels associated to different OAM modes.

RELATED PAPERS

Mari, E., Spinello, F., Oldoni, M., Ravanelli, R., Romanato, F. & Parisi, G. (2015). *Near-Field Experimental Verification of Separation of OAM Channels*. Antennas and Wireless Propagation Letters, IEEE, 14, 556-558.

2.1 Cassegrain conformal parabolae

Conformal parabolic antennas that are examined in this chapter are based on a Cassegrain structure [67], also known as *prime focus* configuration.

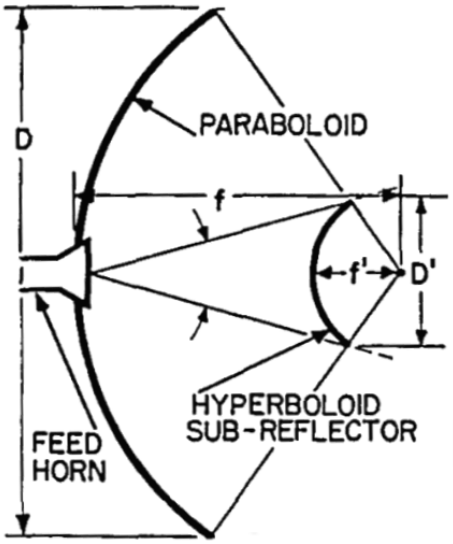

Figure 2.1: Standard prime focus antenna scheme. Source: [116].

A Cassegrain antenna, Fig. 2.1, is normally composed by three elements: a primary reflector (parabolic surface), a secondary reflector (hyperbolic surface) and a feeder. Moreover, the focus of the primary reflector match with the focus of the secondary one to ensure that the antenna radiates a collimated plane wave in far field, (as any parabolic antenna). In fact, in this way, the spherical waves radiated by the feeder, typically a circular or a square waveguide, are reflected by the secondary and by the primary reflector, respectively, and transformed into plane waves focused towards infinity [116]. The surface of a parabolic reflector with focal length equal to F can be described, in a cylindrical reference system (ρ, ϕ, z) with the positive $\hat{z}$ axis as radiation direction, by the equation:

$$z(\rho, \phi) = \frac{\rho^2}{4F} \tag{2.1.1}$$

Conformal parabolic antennas preserve the Cassegrain structure but present a modified primary reflector. Inspired by optical phase masks [52], they are characterized by a twisted primary reflector that is designed to convert the EM field generated by the feeder into a helical wave, with a well defined value of OAM. The surface of the modified parabolic reflector, designed to generate

a vortex beam with order ℓ, can be described by the formula [117]:

$$z(\rho,\phi) = \underbrace{\frac{\ell(\phi-\pi)\lambda}{4\pi}}_{c} + \underbrace{\frac{\pi\rho^2}{4\pi F - \ell(\phi-\pi)\lambda}}_{a\rho^2} \tag{2.1.2}$$

It represents a spiral surface with a special characteristic: the focus F of each radial section is independent on the angular coordinate ϕ. This can be easily proved considering the expression of a generic parabola $z(\rho,\tilde{\phi}) = a\rho^2 + b\rho + c$, whose focus point coordinates are:

$$F_p(\rho,z) = \left(-\frac{b}{2a}, \frac{1-b^2+4ac}{4a}\right) \tag{2.1.3}$$

Substituting the coefficient of Eq. 2.1.2 into Eq. 2.1.3 it results that

$$F_p(\rho,z) = \left(0, \left(1 + 4\frac{\pi}{4\pi F - \ell(\phi-\pi)\lambda}\frac{\ell(\phi-\pi)\lambda}{4\pi}\right)\left(\frac{4\pi F - \ell(\phi-\pi)\lambda}{4\pi}\right)\right) = (0,F) \tag{2.1.4}$$

As can be noticed, for example from Fig. 2.2, the primary reflector is always characterized by a radial step, due to the helix function, whose height depends on the chosen OAM value. In this particular case, (Fig. 2.2), the antenna has been designed to generate a beam with OAM $\ell = 1$. Eq. 2.1.2 is frequency dependent and describes a helical structure associated to a single frequency. For this reason, conformal parabolic antennas are narrow band devices.

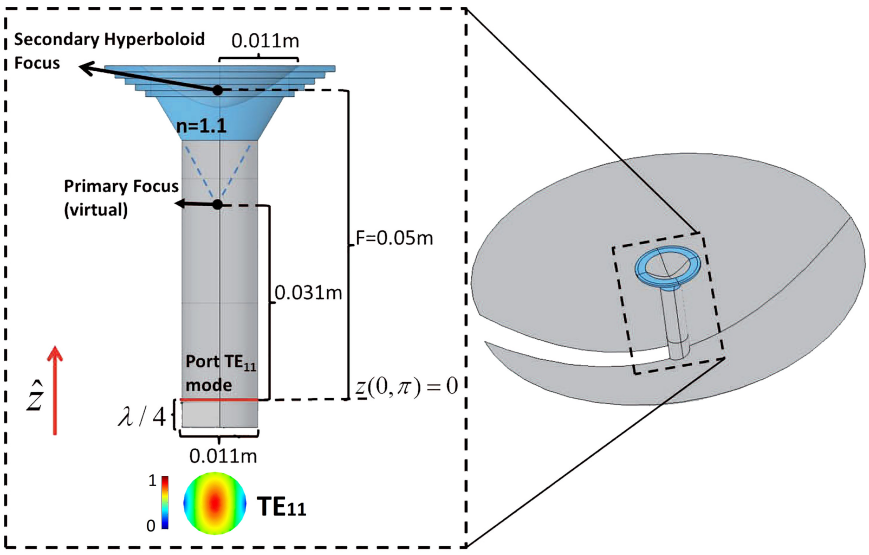

Figure 2.2: A conformal Cassegrain antenna that generates a twisted $\ell = +1$ beam. Inset shows the detail of the feeder and of the secondary reflector which has been used for numerical simulations.

2.2 Conformal parabola behavior

To understand the behavior of conformal antennas it is useful to examine these devices by means of ray optics. When the antenna is used in transmission mode, the rays originated from the feeder are uniformly directed, with the help of the secondary reflector, towards the primary one. Because of the helical profile of the conformal reflector, the path length of each ray is not constant, as can be observed in Fig. 2.3. Each ray emerges from the primary reflector with a different delay, proportional to the length of its path. In this way, the wave radiated by the antenna presents a

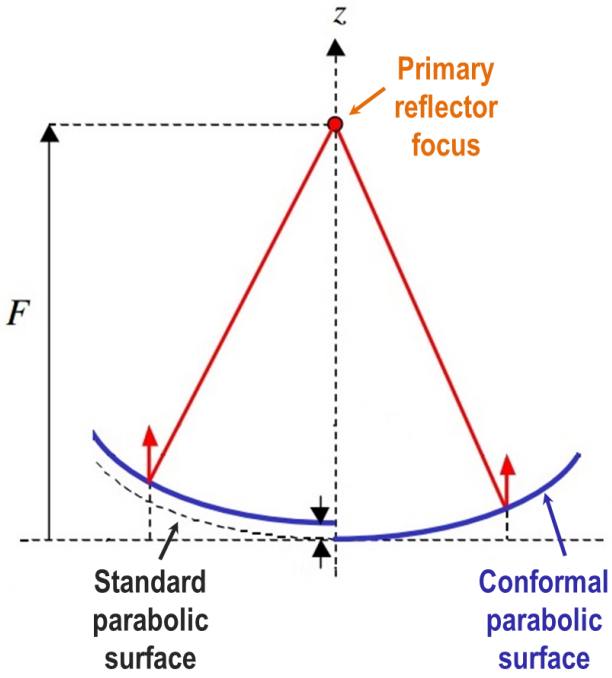

Figure 2.3: A radial section of a prime focus conformal parabolic reflector. Source: [117].

helical phase front, identical to the shape of the reflector, and carries an integer quantity of OAM.

A similar behavior can be found also considering the antenna in reception mode. When an EM field impinge the primary reflector each ray experiments a different reflection delay, depending on its reflection point. For this reason, the rays that sums in the focus point, (where the secondary reflector is located), are characterized by different phase shifts that cause a constructive or a destructive interference.

More in general, from a mathematical point of view, a conformal parabolic reflector can be modeled as an $\exp(\pm i\ell\phi)$ term that multiplies the field distribution transmitted by the feeder or received from free space. The $\pm$ sign depends on the antenna use, transmission or reception

mode, and can be explained thinking at the propagation direction of the EM field. Normally, the OAM values are defined for twisted parabolas used in transmission mode for which the EM field propagates towards the positive z axis. On the contrary, when a twisted antenna is used in reception side it performs as an inverse phase reflector, because of the change of propagation direction. In other words, a transmitting $\ell = +1$ antenna receives like a $\ell = -1$ one [117]. To better understand this fact it can be useful to think at the the movement of the hands of a clock. From a front point of view the hands moves in a clockwise direction (CW), while from a back point of view they moves in the counter-clockwise one (CCW).

2.3 Prototypes design

Within the thesis activities, to practically examine the behavior of such devices, some prototypes of conformal parabolic antennas have been realized by substituting the traditional primary reflector of commercial prime focus antennas (Andrew VHLPX1). In particular, the antennas aperture diameter is equal to 36cm while the focus is located at $z = 5$cm. Both $\ell = +1$ and $\ell = -1$ antennas have been produced to be used at a frequency of 17.2GHz ($\lambda = 1.74$ cm); an example of a $\ell = +1$ one is shown in Fig. 2.4. The custom reflectors were produced by sintering, starting from ceramic

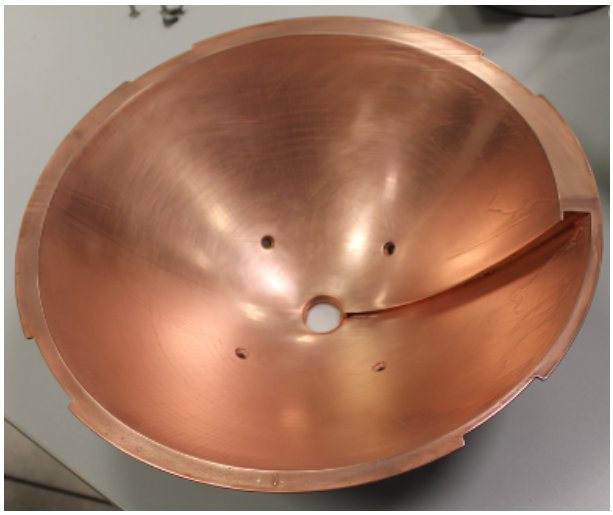

Figure 2.4: Prototype of a conformal parabolic reflector modified for the generation of $\ell = +1$ beams.

powder and the bodies were made of photo-polymeric ceramic material. The surfaces were then covered with copper in an electroplating bath, up to a thickness of about 0.1mm. This treatment was performed only on their internal surface and the final tolerance was better than $\lambda/200$. The feeder, whose structure is shown in Fig. 2.2, is mounted in the same position as for commercial

parabolic antennas ($\ell = 0$). In detail, it is composed by a rectangular waveguide that is then converted in a circular one. For this particular structure, the generated field is always linearly polarized.

2.3.1 Numerical simulations of prototypes behavior

Before producing the prototypes, some MoM (Method of Moments) based numerical simulations of the generated field have been performed. Fig. 2.5 reports an example of simulations results: the far field radiation pattern generated by a $\ell = +1$ parabola. As can be noticed, the field phase presents the typical vortex distribution while the field intensity is characterized by the doughnut shape typical of OAM beams. Moreover, the doughnut intensity is not regular but presents a char-

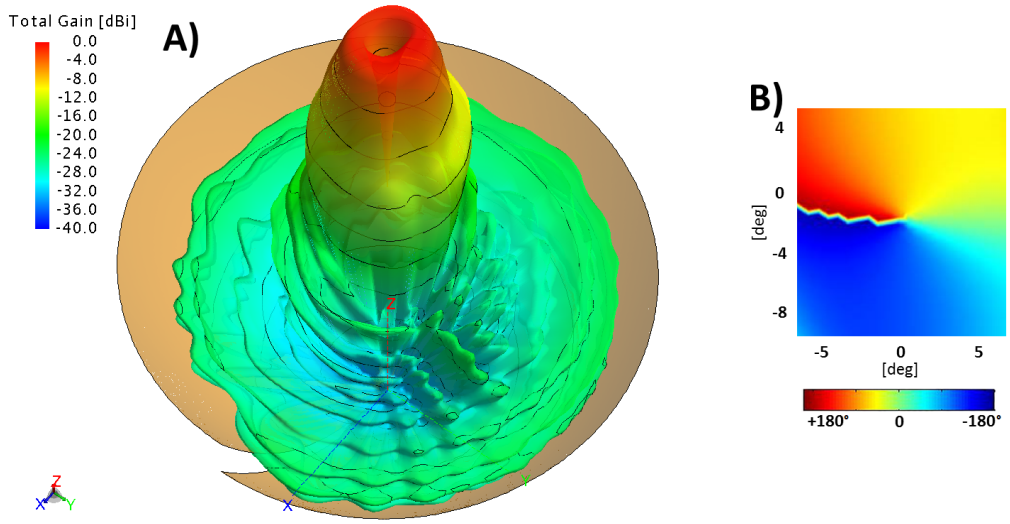

Figure 2.5: Simulation of the far field A) radiation pattern and B) phase of a $\ell = +1$ parabola.

acteristics “fish mouth” shape. To explain this fact it is useful to remember the feeder structure which is composed by a circular waveguide that propagates the field with the TE_{11} mode. Supposing the field vertically polarized, the TE_{11} mode is characterized by a maximum of the field in the guide center and by two minimum at the edges, (Fig. 2.2 inset). For this reason, the radiated far field assume the characteristic “fish mouth” shape.

2.4 Generated fields measurements

The fist experimental test that has been performed is the verification of the correct behavior of all single twisted antenna by measuring intensity and phase of the beam in far-field zone (100m).

The measurements have been performed using the setup sketched in Fig. 2.6. The twisted

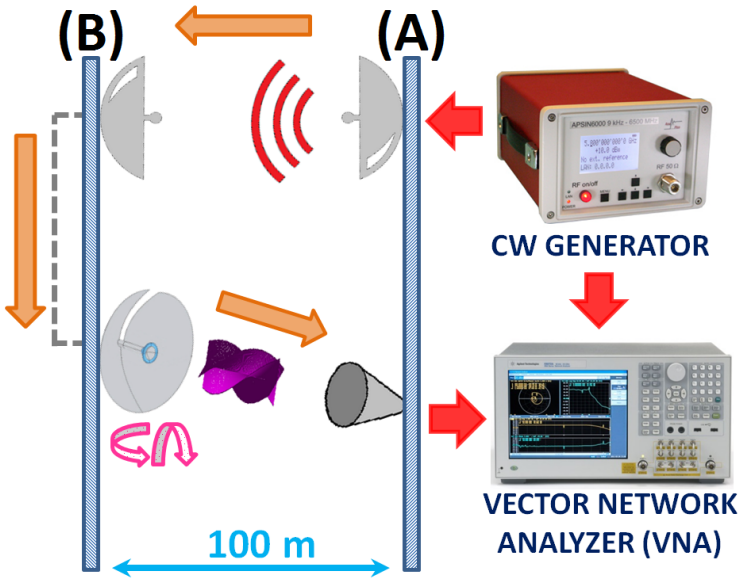

Figure 2.6: Far field measurement setup.

transmitting antenna under test was mounted on a computer-controlled rotator (CCR), moving both in elevation and azimuth with a resolution of $0.2°$. A continuous wave (CW) signal generator, placed on the A side of the test facility, was connected by means of a signal splitter both to a Vector Network Analyzed (VNA) and to a standard parabolic antenna which radiates a 17.2GHz signal towards the B side. Here, the signal was amplified and used to feed the conformal parabolic antenna mounted on the CCR. The generated OAM beam was transmitted towards the A side where it was received by a 7dB gain horn antenna connected to the VNA. Spurious signal interferences were prevented by using microwave circulators after the CW generator and the amplifier. Using this setup, it has been possible to measure not only the generated field intensity but also the phase which always require a proper reference. The choice of mapping the field at a distance of 100m was convenient due to facilities already installed for other experiments.

An example of measured intensity and phase of the beam radiated by the $\ell = +1$ antenna is reported in Fig. 2.7 together with simulations. As can be noticed, the intensity and the phase of the measured field are characterized by the typical distributions of a $\ell = +1$ OAM beam: a doughnut intensity and a vortex phase with an azimuthal span between 0 and 2π. Moreover, using the Spiral Spectrum algorithm [45], it results that the $\ell = +1$ OAM harmonic carries 90% of total field energy. Similar results have been obtained also by the measurements performed on the $\ell = -1$ conformal parabola (Fig. 2.8).

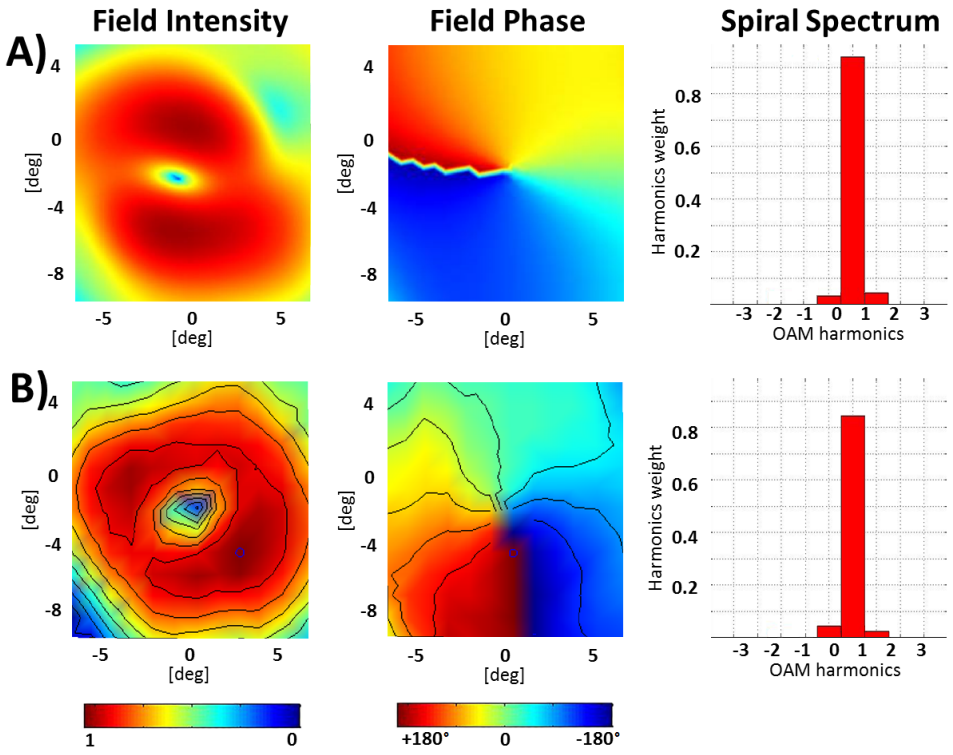

Figure 2.7: Normalized intensity and phase maps, in spherical coordinates, of the $\ell = +1$ radio beam vortex A) simulated and B) measured in free space, at a distance $d = 100$ m from the transmitter. The inner and outer radii of the doughnut, are about 6 and 9 m, respectively.

2.5 Characterization tests

Two different tests have been performed to better characterize the behavior of conformal parabolic antennas. In the first one, it has been measured the Return Loss parameter, in order to determine the radiation capacity of such devices and to make a comparison with standard parabolae. On the other hand, the second test has been performed to verify and evaluate the separation between communication channels associated to different OAM modes. This is a consequence of the orthogonality between OAM states, when the whole beam, in magnitude and phase, is collected. This test was performed at a short distance to ensure that a good fraction of power is received, avoiding the spread of the OAM beam due to propagation. In fact, when using OAM modes, if the distance between transmitting and receiving antennas is too large, the receiving antenna can fall into the center of the doughnut. In this way, it does not collect the entire field, not allowing to exploit the orthogonality property [7, 47].

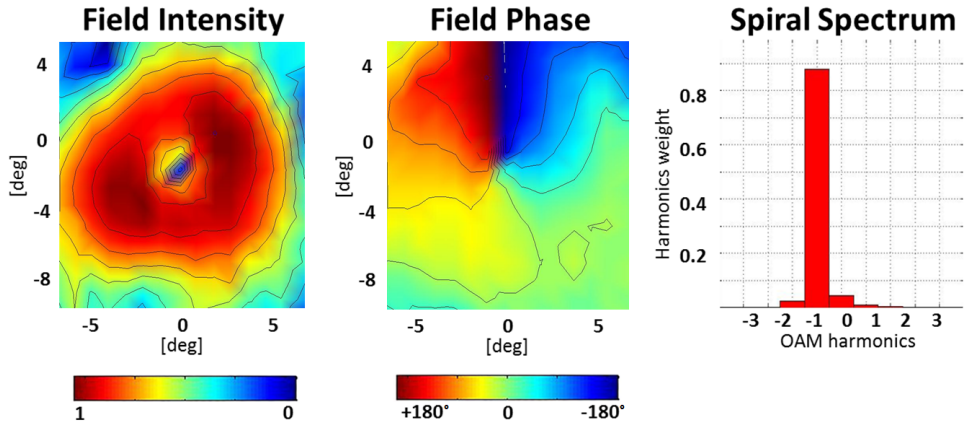

Figure 2.8: Normalized intensity and phase maps, in spherical coordinates, of the $\ell = -1$ radio beam vortex measured in free space, at a distance $d = 100$ m from the transmitter.

2.5.1 Return Loss (RL) tests

As well known, the Return Loss (RL) is defined as the ratio between the incident power (P_i) on the antenna from the feeding line and the reflected one (P_r); namely $RL = 10 \log_{10} P_i/P_r$ [67]. The antennas were placed in open space (OP), freely radiating and the measurements were performed at 17.2GHz, the design frequency of the twisted parabolic antennas (recall that these devices are narrow-band). Each of the built antennas were connected, one at a time, to a port of the VNA and the RL was measured; to perform these measurements the VNA transmitted a constant power of about 20dBm. It has been found that, for both the twisted and the standard antennas, the RL value is approximately equal to 14dB, as expected from the specifications of the standard parabola. After that, the RL measurements were repeated with each parabola in contact with a metal plate (brass) that covers the whole aperture (this is the short-circuit or shielded condition, SH). The obtained results are reported in Table 3.1.

Table 2.1: Return-Loss measurements. Tx(ℓ) denotes the OAM value of the transmitted beam, RL $\equiv$ return loss, OP $\equiv$ open space and SH $\equiv$ shielded condition.

Tx(ℓ)	Experiment	RL [dB]
0	OP	13.7
0	SH	2.3
+1	OP	14.2
+1	SH	16.2

For the standard ($\ell = 0$) antenna, the measured RL value, in SH condition, drops dramatically to 2.3dB. This is a clear indication of an expected and almost complete reflection of the radiated power back into the feeder. In this case, theoretically, RL should be equal to 0. The difference

of this measured RL value and the theoretical one is due to several experimental factors such as power loss (approximatively 1dB/m) of 2m flexible cables and use of waveguide to cable adapters.

On the other hand, the twisted parabola ($\ell = +1$), even if its aperture is shut by the brass plate, still shows a high RL (≈ 16 dB), similar to the one measured in the OP condition. This different behavior with respect to the standard parabola is linked to the OAM geometrical properties. The emitted field's reflection on the brass plate reverses its propagation direction with respect to the fixed z-axis. As a consequence, the OAM topological charge changes sign. So, what comes back from the plate and impinges on the reflector (designed to emits an $\ell = +1$ beam) is an $\ell = -1$ beam. Recalling that the same antenna in reception mode acts like a $\ell = -1$ antenna, a

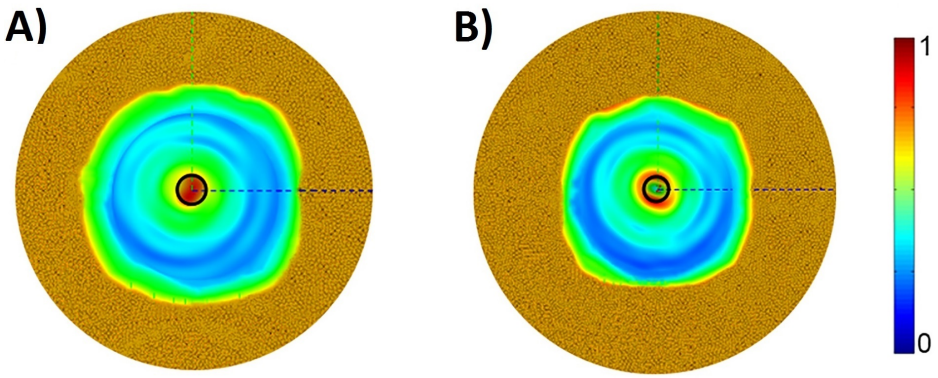

Figure 2.9: Intensity of the electric field (normalized to 1) produced by a $\ell = +1$ wave received by A) an $\ell = -1$ antenna and B) a $\ell = +1$ antenna, in reception mode. External circles represent a top view of the antennas, solid black circles represent the dimension of the feeder. A) an untwisted beam ($\ell = 1 - 1 = 0$) is produced and it is focused into the feeder. B) a $\ell = 1 + 1 = +2$ beam is produced showing that the feeder receives only a small fraction of the beam because of the characteristic central dark zone of the OAM beam.

doughnut field profile, corresponding to $\ell = -2$, is formed on the secondary reflector and a very small fraction of the power reaches the detector. In fact, the beam focused towards the feeder of the receiving antenna acquires the topological charge of the impinging beam plus the topological charge of the antenna in reception mode. For example, when a transmitting $\ell = +1$ antenna operates in pair with an opposite one (i.e. an antenna built as $\ell = -1$ that acts in reception mode as a $\ell = +1$, according to the change of propagation direction), the received twisted beam is transformed into an $\ell = +2$ wave, which can not be collected by the feeder, because the dark region inside the ring is mostly overlapping the feeder aperture. On the other hand, a transmitting $\ell = +1$ antenna in communication with an identical receiving antenna (so $\ell = -1$ in reception mode, as stated above), produces an untwisted beam ($\ell = 0$) that is focused into the feeder. As proof-of-concept, Fig. 2.9 reports MoM-based numerical simulations of the normalized intensity of the electric field focused towards the feeder of twisted $\ell = +1$ and $\ell = -1$ antennas, when

illuminated by a $\ell = +1$ beam. In the first case, an untwisted beam ($\ell = 1 - 1 = 0$) is focused into the feeder. On the contrary, with the twisted $\ell = -1$ receiving antenna, a $\ell = 1 + 1 = +2$ beam is produced. In this latter case, since OAM beams are characterized by a doughnut-shaped intensity distribution, the central dark zone hits on the feeder and only a small portion of signal is received.

2.5.2 Orthogonality tests

The particular behavior just explained is useful to understand also the results of the orthogonality tests for combinations of aligned transmitting (Tx) and receiving (Rx) antennas of different type. The antennas faced each other at a short distance (less than 1 cm from their outer border), keeping the (vertical) polarization concordant. The alignment of the antennas ensures the collection of the whole OAM beam. The orthogonality evaluation has been performed by measuring the Insertion Loss (IL) parameter which is defined as the ratio between the Tx and the Rx powers measured at two different sides of a radio link. The IL is calculated as: $IL = 10 \log_{10} P_{TX}/P_{RX}$ [67] and quantifies the signal power lost between the transmission and the reception point. The lower its value, the better the signal transmission. The Tx antenna was connected to the first port of the VNA while the Rx one to the second port; then the instrument was configured to measure the IL. Frequency and power parameters are identical to those used for the measurements of RL. Table 2.2 shows the experimentally-obtained results. As expected, pairs of identical antennas,

Table 2.2: Insertion Loss (IL) measurements. Tx and Rx columns identify the transmitting and receiving antennas.

Tx(ℓ)	Rx(ℓ)	IL [dB]
0	0	3.3
+1	+1	3.2
+1	0	18.6
+1	-1	26.2

facing each other, show a good throughput ($IL_{\ell=0} = 3.3$ and $IL_{\ell=1} = 3.2$). On the other hand, pairs of twisted antennas of different type exhibit an excellent modal isolation: an insertion loss of 18.6dB was measured when a standard antenna receives a twisted beam, and an even better isolation of 26.2dB when Tx and Rx antennas have opposite OAM values. This is compatible with the expected behavior of OAM beams impinging on antennas with opposite topological charge.

2.6 Conclusions

In this chapter, the structure and the behavior of conformal parabolic antennas that generate and receive OAM beams have been examined. In particular, from all the presented experimental results, it is clear that is possible to separate OAM channels when the whole beam is correctly collected; a condition that can be easily satisfied at short distances. A possible application of this property, in telecommunication, could be in short-range high data-rate links [8] in indoor environments. By taking advantage of separation between OAM channels that is a physical consequence of the orthogonality of OAM states, it is possible to implement a multi-channel system with a very simple post processing.

Up to now, the study have been limited to near-field conditions, strengthening the idea of exploiting OAM in short distance communication[12], when both the transmitting and receiving antennas are facing each other. A possible application of such devices over long distances will be examined in next chapter.

Chapter 3

A long range OAM-based link

This chapter presents an outdoor experiment in which a long-range OAM-based multiplexing system is implemented. The communication link, composed by three channels on the same frequency and polarization state, is based on OAM modes $\ell = -1, 0, +1$, generated and received by means of conformal antennas. The experiment aims to study how OAM modes can be used to communicate over long distances, when the exploitation of orthogonality becomes difficult because of the huge size of received fields.

RELATED PAPERS

Tamburini, F., Mari, E., Parisi, G., Spinello, F., Oldoni, M., Ravanelli, R. A., Coassini, P., Someda, C. G., Thidé, B. & Romanato, F. (2015). *Tripling the capacity of a point-to-point radio link by using electromagnetic vortices*. Radio Science, AGU, 50(6), 501-208.

3.1 Introduction

Orbital Angular Momentum waves form a complete orthogonal set [6] and can be employed to implement new multiplexing systems that better exploit the electromagnetic spectrum. However, to take advantage of OAM fields orthogonality, it is mandatory to receive their whole distribution [7]. While this request can be easily complied at short distances, it is more complicated to satisfy at long ones. In fact, due to diffraction, electromagnetic fields enlarge during propagation and it is difficult to receive their whole phase front with small antennas. For this reason, the implementation of long range OAM-based multiplexing systems requires several attentions.

Within this particular framework and keeping in mind the theoretical studies on OAM based systems [101, 102, 103, 12], it will now be presented a communication experiment performed in a real urban environment. The experiment is intended to test a half duplex radio link, composed by three channels at the same frequency and polarization state, each one associated to a different OAM mode. Conformal parabolic antennas, presented in the previous chapter, are used to transmit and receive the OAM fields.

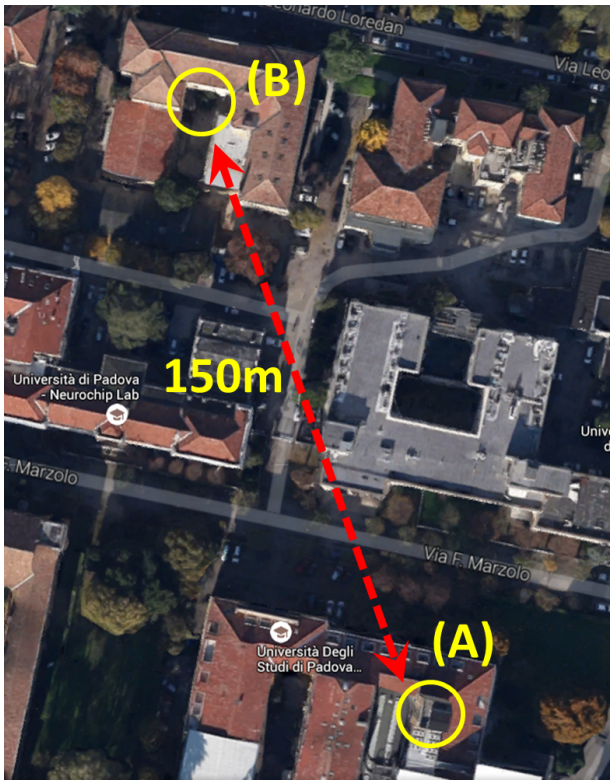

Figure 3.1: Top view of the communication link installed at the Department of Physics and Astronomy at the University of Padova.

The experiment represents a great opportunity to investigate the potentials and the limitations on the use of OAM waves in long range communication systems (far field domain) and to examine two interesting issues. The first one concerns the study of the orthogonality property when the received field can not be completely received. With the experiment, in fact, it is possible to evaluate how a limited orthogonality increases the mutual interference between channels. The second one, on the contrary, concerns how the peculiar field distribution of OAM modes can still be exploited to implement a channel multiplexing not using modes orthogonality.

Looking at the literature, at the best of today knowledge, this is the first OAM-based multiplexing experiment where more than two channels are used without any digital post processing.

3.2 Experimental setup

As briefly mentioned in the previous section, the experiment tested a point-to-point half-duplex radio communication link in free space, using simultaneously three channels associated to different OAM states, $\ell = 0$, $\ell = +1$ and $\ell = -1$, on the same frequency band centered at 17.128GHz, and with the same (vertical) polarization. The transmitting and the receiving side of the link were installed on the rooftops of two buildings (A and B, for transmission and reception, respectively) at the SIAE Microelettronica industrial compound in Cologno Monzese, near Milan, Italy, for the first experimental session, and later on two terraces of the Department of Physics and Astronomy at the University of Padova, Italy, for the second one (in the following, called site CM and PD). The link was tested on two different places to demonstrate the robustness and repeatability of the triple OAM radio links, over different distances. At CM, the distance between the transmitter and the receiver was 100m ($\sim 5900\lambda$ wavelengths at 17.128 GHz), while in PD it was 150m (~ 8800 wavelengths). The two environments (including buildings, trees, path inclination with respect to ground) were significantly different.

In all tests, generation and reception of each OAM beam was made through a pair of identical antennas, placed on the transmitter-receiver line of sight. Each of them was a parabolic "twisted" antenna, identical to the models described in Chap. 2. A typical example of the measured field distribution, both in intensity and phase, of the twisted beam radiated by the $\ell = -1$ antenna, at 100m is presented in Fig. 3.2. Both at receiving and transmitting side, the three antennas (built to generate and receive beams with $\ell = 0, -1, +1$) were vertically stacked, for logistic reasons, with a gap of about 30cm between the edges of their apertures (36cm in diameter). The untwisted ($\ell = 0$) beam was generated and received by a couple of standard parabolic Cassegrain antennas (Andrews VHLPX1). The OAM beam generating antennas had the same diameter and focal ratio as those used for the untwisted beam. The radio equipments used in these experiments were commercially available units, manufactured by SIAE Microelettronica, (ALFOplus [118]). They are completely configurable in all features of interest: transmitted power, modulation scheme,

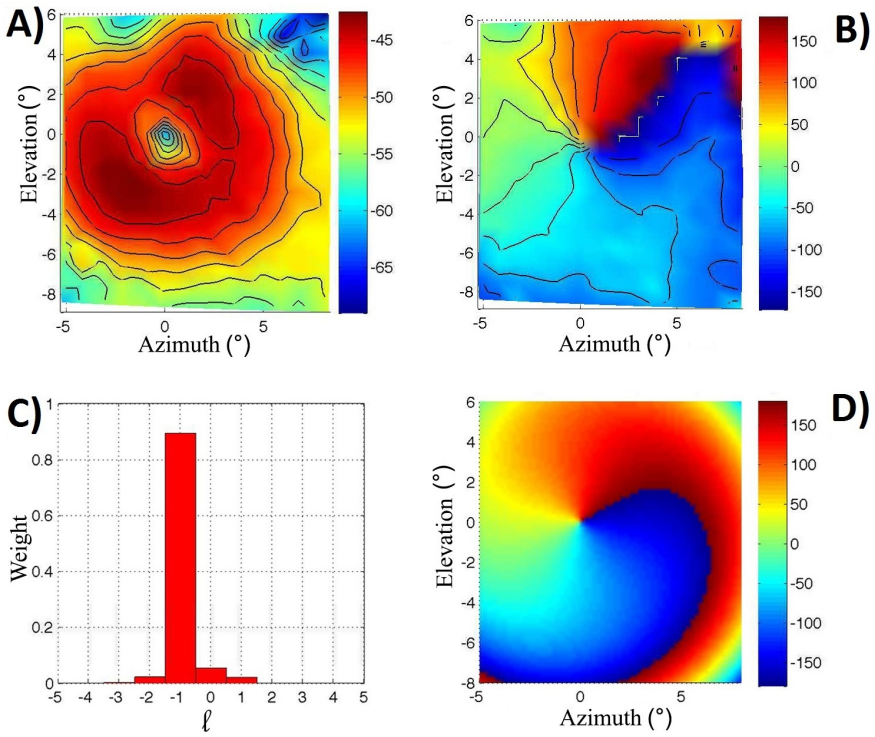

Figure 3.2: A) intensity and B) phase distributions of the $\ell = -1$ radio beam vortex measured in free space, at a distance $d = 100$m from the transmitter. C) spiral spectrum of the measured field. D) numerical simulation of the measured phase distribution.

carrier frequency, modulated bandwidth. The radio units can operate as full duplex transceivers, and implement standard forward error correction based on the low-density parity-check codes (LDPC) algorithm [119]. Passive and active components were connected via flexible elliptical single-mode waveguides. Each twisted antenna was mounted on a computer-controlled rotator, moving both in elevation and azimuth with a resolution of $0.2°$. Using the computer-controlled rotator, each twisted transmitting and receiving antenna was properly aligned in order to minimize the interference between channels at the receiving side, as explained in more details in the next sections.

To optimize the OAM modal isolation in the triple link, the received powers in the three channels were equalized. This operation must take into account the actual geometrical shape of LG beams. In fact, for a fixed antenna aperture, the peak intensity of an OAM beam is a function of its topological charge, and decreases as the OAM value increases [6]. In our case, the peak difference between an $\ell = \pm 1$ and an untwisted beam is 6dB. Because of this, in order to equalize the three signals at the receiving point, the $\ell = 0$ antennas were equipped with an additional 10dB

fixed attenuator. Thus, the power levels at the 3 receivers were comparable. To better fine-tune this equalization of channel powers, also the transmitters could be set at different output power levels.

Figure 3.3: Example of transmission side of the link with three parabolic antennas installed on a pole. $\ell = \pm 1$ antennas are on the top and on the bottom, respectively. Inset: picture of a twisted $\ell = +1$ antenna without radome.

3.3 Ideal experimental conditions

The natural orthogonality between different OAM beams can be totally exploited, in order to separate different OAM channels, if all the phase information of the transmitted beam is collected by the receiver, i.e. if the detector size can be comparable to the received beam size. In this condition, in fact, conformal antennas act as inverse phase reflectors, as proved in Chap. 2. An EM vortex, characterized e.g. by a phase rotation in the CCW direction is seen by the receiving antenna as a vortex rotating in the CW direction because of the local inversion of the z axis. When a receiving antenna operates in pair with an identical transmitting one, it transforms the received twisted beam into an untwisted ($\ell = 0$) wave, which is focused into the feeder/coupler. From there it propagates to the receiver via the fundamental (TE11) mode of an elliptical single-mode waveg-

uide. The real configuration, unfortunately, is quite far from being ideal due to the spread of the propagating OAM beams [120]. In fact, the inner and outer radii at 3dB of the doughnut, for the $|\ell| = 1$ beams, at a distance of 100m, are about 6 and 9 m, respectively. If the receiving antennas are obliged to be comparable in size to commercial ($\ell = 0$) ones, this entails a significant decrease in the fraction of the beam power collected at the receiver, and, even worse, the reception of a very small area of the phase front. This leads to significant difficulties to recognize the phase footprint of the received beam, which clearly impacts on orthogonality. For these reasons, it is necessary to adopt a more elaborate strategy in order to discriminate the three received signals.

3.4 Antennas alignment

Antennas alignment is a fundamental step for the right configuration of the link and it was studied to minimize channel interferences. For this reason, the best configuration that can be adopted with respect to the link infrastructure is presented. In practice, as shown in Fig. 3.4, each twisted transmitting antenna is aimed to the center of the opposite one on the other side and the standard antennas are faced each other. In such a way, on the receiver side (the most demanding part of

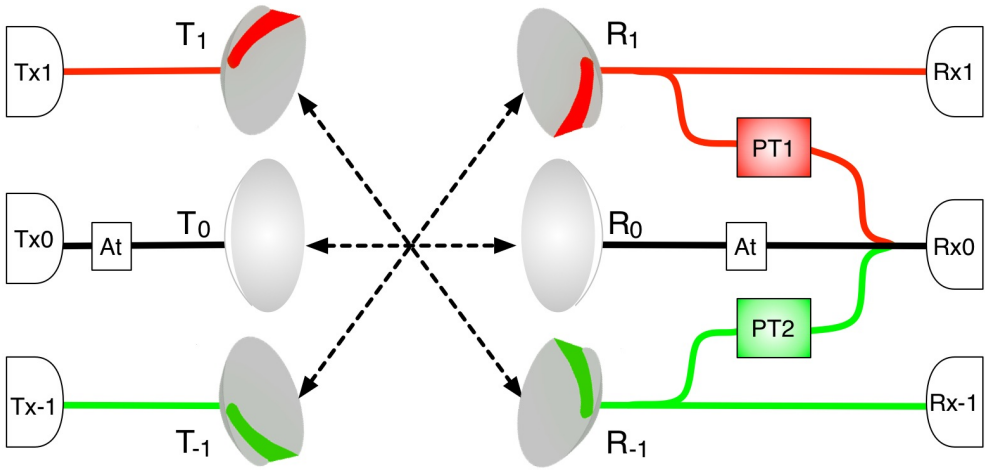

Figure 3.4: Schematics of the triple radio links. Each twisted transmitting antenna aims towards the receiving antenna of opposite OAM sign $\ell = \pm 1$. The label `At` refers to a 10 dB static attenuator. `PT` is a block consisting of a phase shifter and a variable attenuator. Dashed lines represent the aiming directions of the antennas (angles and distances are not to scale). Solid lines represent waveguides. Each bifurcation of a solid line represents a -3dB three-way directional coupler.

the experiment), separation of the three channels is obtained not only with orthogonality between different OAM states but also exploiting the central power null typical of the doughnut field distribution of OAM modes. The alignment with an OAM beam turned out to be quite simple, because

the reference point is the minimum of intensity in the center of the beam, due to the characteristic phase singularity.

During the alignment procedure, the radio units were configured to transmit, on a 4-QAM constellation, a dummy data signal, with a bandwidth of 7MHz. The transmitted powers, for each channel, were calibrated as to equalize the received ones, as shown by the main diagonal of Table 3.1. In particular, the output powers from the $\ell = 1$ and the $\ell = -1$ transmitters were 22dBm while that from the $\ell = 0$ was 8dBm. The received powers were measured turning on each transmitting radio, one at a time. On the other hand, the SNR values were measured during the full operation of the triple link, i.e., all the Tx radios were turned on, and each of them was transmitting an independent dummy data stream. Both the power levels and the SNR values were directly measured and evaluated by the radio controllers.

The antennas alignment is analyzed in details in the following sub-sections. Let T_i (R_i) to indicate the transmitting (receiving) antenna designed for the $\ell = i$ ($i = -1, 0, 1$) beam, and an arrow ($\rightarrow$) stands as a symbol for the connection (both wanted and unwanted, i.e., generating a desired or a spurious signal) between two of them. Obviously, the goal is to maximize modal isolation between channels having different OAMs, between transmission (A) and reception (B) sides.

3.4.1 Isolation and interference between antennas with different OAM.

$\mathbf{T_1 \rightarrow R_{-1}}$ and $\mathbf{T_{-1} \rightarrow R_1}$

In the experimental setup these antennas are aimed to each other, so, the whole phase information is collected. As a consequence, a good modal isolation is achieved because of the difference in spatial phase distribution between OAM states of opposite sign. In addition, the receiving antennas are located within the null of the transmitted field at the doughnut center. The total modal isolation is about 26dB.

$\mathbf{T_0 \rightarrow R_{-1}}$ and $\mathbf{R_1}$

When the three beams are all active, the twisted receiving antennas (R_1, R_{-1}) are exposed to a portion of the $\ell = 0$ beam (T_0), i.e. to an interfering plane wave. The twisted antennas exhibit a natural modal isolation of about 10-12 dB, experimentally tested in the far field.

$\mathbf{T_1}$ and $\mathbf{T_{-1} \rightarrow R_0}$

The standard receiving antenna (R_0) does not fully benefit from the modal isolation, because of the limited phase footprint of the impinging OAM beams. In fact, the partial phase footprint of the vortex that reaches R_0 provides a small, albeit limited, modal isolation. However, given

the antenna alignment strategy adopted in our setup, R_0 intercepts a very small power fraction of each twisted channel, because it falls within the dark center of the doughnut. As an overall result, the untwisted mode suffers the largest interference exposure. To improve its immunity to interference, we inserted, in the waveguide connections between R_0 and its receiver (elliptic flexible waveguides), a couple of static mode cancelers, namely, two blocks, each comprising an attenuator plus a phase shifter. The purpose of these two devices is to minimize the levels of the T_1 and T_{-1} interfering signals at the input of the Rx_0 receiver. The overall connection scheme is shown in Fig. 3.4, where the mode canceler PT1 is shown. A portion of the T_1 signal, received by R_1, is split, sent to PT1, and then exploited to generate a destructive interference. This requires suitable attenuation and phase shifting with respect to the signal received directly from R_0, whence the two blocks. Splitting and recombination are made with standard 3-way splitter/combiners. Quite similarly, PT2 minimizes the interference signal due to T_{-1}. The two mode cancelers needs to be calibrated one at a time. With the mode cancelers, it has been possible to minimize the level of spurious $\ell = \pm 1$ signals overlapping the $\ell = 0$ one, achieving a reduction of the resulting interfering signals of one order of magnitude with respect to the signal that R_0 receives from T_0. The modal isolation, in this case, is equal to 18dB.

3.4.2 Transmission and reception between identical antennas

$\mathbf{T_1 \rightarrow R_1}$ and $\mathbf{T_{-1} \rightarrow R_{-1}}$

Finally, the $\ell = \pm 1$ signals transmitted from site A (T_1, T_{-1}) are collected by the identical twisted parabolic antennas at the receiving site B (R_1, R_{-1}). The ideal condition (i.e., the collection of the whole phase footprint by the receiving antenna), is not fulfilled, as the antennas are not aligned. When the SNR is good enough to operate a digital link (SNR> 10 dB), the main remaining drawback is that R_1 and R_{-1} catch only a part of the phase footprint of the wanted OAM beam. Nonetheless, since both R_1 and R_{-1} fall within the 3dB region of the corresponding transmitted vortex, the received signal is strong enough to be partially collected. Note that it would be impossible to reach the same signal level, because of the central null, if the two antennas were aimed straight at each other.

3.5 Communication results

Adopting the strategy of exploiting both the natural isolation between OAM states and the characteristic OAM radiation pattern, a total isolation better than 10dB between all 3 channels has been obtained. The detailed received powers for the PD 150m long triple link are reported in Table 3.1, associated with the SNR of each receiving channel. In both CM and PD experiments, an error-free throughput of 3×11 Mbit/s with 4-Quadrature Amplitude Modulation (QAM) [121] over

a 7MHz bandwidth was achieved. The radio bandwidth was set to 7MHz because of narrow-band phase shifters. This is sufficient to send a DVD quality video signal on each channel. A typical screenshot of the received constellations is shown in Fig. 3.5.

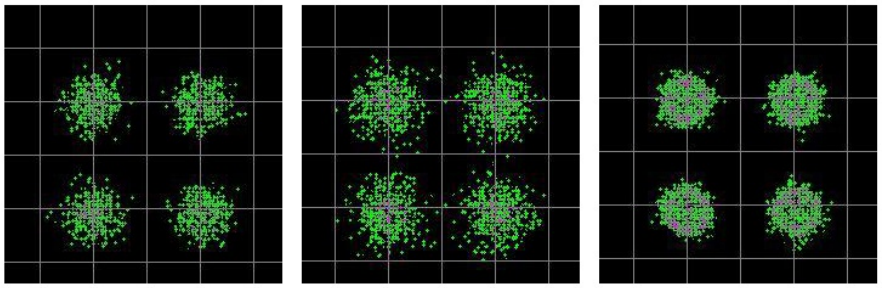

Figure 3.5: Received 4-QAM constellations of 3 independent digital channels in the PD experiment. From left to right: channels R_{-1}, R_0 and R_{+1}.

Table 3.1: Measurement for PD experiment (150m length). The output power from $\ell = 1$ and $\ell = -1$ radio transmitter is 22dBm, from $\ell = 0$ is 8dBm.

		Tx			
		$\ell = +1$	$\ell = 0$	$\ell = -1$	SNR(dB)
Rx	$\ell = +1$	-56	-65	-80	10
	$\ell = 0$	-74	-55	-71	9.1
	$\ell = -1$	-85	-63	-53	12.2

3.6 OAM radio channels and digital modulations

To better study the OAM-based communication process, the robustness of a channel associated to an OAM radio beam has been tested.

3.6.1 Single channel full-duplex communication link

Initially, both in CM and PD sites, a single-channel bidirectional data exchange using one OAM beam has been implemented, obtaining a stable full-duplex link that provided a very high data rate without any digital post-processing. The full-duplex single link proved that the beam generated (and received) by a twisted $\ell = +1$ antenna can support a complex modulation scheme (1024-QAM) over a quite wide bandwidth (56MHz), resulting in an error-free throughput of 436Mbit/s

per direction. The frequency for the A $\rightarrow$ B link was 17.128GHz, whereas for B $\rightarrow$ A it was 17.272GHz. More in detail, propagation axis of the transmitting $\ell = +1$ antenna at site A (B) was initially aimed towards its counterpart at site B (A), which caused the receiving antenna to be in a minimum, due to the doughnut-shaped radiation pattern. To overcomes the inconvenience of minimum received signal for direct aiming, the antennas were tilted slightly upward (< 1 degree). After tilting, the constellation levels reach up to a 1024-QAM (10 bits per symbol). The data rate behavior was consistent with the measured radiation pattern of the twisted parabolas, whose doughnut intensity, at the selected distance, peaks at an angle between 2 and 3 degrees from axis, according to numerical simulations. The error rates at both sides remained zero for the whole duration of the experiment (one day), while the signal-to-noise ratios were equal to $\approx$40dB, well above the equipment error-free thresholds. The total throughput for the single duplex link was about 2×436 Mbit/s.

3.6.2 Double channel half-duplex communication link

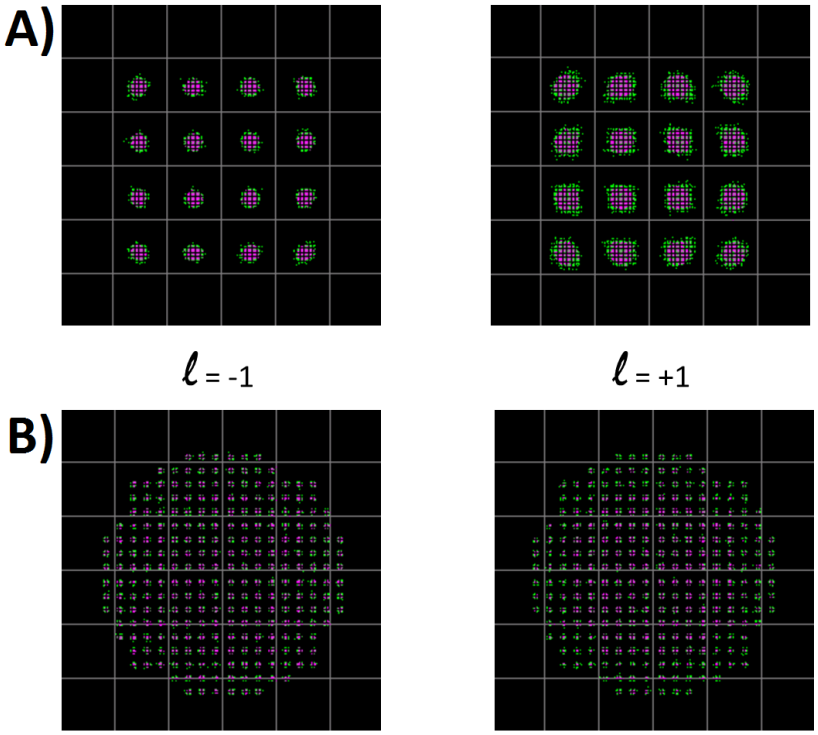

Figure 3.6: Received digital A) 16-QAM and B) 256-QAM constellations of 2 independent digital channels. From left to right: channels R_{-1} and R_{+1}.

A double half-duplex OAM link was then implemented, to test unidirectional data transfer

via two OAM beams generated by the twisted parabolas $\ell \pm 1$, at the same carrier frequency (17.128GHz), with vertical polarization. The gaps between the antenna apertures on the mast were about 1m wide. Each of the transmitting antennas (at site A) was aimed towards its opposite-sign counterpart, in the same way as the triple link. For both the signals a SNR between 22 and 25dB was achieved, leading to an error-free throughput of 2×171 Mbit/s, with 16-QAM modulation over a 56MHz bandwidth (Fig. 3.6A). Further improvements of the isolation between channels have been obtained by introducing a pair of attenuator-phase shifter blocks, thus implementing a basic static canceling scheme (see the previous Section). They were connected to the receiver front end via 3 additional directional couplers, so that the residual $\ell \pm 1$ spurious signal could be suppressed. Manually adjusting the attenuation levels and the phase delays to minimize interference, it was achieved an SNR equal to ≈ 30dB with an error-free 256-QAM modulation (8 bits/symbol) per channel. This required again a reduction of the bandwidth to 7MHz, because of the narrow-band phase shifters. Still, due to the modulation increase to 256-QAM (Fig. 3.6B), an error-less throughput of 2×42 Mbit/s was obtained.

3.7 Conclusions

In this experiment, the basic properties of OAM radio beams have been exploited to realize a long range (far-field) triple link, using a single carrier frequency and a single polarization state. This is the first example of free-space OAM-based radio multiplexing with more than two channels and without any digital post-processing. Moreover, performing additional ad-hoc tests on site, it results that it is not possible to reproduce the link behavior by exploiting only the linear momentum properties of EM waves, even when it is combined with beam shaping techniques. In fact, additional tests showed that by replacing the two receiving twisted antennas with two standard ones, while keeping the same $\ell = 0$, $\ell = +1$ and $\ell = -1$ transmitting antennas, with equal condition (post processing, distance between antennas), it was not possible to discriminate between the three channels because of their high mutual interference. So, the intrinsic isolation provided by the twisted receiving antennas appears to play a crucial role.

Within this study, also the major difficulties of employing OAM modes for long range communications have been presented. In particular, the fact that it is not possible to fully exploit orthogonality without antennas of suitable size. This is the main reason for which the experiment was characterized by the peculiar antennas alignment previously described. However, it is also clear from these tests that some properties of OAM modes, like the particular intensity distributions, can be useful also in non ideal situations to improve communication performances.

In conclusion, the experiment has been a practical demonstration both of potential and mostly of limits of using OAM beams for radio multiplexing. It represents a first step along a new way, which investigate how this quantity can be useful for telecommunications. To continue this study,

next chapters will examine some interesting proposals that may reduce the size of received fields and allow a fully exploitation of modes orthogonality.

Chapter 4

OAM fields concentration

This chapter presents a method, based on proper superpositions of integer and consecutive OAM modes, that allows to concentrate the intensity distribution of an OAM field. Moreover, by acting on the superimposed beams parameters, the method allows to control also the phase gradient within the field. This technique may be used to reduce the size of OAM fields and to better exploit modes orthogonality in long range communication systems. Otherwise, it can be used to generate EM waves with a custom field distribution.

RELATED PAPERS

Parisi, G., Mari, E., Spinello, F., Romanato, F., & Tamburini, F. (2014). *Manipulating intensity and phase distribution of composite Laguerre-Gaussian beams*. Optics express, OSA, 22(14), 17135-17146.

4.1 Introduction

Chapter 3 presented a far field communication experiment and studied potentials and limitations of using OAM modes in long range multiplexing systems. In particular, it has been observed that the major criticism concerns the exploitation of OAM modes orthogonality when small antennas are used. In fact, the OAM orthogonality property, that is fundamental to reach a low interference between different channels, can be exploited only when the whole EM fields are received.

To overcome this limitation, one can increase the size of receiving antennas. Unfortunately, while this solution allows to receive the whole field distributions, it is not practicable because of the complexity and of the cost when dealing with huge structures. On the other hand, one can try to reduce the size of received EM fields keeping their OAM values different from zero.

Considering this latter idea, it will be presented, in the follow, a new method to manipulate both intensity and phase distributions of a beam with non-zero orbital angular momentum. More in details, by using a smart combination of OAM modes, the technique allows to concentrate the field intensity in a restricted angular domain and to embed a certain phase variation within the concentrated beam. The method is developed considering the scalar field of LG beams because of its simple mathematical expression. It consists in superimposing a given number N of coherent OAM modes, with a proper amplitude term, characterized by integer, concordant and consecutive value of OAM. As will be presented in the following, acting on these parameters one can fully control the EM field distribution.

4.2 LG beams consecutive superpositions

To study the field concentration effect, it is useful to use LG beams because they are one of the most simple OAM field solution of the paraxial wave equation, as described in Chap. 1. A generic superposition of coherent and coaxial LG modes, each of them with integer and non-zero value of topological charge [5], can be written, in a cylindrical reference system (ρ, ϕ, z), as

$$u_{tot}(\rho, \phi, z) = \sum_{n} u_n(\rho, \phi, z) e^{i\delta_n} \tag{4.2.1}$$

where $u_n(\rho, \phi, z)$ is the expression of the n-th LG beam and δ_n is the relative phase with respect to the first one. For simplicity, but without loss of generality, LG modes are assumed to have the same beam waist w_0 and the same relative phase, for example $\delta_n = 0$. Moreover, they are characterized by a null radial index, $p = 0$, and by topological charges ℓ_n with *concordant and consecutive values*. With all these prescriptions, the coherent superposition of N concordant and consecutive modes in Eq. 4.2.1 can be written as follows:

$$u_{tot}(\rho, \phi, z) = \sum_{n=n_{min}}^{n_{max}} u_n(\rho, \phi, z) = \frac{1}{w(z)} e^{-\frac{\rho^2}{w^2(z)}} e^{-\frac{ik\rho^2}{2R(z)}} \sum_{\ell=\ell_{min}}^{\ell_{max}} A_\ell \alpha^{|\ell|}(z) e^{i(2|\ell|+1)\xi(z)} e^{-i\ell\phi} \tag{4.2.2}$$

where the maximum OAM term in the sum is $\ell_{max} = \ell_{min} + N - 1$, the beam radius $w(z)$ is fixed and equal for all the superposed modes, the parameter $\alpha(z) = \sqrt{2}\rho/w(z)$ is related to the spatial beam distribution and ℓ_{min} gives the minimum OAM value of the set of the superposed OAM modes.

As can be observed in Eq. 4.2.2, each OAM mode is pounded by its amplitude factor A_ℓ. These factors are fundamental to obtain the field concentration effect because they determine the weight of each OAM mode within the superposition. To better clarify this concept, two distinct cases of coherent superposition of OAM modes will be examined, looking at the fields distributions at the beam waist plane ($z = 0$).

In the first one, A_ℓ is a pure constant, equal to one for convenience. As a consequence, it is possible to expand the series in Eq. 4.2.2 into a new formulation with help of [122],

$$u_{tot}(\rho, \phi, 0) = \frac{1}{w_0} e^{-\frac{\rho^2}{w_0^2}} \alpha(0)^{\ell_{min}} e^{-i\ell_{min}\phi} \sqrt{\frac{\alpha(0)^{2N} - 2\alpha(0)^N \cos(N\phi) + 1}{\alpha(0)^2 - 2\alpha(0)\cos(\phi) + 1}} \tag{4.2.3}$$

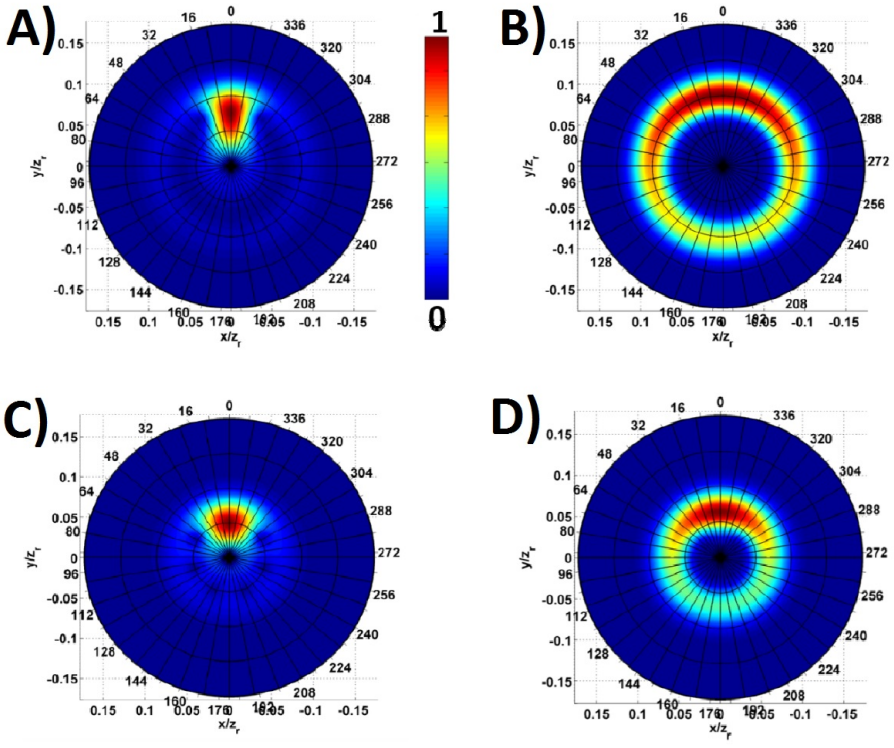

Figure 4.1: Plots of the superposition of concordant, consecutive and coherent OAM modes. Normalized intensity of scalar field for A), B) $N = 16$, ℓ_{min} = 1 and for C), D) $N = 7$, $\ell_{min} = 1$. In the left column the superpositions have $A_\ell = \sqrt{2/(\pi|\ell|!)}$ while in the right column $A_\ell = 1$.

On the contrary, in the second case, $A_\ell = \sqrt{\frac{2}{\pi|\ell|!}}$ depends on the OAM value, ℓ, of each single mode. With this choice, Eq. 4.2.2 becomes:

$$u_{tot}(\rho,\phi,0) = \frac{1}{w_0} e^{-\frac{\rho^2}{w_0^2}} \sum_{\ell=\ell_{min}}^{\ell_{max}} \sqrt{\frac{2}{\pi|\ell|!}} \left(\frac{\rho\sqrt{2}}{w_0}\right)^{|\ell|} e^{-i\ell\phi} \tag{4.2.4}$$

Here, the presence of a factor $1/\sqrt{|\ell|!}$, in the term A_ℓ, normalizes each single beam to unitary power. Moreover, it leads to a different intensity and phase distribution of the superposition field with respect to the case where A_ℓ is constant, as reported in Fig. 4.1. In fact, (Fig. 4.1), the resulting intensity distributions are no longer symmetric with respect to the propagation axis and, those weighted by the factorial term, $1/\sqrt{|\ell|!}$, result mainly concentrated in a very restricted angular domain. On the other hand, with a constant A_ℓ term, it is not possible to concentrate the power of the beam within a restricted angular region.

For this reason, only the superposition for which the intensity is concentrated in a restricted angular domain, namely when $A_\ell = \sqrt{\frac{2}{\pi|\ell|!}}$, will be examined in the following.

4.3 Superpositions radial divergence

The most interesting parameters to characterize the resulting distribution of the superposition beam are the angular spread, θ_{far}, and radial position, $s(z)$, of the field maximum size at fixed z-axis plane, with respect to the optical axis (see Fig. 4.2).

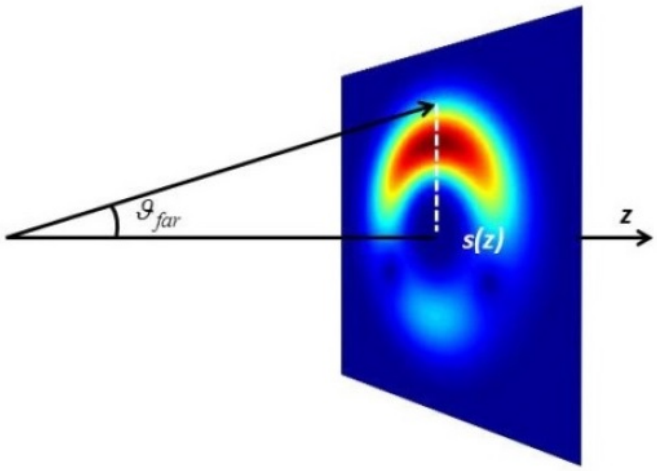

Figure 4.2: Schematic representation of angular, θ_{far} and radial, $s(z)$, position of the resulting beam.

One way to calculate these quantities is by means of the Wigner function which provide a full description of the resulting field using both spatial coordinates $\mathbf{r}$ and momentum ones $\mathbf{p}$,

simultaneously. Before starting the calculations, it is useful to recall that the circular spot size of a Gaussian beam, expressed by:

$$w(z) = w_0\sqrt{1+\left(\frac{\lambda z}{\pi w_0^2}\right)^2}, \tag{4.3.1}$$

has a simple physical meaning only for the fundamental mode, $\ell = 0$, when the light beam has a Gaussian intensity profile [123, 124] and can be thus related to the divergence of the beam itself. In fact, in this case, the beam waist $w(z)$ represent the distance from the propagation axis in which the field amplitude is $1/e$ times its maximum value. It is evident that Eq. 4.3.1 is independent of order ℓ of the LG modes, so for Gaussian beams with higher order ($\ell \geq 1$), this expression gives an inaccurate estimate of the beam geometric properties in the propagation. To overcome this approximation and obtain a more detailed and general description of the beam superposition, it may be useful to use an analytic approach based on the Wigner distribution of the scalar field. The Wigner distribution contains information regarding both the spatial distribution and the angular spectrum (App. A) of a field and is a tool widely used in optics and applied for the analysis of coherent and partially coherent beams. A more detailed description of the Wigner function can be found in [125, 126, 127, 128, 129, 130].

The first application of this tool to arbitrary light beams, in particular to an arbitrary superposition of Hermite-Gaussian (HG) modes, was discussed in [131, 132], whereas the Wigner representation of LG beams can be found in [133]. Following the approach in [133, 134], the Wigner distribution for the resulting field superposition of consecutive and concordant LG modes can be expressed, at the beam waist plane ($z = 0$), in terms of a series as in Eq. 4.2.2:

$$W_{LG}^{TOT}(\mathbf{r},\mathbf{p},0) = \sum_{\ell=\ell_{min}}^{\ell_{max}}\sum_{n\geq\ell}^{\ell_{max}} W_{LG}^{(\ell,n)}(\mathbf{r},\mathbf{p},0) \tag{4.3.2}$$

where each summing term is given by:

$$\begin{aligned} W_{LG}^{(\ell,n)}(\mathbf{r},\mathbf{p},0) = &\left(\frac{2^{\frac{|\ell-n|}{2}}(-1)^\ell 4}{\lambda^2}\right)\sqrt{\frac{\ell!}{n!}}\left[\frac{x-iy}{w_0} + \mathtt{sign}(\ell-n)\frac{\pi w_0}{\lambda}(p_y - ip_x)\right]^{|\ell-n|}\cdot \\ &L_\ell^{|\ell-n|}\left[2\left(\frac{x^2+y^2}{w_0^2} + \frac{\pi^2 w_0^2}{\lambda^2}(p_x^2+p_y^2)\right) - \frac{2\pi}{\lambda}(xp_y - yp_x)\right]\cdot \\ &\exp\left(-2\frac{x^2+y^2}{w_0^2} - 2\frac{\pi^2 w_0^2}{\lambda^2}(p_x^2+p_y^2)\right) \end{aligned} \tag{4.3.3}$$

The quantity $W_{LG}^{(\ell,n)}$ is the Wigner function (WF) of the mix between two arbitrary coherent LG modes with angular indexes ℓ and n. So, the case where $n = \ell$, $\left(W_{LG}^{(\ell,\ell)}\right)$, corresponds to that of a single mode with angular index equal to ℓ. $\mathbf{r} \equiv (x, y)$ and , $\mathbf{p} \equiv (p_x, p_y)$ are the transversal variable in coordinate and momentum space, respectively. Eq. 4.3.3 is written only for $z = 0$ but

the general case $z > 0$ can be accounted for by means of a simple change of arguments i.e.:

$$W(\mathbf{r}, \mathbf{p}, z) = W(\mathbf{r} - \lambda z \mathbf{p}, \mathbf{p}, 0) \tag{4.3.4}$$

owing to a general property of the Wigner formalism [125]. Using Eq. 4.3.2, the total intensity according to the normalization factor in Eq. 4.2.4, that is invariant under free space propagation, is equal to:

$$I = \int\int\int\int_{\mathbb{R}^4} W_{LG}^{TOT}(\mathbf{r}, \mathbf{p}, 0) d\mathbf{r} d\mathbf{p} = N \tag{4.3.5}$$

Similarly, the analytical expression for the radial and angular dimension of the resulting beam spot can be determined first by integrating on momentum and space coordinates, respectively, and then by averaging the resulting WF over the polar coordinates. The analytical expression for the spot size position of the emitted beam at fixed z-axis is:

$$\begin{aligned} s(z) = \sqrt{\frac{2\langle r^2 \rangle}{I}} &= \left(\frac{2}{I} \int_0^{\infty} \int_{-\pi}^{\pi} \int_{-\infty}^{+\infty} \int_{-\infty}^{+\infty} r^2 W_{LG}^{TOT}(r, \mathbf{p}, z) r dr d\phi_r d\mathbf{p} \right)^{\frac{1}{2}} \\ &= \left(\frac{2}{I} \int_0^{\infty} \int_{-\pi}^{\pi} \int_{-\infty}^{+\infty} \int_{-\infty}^{+\infty} r^2 \sum_{\ell=\ell_{min}}^{\ell_{max}} W_{LG}^{(\ell,\ell)}(r, \mathbf{p}, z) r dr d\phi_r d\mathbf{p} \right)^{\frac{1}{2}} \\ &= w(z) \sqrt{\frac{N + 2\ell_{min} + 1}{2}} \end{aligned} \tag{4.3.6}$$

and for the far field angle of divergence, that is expected to be invariant to axial position z, is

$$\begin{aligned} \theta_{far} = \sqrt{\frac{2\langle p_r^2 \rangle}{I}} &= \left(\frac{2}{I} \int_0^{\infty} \int_{-\pi}^{\pi} \int_{-\infty}^{+\infty} \int_{-\infty}^{+\infty} p^2 W_{LG}^{TOT}(r, \mathbf{p}, 0) r dr d\phi_r d\mathbf{p} \right)^{\frac{1}{2}} \\ &= \left(\frac{2}{I} \int_0^{\infty} \int_{-\pi}^{\pi} \int_{-\infty}^{+\infty} \int_{-\infty}^{+\infty} p^2 \sum_{\ell=\ell_{min}}^{\ell_{max}} W_{LG}^{(\ell,\ell)}(r, \mathbf{p}, 0) r dr d\phi_r d\mathbf{p} \right)^{\frac{1}{2}} \\ &= \sqrt{\frac{\lambda^2}{\pi^2 w_0^2} \left(\frac{N + 2\ell_{min} + 1}{2} \right)} \end{aligned} \tag{4.3.7}$$

Moreover, θ_{far} can be calculated also as $\theta_{far} = \lim_{z \to \infty} s(z)/z$ [127].

The sums in equations 4.3.6 and 4.3.7 have non-zero values only for $W_{LG}^{(\ell,\ell)}$ while the mixing terms $W_{LG}^{(\ell,n)}$ with $n \neq \ell$ integrate to zero because of the orthogonality condition proper of the OAM modes [5]. The factor 2, which is present in the first line of both Eqs. 4.3.6 and 4.3.7, has been first introduced in [124] for the characterization of the illuminated area of a single LG mode. This area has been defined as a circle having, as radial dimension, the standard deviation of $\sqrt{2}r/\sqrt{I}$ on a plane of constant z. A similar definition can be found in [135] where $\langle r^2 \rangle = 2\langle x^2 \rangle = 2\langle y^2 \rangle$ holds. The average value of the second order quantities have been calculated with respect to the origin of coordinates by adopting the assumption used in [124], i.e., by setting the averaged quantities $\langle x \rangle$, $\langle y \rangle$, $\langle z \rangle$ to zero, considering the standard deviation with respect to the origin of the

coordinates instead of the physical “center of mass”. In this way, the illuminated area of the total beam in any plane of constant z is contained within a circle having circumference of $2\pi s(z)$. This area linearly increases with the distance z when it is far from the Rayleigh distance, which is the typical behavior of Gaussian beams [132]. For $N = 1$ and $\ell_{min} = 0$, that describe the fundamental Gaussian mode, Eq. 4.3.6 reduces to the circular spot size described by Eq. 4.3.1. In Fig. 4.3, some examples of the evolution of $s(z)$ are shown at different distances z for different number of superimposed OAM modes, having fixed the beam waist and $\ell_{min} = 1$. As can be observed,

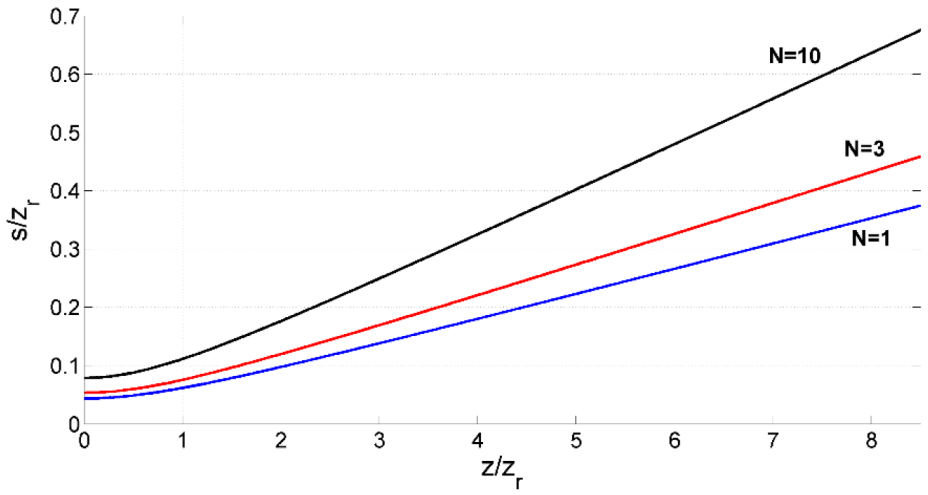

Figure 4.3: Examples of $s(z)$ at different distances z for different number of superimposed OAM modes. All the OAM modes have the same beam waist w_0 and their ℓ-values are concordant and consecutive. z and $s(z)$ are normalized with respect to the Rayleigh distance z_r.

the bigger is N the larger are $s(z)$ and θ_{far}. Moreover, the terms $s(z)$ and θ_{far} depend on the smallest value of the superposed OAM modes, ℓ_{min}. The larger is the value ℓ_{min}, the farther the illuminated spot spreads from the optical axis.

4.4 Superposition angular divergence

The angular (azimuthal) aperture of the superposed beams depends on the number of the superposed modes N and on the minimum value of OAM, ℓ_{min}. To quantify how much the spot is angularly concentrated a new quantity Θ is defined to describe the field azimuthal spread.

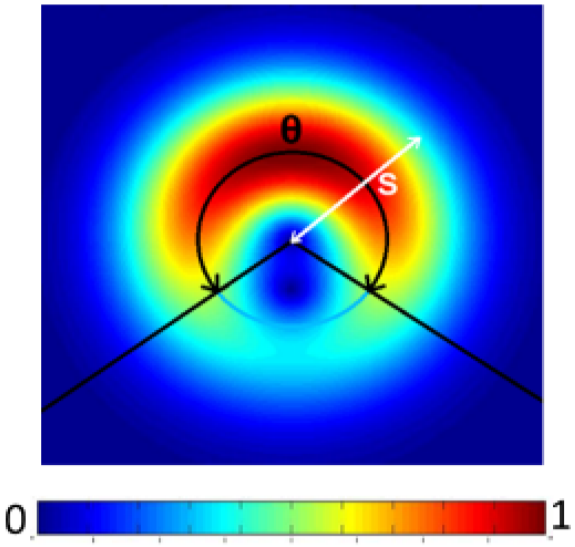

Figure 4.4: Example of the angular divergence Θ.

The total azimuthal angle of the intensity pattern Θ is given by

$$\begin{aligned}\Theta = 2\sqrt{\langle\phi^2\rangle} &= 2\left(\frac{1}{I}\int_0^{\infty}\int_{-\pi}^{\pi}\int_{-\infty}^{+\infty}\int_{-\infty}^{+\infty}\phi^2 W_{LG}^{TOT}(r,\mathbf{p},0)rdrd\phi d\mathbf{p}\right)^{\frac{1}{2}} \\ &= 2\left(\frac{1}{I}\int_0^{\infty}\int_{-\pi}^{\pi}\int_{-\infty}^{+\infty}\int_{-\infty}^{+\infty}\phi^2\sum_{\ell=\ell_{min}}^{\ell_{max}}\sum_{n=\ell_{min}}^{\ell_{max}} W_{LG}^{(\ell,n)}(r,\mathbf{p},0)rdrd\phi d\mathbf{p}\right)^{\frac{1}{2}} \\ &= 2\sqrt{\frac{\pi^2}{3}+\frac{1}{N}\sum_{\ell=\ell_{min}}^{\ell_{max}}\sum_{n>\ell}^{\ell_{max}}\frac{4(-1)^{n-\ell}\Gamma\left(\frac{\ell+n+1}{2}\right)}{(n-\ell)^2\sqrt{\ell!n!}}}\end{aligned} \tag{4.4.1}$$

where $\Gamma(.)$ is the Gamma function. Differently from Eqs. 4.3.5-4.3.7 the sum mixing terms ($W_{LG}^{(\ell,n)}$ with $n \neq \ell$) in Eq. 4.4.1 do not integrate to zero because of the ϕ^2 term as part of the integrand function.

The intensity distribution, $|u_{tot}|^2$, normalized as Eq. 4.2.4 (see also Fig. 1) on a plane perpendicular to the propagation direction z, presents an azimuthal symmetry, at $z = 0$, with respect to the axis defined by $\phi = 0$. This stems from the fact that the product of the mixing terms of the intensity are $\prec f(r)\cos\left[\phi(n-\ell)\right]$ with $-\pi < \phi < \pi$, and so the mean value of ϕ is null, namely, $\phi = 0$. The effect of the Gouy term of Eq. 4.2.1 is a $0 \leq \zeta(z) < \pi/2$ rotation of the total intensity pattern, without affecting the field distribution, and so the intensity distribution at fixed z keeps the azimuthal symmetry but with respect to the set of axis defined by $\phi^{'} = \phi + \zeta(z)$ [7]. If one wants to calculate the integral of Eq. 4.4.1 for $z > 0$, it is mathematically convenient to define the origin of the angular coordinate as the physical symmetry axis $\phi^{'} = \phi + \zeta(z)$ due to the

Gouy effect of rotation. In this way, the product of the mixing terms of the total intensity results $\propto f(r)\cos\left[\phi^{'}(n-\ell)\right]$ with $-\pi < \phi^{'} < \pi$ and the mean value $\phi^{'}$ is null. So, one can remove the dependence on $\phi^{'}$, with the same result of Eq. 4.4.1, by calculating $\sqrt{\langle\phi'^{2}\rangle - \langle\phi'\rangle^{2}}$, which is a clear measure of the standard deviation of the azimuthal spread angle. In other words a rigid rotation of the intensity pattern, as the only effect of Gouy phase when $z > 0$, does not modify the angular aperture Θ, as expected. From these argumentations, Eq. 4.4.1 is calculated at $z = 0$, for convenience. Analogously to the definition of the variable $s(z)$, the parameter Θ describes the angular standard deviation within which the illuminated area is angularly confined. However, the angular aperture is preserved during the beam propagation. It is also inversely dependent on the number of superposed OAM modes N. The larger is N, the smaller is the angular aperture of the resulting illuminated spot. In Fig. 4.5, the relationship between N and the angular aperture of the spot is shown. As can be noticed, the parameter Θ decreases as N increases and it is

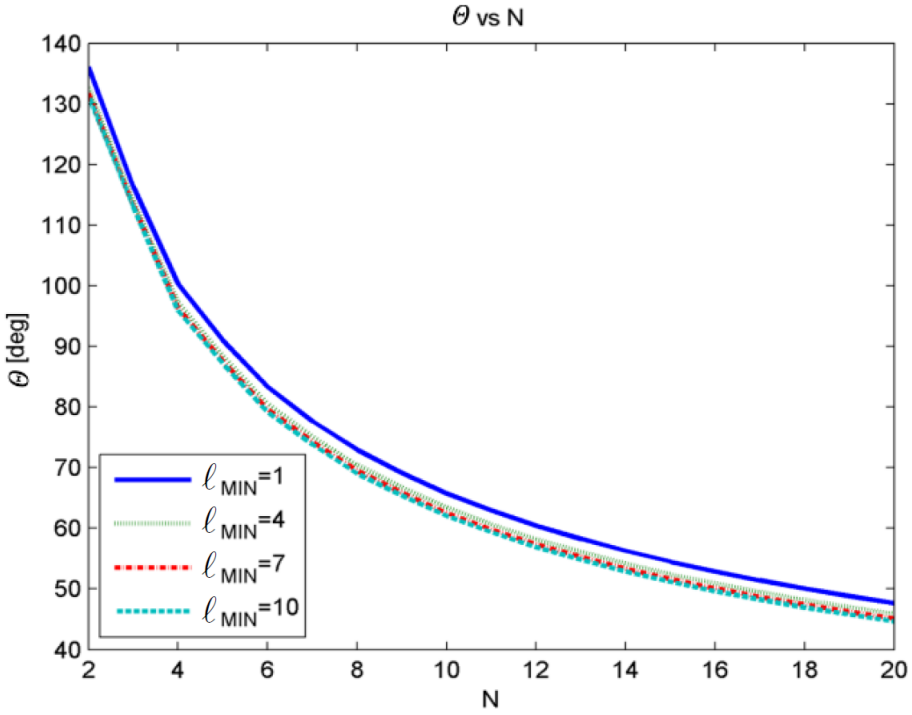

Figure 4.5: Graphic representation of the relationship between the angular aperture Θ and the number of superimposed OAM modes N at several values of ℓ_{min}.

quite unaffected by the lowest order beam ℓ_{min}. This implies that the second term in Eq. 4.4.1 has a remarkable dependence on N while the factor $(-1)^{(n-\ell)}$ is the only quantity responsible for the interference pattern between the mixing terms creating the angular confinement. In other words, it is possible to control the angular aperture of a superposition of coherent, concordant

and consecutive LG beams by acting only, (in a first approximation), on the number of modes N.

4.5 Field phase gradient

The phase embedded within the angular region described by Θ can be controlled by acting on the superposition parameters ℓ_{min} and N. Fig. 4.6 reports an example of phase maps, plotted on a plane with $z = 0$. The value of the total topological charge observed in the plots is equal to the

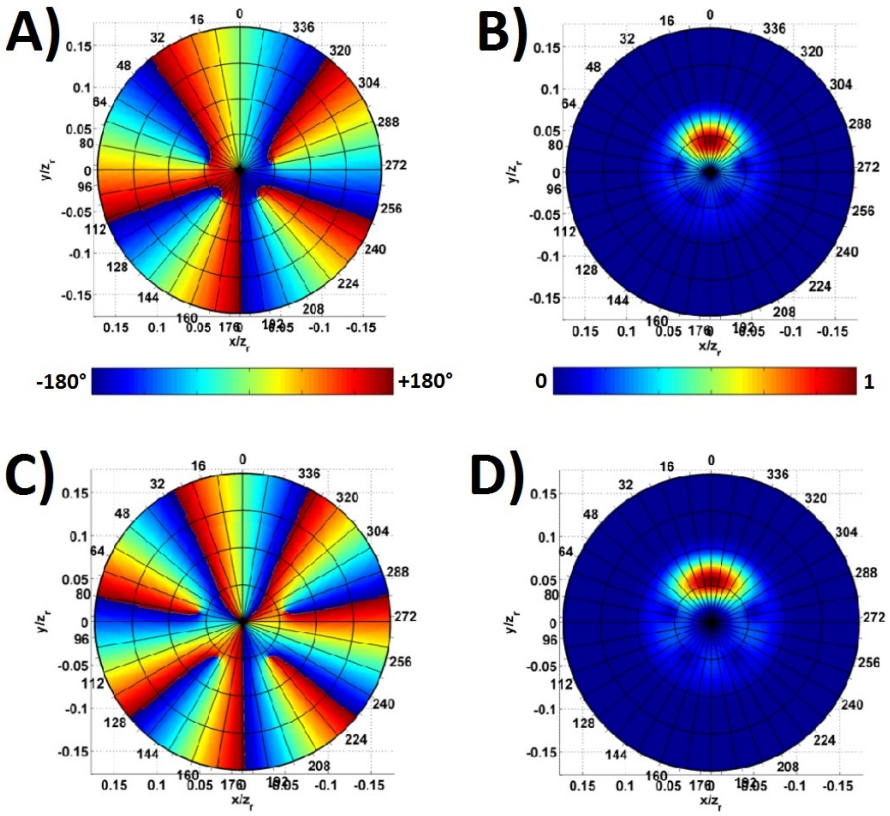

Figure 4.6: A) phase and B) intensity plots for $N = 5$ and $\ell_{min} = 1$. C) phase and D) intensity plots for $N = 5$ and $\ell_{min} = 3$.

maximum number of OAM modes, ℓ_{max}, whereas the number of singularities is equal to N. The location of the phase vortices in this field is obtained by finding the set of points (r_s, ϕ_s) where the following condition is satisfied [136, 137]:

$$\arctan\left(\frac{\Im\big(E_{tot}(r,\phi)\big)}{\Re\big(E_{tot}(r,\phi)\big)}\right) = 0 \tag{4.5.1}$$

Table 4.1: Resuming table

N	ℓ_{min}	ℓ_{max}	Θ	β	β_m	$\Delta\phi_{eff}$
4	2	5	99	72	91	1.3
	9	12	96	30	32	3.2
	15	18	96	20	20	4
8	2	9	72	40	52	1.8
	9	16	69	22.5	25	2.9
	15	22	68	16.4	17	5.2

where $E_{tot}(r,\phi)$ is given by Eq. 4.2.4 and the index s gives the s-th singularity. One of the vortex is always located at the center $r = 0$ and this singularity is of the order ℓ_{min} as can be deduced from Eq. 4.2.2; for $r \neq 0$ the other singularities, hereafter called secondary singularities [137], are present in a number of $|\ell_{max} - \ell_{min}|$. As a consequence, in the central zone, the phase is distributed as the phase of a pure OAM of value ℓ_{min} whereas in the zone far from the center (starting from a certain value of $r \equiv \tilde{r}$ that corresponds to maximum value of the set r_s i.e., the radial position of the secondary singularity, which depends on the particular choice of the parameters N and ℓ_{min}) the whole phase is distributed as the phase of a pure OAM of value ℓ_{max}. Given the definition of $\tilde{r}$, it has been numerically verified that the maximum of the illuminated area of the total beam lies on $r > \tilde{r}$, so the corresponding phase falls in the zone where ℓ_{max} is dominant.

Considering the phase distribution, two parameters can be defined. The first one, called β, identifies the angle where a variation of 360° of the phase profile is included. The second one, on the other hand, define the effective phase variation within the restricted angular domain of angular aperture Θ as $\Delta\phi_{eff} = \Theta/\beta$. For $r \gg \tilde{r}$ the angular parameter β is given by $360^\circ/\ell_{max}$. So, it is possible, with good accuracy, to predict the total phase variation within a fixed angle when the intensity distribution is far from the optical axis. The above condition is fulfilled for large values of ℓ_{min} (see Eqs. 4.3.6 or 4.3.7). In particular, as proved by numerical simulations, it is fully satisfied just when $\ell_{min} > 2$. On the contrary, in the case of $\ell_{min} = 1, 2$ the expression $360^\circ/\ell_{max}$ is no longer a good approximation for β. In fact, for these values of ℓ_{min}, the illuminated spot is concentrated in a zone where $r \approx \tilde{r}$. In this zone the phase variation is not equally distributed and so the angle embedding the 360° phase variation, β , is not constant. Below, some examples that show the effective phase variation embedded in the region with angular aperture Θ are reported. In particular, N is fixed to 4 and 8 that in good approximation, as stated above, is equivalent to fix the angular aperture of the spot in Θ; ℓ_{min} is changed. Table 4.1 reports the cases for $\ell_{min} = 2, 9, 15$. Numerical data confirm that the angular spot of light in Θ is quite the same for different values of ℓ_{min} having fixed N. On the contrary, the most striking effect obtained by varying ℓ_{min}, and so ℓ_{max}, is to concentrate the phase variation in the angular region described by the parameter Θ as can be seen by considering the parameter β. In addition to

β, another parameter is calculated, β_n, which represents the angle embedding the $360°$ phase variation at $r = s(z)$ obtained from numerical calculations. The quantity $\Delta\phi_{eff} = \Theta/\beta_n$ gives the effective number of the phase variations of $360°$ inside the angular region delimited by Θ. From the comparison between β and β_n it is confirmed that $360°/\ell_{max}$ is not a good approximation for low ℓ_{min} ($= 2$ in the reported examples) whereas for larger ℓ_{min} it is a meaningful quantity which can be used for the prediction of the number of phase variation within a fixed angle Θ of interest. Fig. 4.7 reports the phase embedded in Θ, measured at $r = s(z)$ for the cases resumed in Table 4.1. Each line represents, for different ℓ_{min}, how many times the phase changes between $0°$ and $360°$ within the angular region Θ. The value of Θ sets the angular limits reported in abscissa.

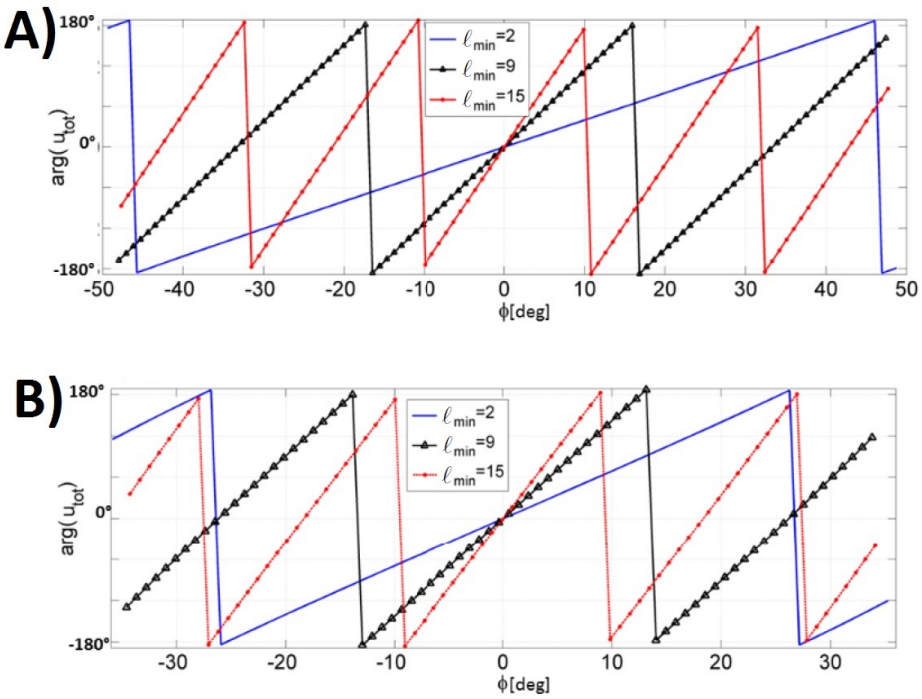

Figure 4.7: Simulation of the phase variation embedded in the angular region Θ measured at distance s from the center for three different values of ℓ_{min}. A) $N = 4$ and B) $N = 8$.

4.6 Conclusions

In this chapter it has been examined a method to control the field distribution generated by the superposition of coherent, consecutive and concordant LG modes. This smart combination of beams, weighted by a factorial normalization factor so that each mode carry the same power, leads to the concentration of the EM field in a restricted angular region. To evaluate the geometry

of the total field, two parameters have been defined by means of the Wigner function: the field radial divergence and the field azimuthal divergence. The first one quantify the radial position of the field maximum size and depends both by the number of superimposed beams and by the minimum topological charge ℓ_{min}. The second one, on the contrary, depends only by the number of superimposed modes. Moreover, once the number of states to be superposed is fixed, it is possible to control the number of 360° phase variations embedded within the field angular aperture by acting on the lowest topological charge of the set.

The method seems to be an interesting solution to produce smaller OAM fields with respect to single modes; its application may be particularly useful in long range OAM-based multiplexing systems, where the size of receiving fields are critical with respect to antennas dimensions. However, to determine the real efficiency of this method it is necessary to provide a full comparison with other techniques, like the MIMO ones. To answer this question, a complete analysis will be presented in Chap. 6. Before concluding, note that the method can be used also to create a custom field distribution, with particular constrain about its intensity size and its phase gradient.

Chapter 5

High-order OAM beams

This chapter presents a novel technique, based on dielectric masks and conformal parabolic antennas, to generate high-order vortex beams in the radio frequency domain. To study the main aspects of the generation process, two experiments have been performed with a custom antenna prototype, designed looking at the mathematical description of such beams. High-order modes, in fact, present a more compact main lobe with respect to corresponding single modes and may represent an interesting tool to improve the orthogonality exploitation on long range OAM-based multiplexing links.

RELATED PAPERS

Spinello, F., Parisi, G., Tamburini, F., Massaro, G., Someda, C. G., Oldoni, M., Ravanelli, R. A., Romanato, F. & Mari, E. (2015). *High-order vortex beams generation in the radio-frequency domain*. Antennas and Wireless Propagation Letters, IEEE, 99.

5.1 Introduction

The previous chapter presented a method to reduce the size of an OAM field by means of proper superpositions of LG beams. The method was designed to help the exploitation of OAM modes orthogonality over long distances, when it is difficult to receive the whole transmitted fields due to the small size of antennas (Chap. 3). Consecutive superpositions of LG beams may be a first option to solve this problem, however, also other solutions, as high-order vortex beams, can be adopted.

As will be presented in next section, these particular OAM beams are characterized by an intensity profile with concentric rings and by interlaced spiral phase fronts. Moreover, their main lobe, (the innermost ring), is more compact with respect to equivalent single modes carrying the same OAM quantity. For this reason, high-order beams may represent a second interesting tool to improve OAM orthogonality exploitation in long range links.

In this chapter, the structure of high-order vortex beams is examined by means of LG modes with radial index $p \neq 0$ and a novel generation process for the radio frequency domain is analyzed. Up to now, in fact, this family of beams has been considered only in optics [138, 139, 140] where they have been produced using either suitably modified spatial light modulators or spiral phase plates [139]. Here, after a theoretical analysis, vortex beams with non-null radial index are produced by means of dielectric masks, mounted upon either twisted parabolic reflectors or conventional ones. Moreover, the produced far-field intensity patterns are compared with analytical models and numerical simulations, thus illustrating the main aspects that influence the generation process.

5.2 Laguerre-Gauss p-modes

As presented in the first chapter, the field of a LG beam is characterized by a symmetric circular distribution and can be described, in a cylindrical reference system (ρ, ϕ, z), as:

$$u_{p,\ell}(\rho,\phi,z) = A\frac{1}{w(z)}\left(\frac{\sqrt{2}\rho}{w(z)}\right)^{|\ell|} L_p^{|\ell|}\left(\frac{2\rho^2}{w(z)^2}\right)\cdot \\ \cdot \mathrm{e}^{-\rho^2/w(z)^2}\mathrm{e}^{\frac{-ik\rho^2}{2R(z)}}e^{i\left(2p+|\ell|+1\right)\zeta(z)}e^{-i\ell\phi}, \tag{5.2.1}$$

where $w(z) = w_0\sqrt{\left(1+z^2/z_R^2\right)}$ is the beam width, w_0 is the beam waist, z_R is the Rayleigh distance, $R(z)$ is the wavefront curvature radius, $\zeta(z) =$*arctan*(z/z_R) is the Gouy phase [32], and $L_p^{|\ell|}(.)$ is the generalized Laguerre polynomial [25]. The ℓ parameter, as just said, is responsible for the amount of OAM carried by the field. On the other hand, the p one acts on the order of the Laguerre polynomial regulating the field intensity distribution. The p parameter is the so called

radial index because it determines the number of zeros of the Laguerre polynomial and so the radial nodes in the field's intensity, which appears to be composed by a series of concentric rings. In fact, an LG beam with $p \neq 0$ is characterized by an intensity pattern with p concentric null rings around the axis of propagation. Moreover, if $\ell \neq 0$ there is also a central null due to the phase singularity. Similarly, also the field phase distribution is characterized by adjacent concentric rings

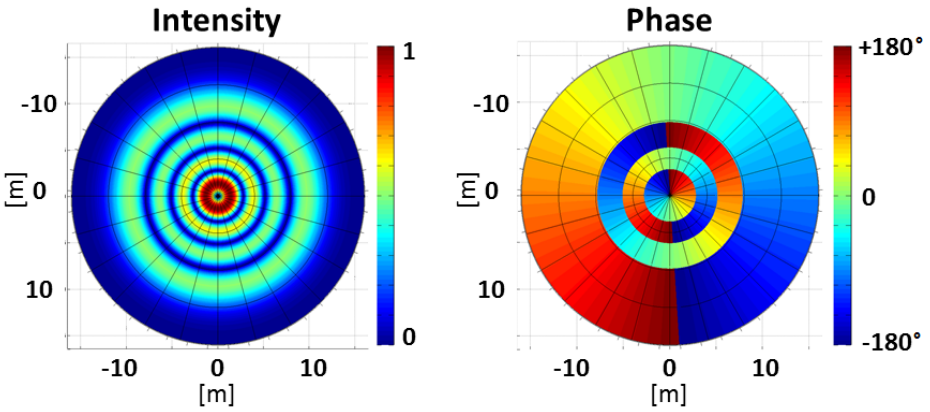

Figure 5.1: Example of a high-order LG beam with $\ell = 1$ and $p = 3$.

radially out of phase of π. This spacial behavior is induced by the Laguerre polynomial which reverse its phase after each null. Due to their particular field structure, LG beams characterized by $p > 0$ are also called high-order LG beams. An example can be observed in Fig. 5.1.

Among all parameters, the p one is the most interesting for squeezing the field size. To better understand this fact, it may be useful to consider a practical example where two LG beams, with same OAM and different radial index, are considered. More in detail, both beams carry the same OAM quantity ($\ell = 3$) while $p = 0$ for the first beam and $p = 2$ for the second one. Looking at the two field distributions, in a plane perpendicular to the propagation direction (z =cost.), it appears that the main lobe of the $p = 2$ beam is narrower than the other one. This particular behavior, that can be observed in Fig. 5.2, is caused by the different order of Laguerre-Gauss polynomial.

From Fig. 5.2, it is also cleat that the concentration effect is limited only to the main lobe of the field. On the contrary, the total surface filled by the $p = 2$ beam is wider with respect to the one filled by the $p = 0$ beam. For this reason, the use of high-order modes in a long range system leads to a bigger energy waste with respect to traditional OAM modes (the fields spread in bigger areas). However, in spite of that, a larger energy waste can be refunded by a higher communication capacity due to the exploitation of modes orthogonality.

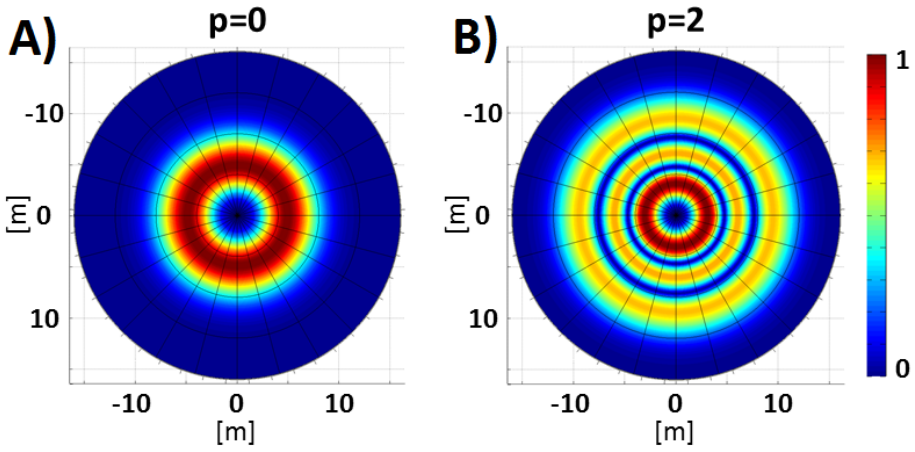

Figure 5.2: Intensity distribution of A) $\ell = 3$, $p = 0$ beam and B) $\ell = 3$, $p = 2$ beam.

5.3 The generation process

High order vortex beams generation can be performed by using dielectric masks mounted either on a standard parabolic reflector or on conformal ones. The phase structure $\varphi(\rho, \phi)$ of a $p \neq 0$ LG mode, characterized by a π-phase discontinuity between each radial node, can be easily deduced from Eq. 5.2.1. It results that:

$$\varphi(\rho, \phi) = -\ell\phi + \pi\theta\big(-L_p^{|\ell|}(2\rho^2/w_0^2)\big) \tag{5.3.1}$$

where $\theta(x)$ is a unit-step function, taking the value -1 for $x < 0$, and 0 elsewhere.

A dielectric mask can be designed to play the role of inducing the second term on the right-hand side of Eq. 5.3.1, whereas the first term can be imprinted either by a standard parabolic antenna ($\ell = 0$) or by a twisted one ($\ell \neq 0$). Since the LG polynomial $L_p^{|\ell|}(2\rho^2/w_0^2)$ reverses its phase after each null, it is clear that the dielectric mask will be composed by concentric rings, as illustrated by Fig. 5.3.

5.4 A prototype antenna design

To test this new method, it has been designed and built a $p = 4$ dielectric mask to convert an input plane wave into the desired phase profile. The mask, designed to work at the frequency of 17.2GHz, is a grating composed by concentric rings, drilled with a numerical-control milling machine into a cylindrical layer of polyethylene (see Fig. 5.5). The mask design requires two parameters to be fixed: the beam waist, w_0, and the height, h, of the dielectric grating. The first parameter is responsible for the beam size at the origin plane $z = 0$; it has to be chosen in such

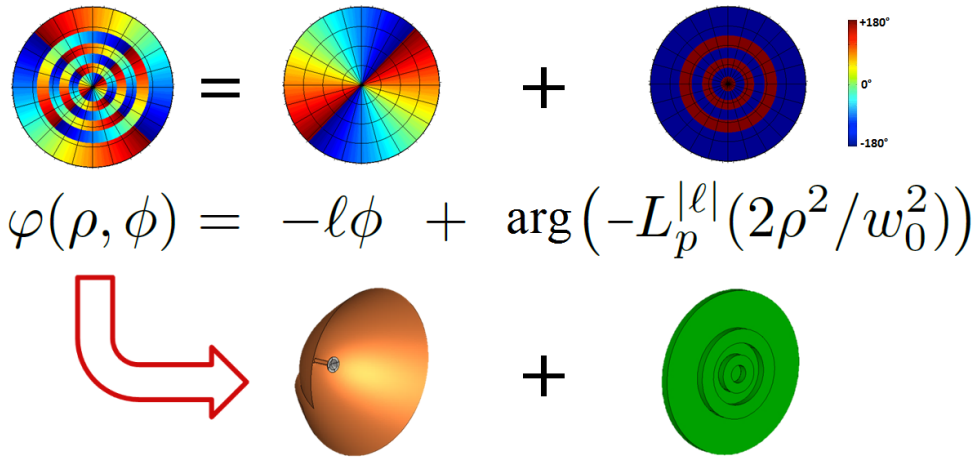

Figure 5.3: Antenna structure for the generation of high-order vortex beams.

a way that the mask can be illuminated completely. In this specific case, it has been chosen such that the entire dielectric structure is contained within the mouth of a standard parabolic reflector (360mm diameter). Thus, it has been set $w_0 = 50$mm. This choice, while satisfying the strict requirement for the dielectric mask to be limited in its lateral size (the outermost ring falls at a distance of ≈ 120mm from the center), leads, however, to a distance between adjacent rings comparable with wavelength, λ. Unfortunately, this could reduce the degree of paraxiality (App. B) of the generated field, causing a mismatch between experimental and theoretical data. It is an important aspect to be accounted during the data post-processing. On the other hand, the second parameter h was taken in order to induce complete destructive interference in correspondence of the p rings. To make this, it is necessary, for the phase delay of the fields emerging from two consecutive rings, to be equal to π in order to produce a destructive interference. In fact, the field propagation within the grating determines the mask behavior. More in details, the EM field crosses a ring height in a time t equal to

$$t = \frac{n}{c}h, \tag{5.4.1}$$

where c is the light speed and n the refraction index of the mask material; (c/n is the wave speed). For this reason, the fields crossing a ring acquire a phase delay $\delta\Phi$ equal to:

$$\delta\Phi = 2\pi\frac{n}{\lambda}h. \tag{5.4.2}$$

Now, forcing a phase difference of π between two adjacent rings, (remember that one ring is composed of dielectric material and the adjacent one is composed by air), it results that:

$$h = \frac{1}{2}\frac{\lambda}{n - n_0}. \tag{5.4.3}$$

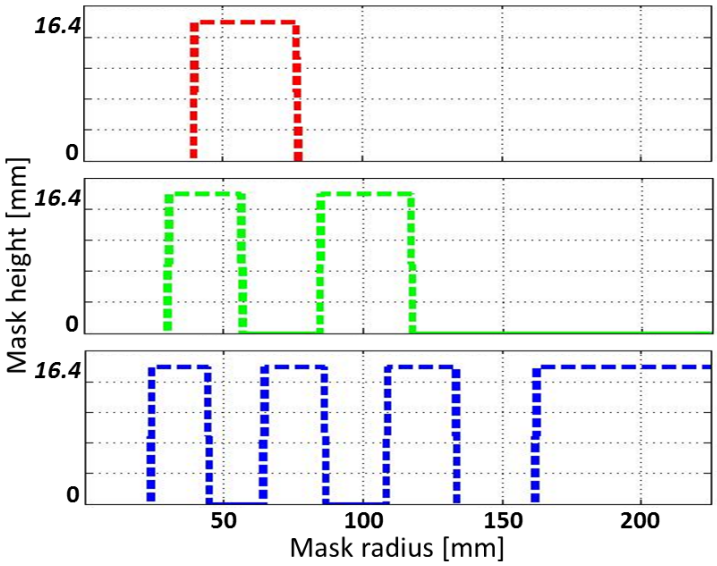

Figure 5.4: Mask profiles for the generation of $p = 2$ beams (red), $p = 4$ beams (green) and $p = 7$ beams (blue). The profiles are obtained from Eq. 5.3.1 with $w_0 = 50$mm, $\ell = 0$.

Since a polyethylene substrate with $n = 1.53$ has been used, $n_0 = 1$ and $\lambda = 17$mm, it results $h = 16.4$mm. An example of the mask profile can be observed in Fig. 5.4 (green line), together with the profiles of similar masks to generate $p = 2$ (red line) and $p = 7$ (blue line) beams. Finally, the $p = 4$ mask has been mounted on the mouth of two antennas: a standard parabolic one and a twisted $\ell = 1$ one (Fig. 5.5).

Notice that this approach is completely different from the optical counterpart [139], where both phase terms were implemented within a single dielectric mask.

5.5 Prototype antennas testing

To measure the generated fields, the prototype antennas have been mounted, once at time, on a computer-controlled rotator, moving both in elevation and azimuth with a resolution of $0.2°$. The transmitted sinusoidal test signal was received by a standard horn antenna, at a distance of 100m, connected to a Vector Network Analyzer (VNA). No signal post-processing was required. Afterward, the measured spatial distributions of the generated fields have been compared with far-field theoretical values. In particular, semi-analytical simulations have been performed, applying the convolution theorem $u_{in} * T_m$ [139, 141] between the closed-form expressions of both the input gaussian field $u_{in} = \exp(-i\ell\phi)\exp(-\rho^2/w_{in})$ and the mask transmission function $T_m = \texttt{sign}\big(-L_p^{|\ell|}(2\rho^2/w_0^2)\big)$. For the gaussian input beam, it has been chosen the analytical expression which best fit the parabola field, setting $w_{in} = 130$mm. This value entails that the impinging

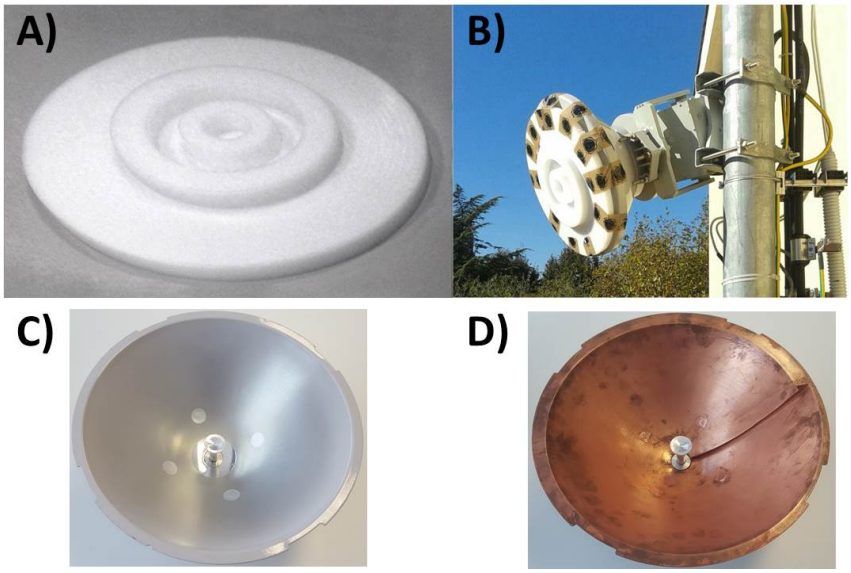

Figure 5.5: A) dielectric $p = 4$ mask, machined in polyethylene. B) the $p = 4$ mask on a standard parabolic reflector mounted on a computer-controlled rotator. C) standard parabolic reflector. D) twisted parabolic reflector.

gaussian field is entirely collected by the dielectric mask. The far field was then numerically calculated by means of a standard fast Fourier transform (FFT) routine.

5.5.1 $\mathbf{p = 4}$, $\ell = 0$ beam

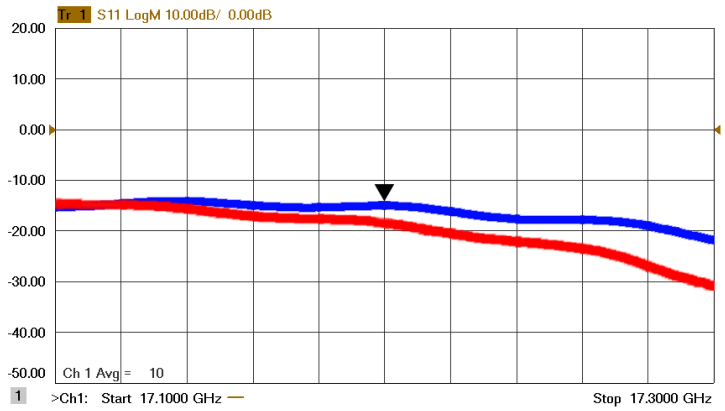

Figure 5.6: Measurement of S_{11} parameter for the $\ell = 0$, $p = 4$ antenna (blue) and for the $\ell = 1$, $p = 4$ one (red).

First, using the VNA, the S_{11} parameter has been measured when the antenna radiates in

free space. At the working frequency of 17.2GHz it results equal to -15dB, as shown by the blue curve of Fig. 5.6. Afterward, the entire generated field distribution has been examined. Fig. 5.7 reports both the numerical (see Fig. 5.7A and Fig. 5.7B) and experimental (Fig. 5.7C) results for $\ell = 0$ and $p = 4$ ($u_{4,0}$). On the other hand, Fig. 5.8 shows a comparison between profiles taken from analytical, numerical and experimental results. The experimental data have been extracted from the map shown in Fig. 5.7C, along the white solid horizontal line passing through the physical center of the generated field. For the case at hand, it has also been possible

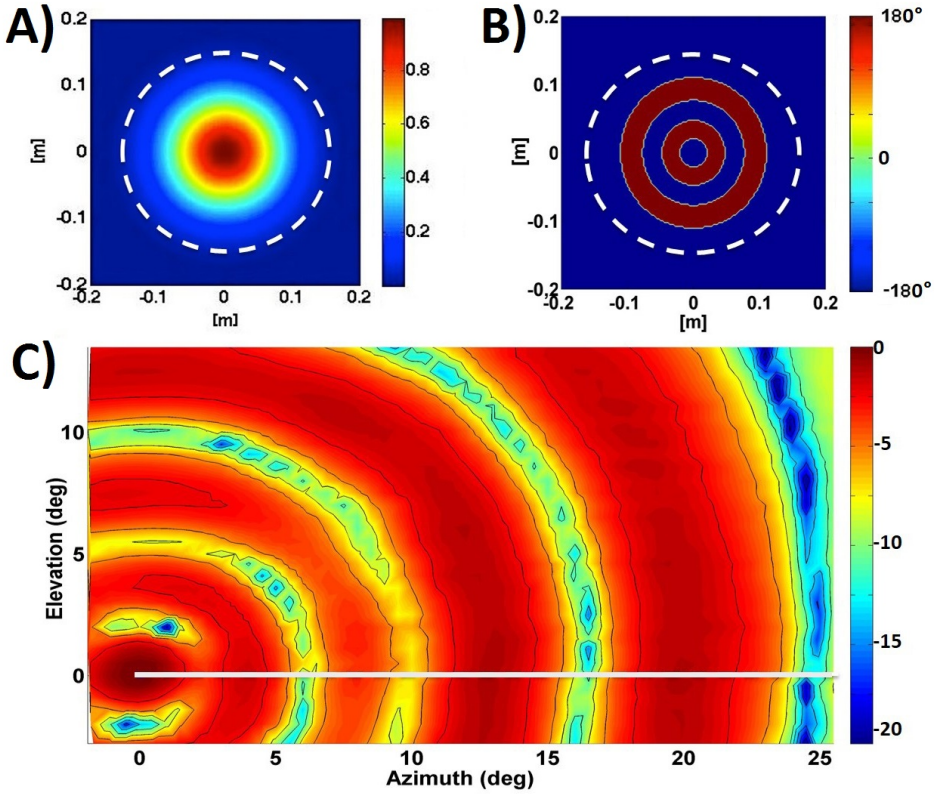

Figure 5.7: Numerical simulations: A) input field intensity $|u_{in}|^2$ and B) phase pattern of the dielectric mask for $\ell = 0, p = 4$ mode. Dashed white circles represent the edge of the parabolic reflector aperture. Experimental results: C) map of the generated intensity field. The horizontal white line represents the locus of data extraction used for Fig. 5.8.

to perform a FEM simulation with a full vectorial method. In spite of the system being electrically large, the complexity of the model can be dramatically reduced by taking into account the system axial symmetry. The profiles given by the analytical description (i.e., $u_{4,0}$, Eq. 5.2.1) and by the FFT semi-analytical one are in good agreement near the beam center, while slight discrepancies show up in the secondary rings, especially the outermost ones. This appears to be due to a non-ideal modeling of the illumination field as a Gaussian beam, u_{in}. A top-hat input beam would

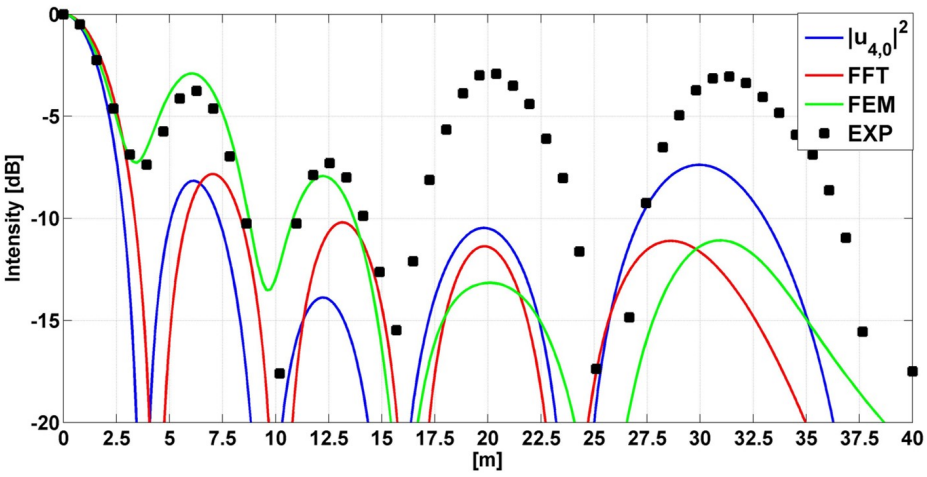

Figure 5.8: Comparison between intensity distribution of the analytic mode $u_{4,0}$ (blue solid line), the FFT semi-analytical approach (red solid line), the FEM simulation (green solid line), and the experimental data (black marks). The experimental data are taken from Fig. 5.7 along the white line; the coordinates were converted from spherical to Cartesian for having coherent units.

have lead to a better overlap with the analytical case[138]. Notice that a similar discrepancy has been observed also at optical frequencies [139]. Comparison between the $u_{4,0}$-based theory and experimental data shows larger deviations in the amplitude distribution, especially out of the central zone. This behavior is ascribed to three primary deviations from ideal conditions. The first is the already mentioned insufficient degree of paraxiality of the beam radiated by the mask. In fact, the vectorial structure of the field can significantly impair the destructive interference at the edges of the p rings. This explains why the minima of the experimental field are not as deep as those of the $u_{4,0}$ beam in the central zone. The second is a non ideal illumination of the dielectric mask due to the feeder. In fact, the field reflected by the parabola presents several diffraction orders, which are quite far from the ideal condition of illumination. This effect becomes stronger in non-central zones, where high-order scattered modes and the edge diffraction of the parabolic reflector yield significant “spurious” peaks (the third and the fourth one, in particular), compared to the analytical model. Still, despite the imperfect amplitude distribution, it is clear that the positions of the minima are in good agreement with those of the analytical model. Finally, as for the third source of discrepancy, let’s remind that transmission through the dielectric mask acts only on the phase of the field. If the LG polynomial in Eq. (5.2.1) is examined, it is clear that p affects not only the phase, but also the amplitude of the LG beams [137]. Hence, this phenomenon, although overlooked so far, is present also in the optical experiments.

Finally, FEM simulation must be examined. The three central peaks agree well with the experimental data, while the fourth and the fifth one are predicted much lower than the experimental

results. This discrepancy can be explained by insufficient knowledge of details on the antenna feeder. Indeed, while accurate information on the CAD of the dielectric mask and on the shape of the primary reflector have been inserted in FEM simulation, there was an insufficient knowledge of the geometric details of the secondary reflector and a simplified model has been adopted. For this reason, the simulated feeder reproduces faithfully the illumination in the central zone, but is not accurate enough far from the center. The FEM simulation fails in the prediction of the far-field last two peaks.

5.5.2 $\mathbf{p = 4}$, $\ell = 1$ beam

A second experiment has been performed to produce a $u_{4,1}$ beam; in this second case the $p = 4$ dielectric mask was mounted upon an $\ell = 1$ twisted parabolic reflector. This time, the S_{11} parameter is equal to -18dB at the working frequency, as shown by the red curve of Fig. 5.6. Fig. 5.9A shows the theoretically calculated intensity of the input field (u_{in}) and Fig. 5.9B the

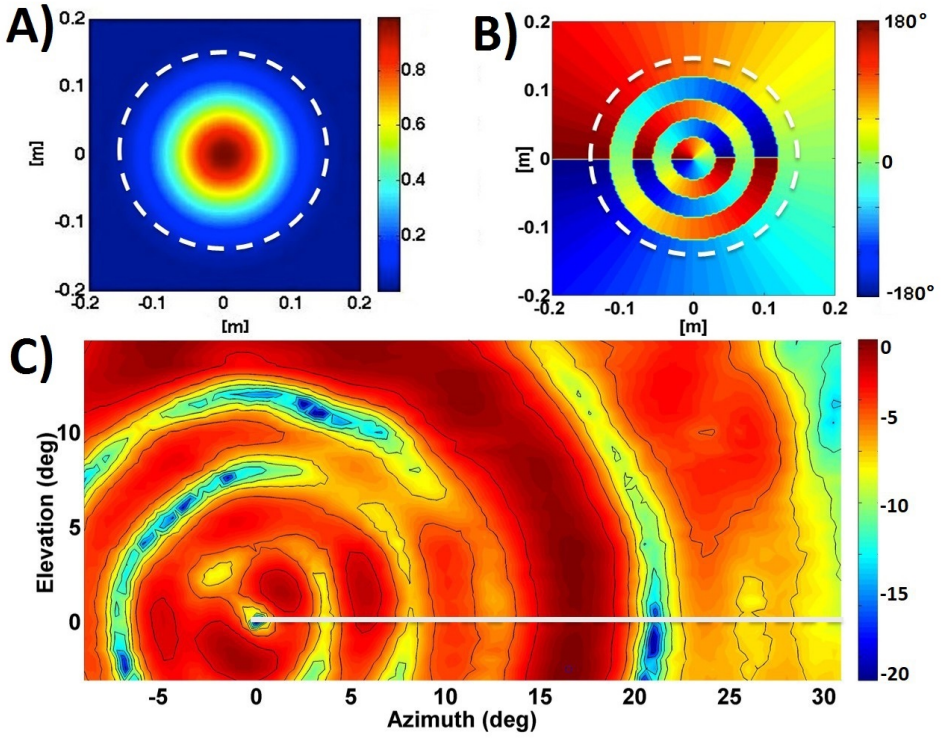

Figure 5.9: Numerical simulations: A) input field intensity $|u_{in}|^2$ and B) phase pattern for $\ell = 1, p = 4$ mode. Dashed white circles represent the edge of the reflector aperture. Experimental results: C) map of the generated intensity field. The horizontal solid white line represents the locus of data extraction. The central zone of zero intensity confirms the presence of a phase singularity, typical of an $\ell = 1$ OAM beam.

cumulative phase pattern given by the contributions of both the twisted antenna and the dielectric mask, Eq. (5.3.1). On the other hand, Fig. 5.9C reports the experimental map of the field intensity in which is visible the central zone of zero intensity that is typical of an OAM beam. The measured field distribution is less regular than in the $p = 4$, $\ell = 0$ case. This can be explained as a combination of low degree of paraxiality, and non-perfect uniform illumination. In fact, the twisted parabolic reflector further enhances the number of diffracted orders and, at the same time, this setup is more affected by misalignment errors between the dielectric mask and the twisted reflector. In other words, for the $\ell = 1$ mode the conditions are more severe with respect to the $\ell = 0$ case, as expected considering the more complicated phase distribution. Fig. 5.10 reports the comparison between theoretical, numerical and experimental results. In this case, due to the complex non-symmetric geometry, it has not been possible to perform a FEM simulation. A good match is found between the FFT and the $u_{4,1}$ curve. Comparison between the intensity

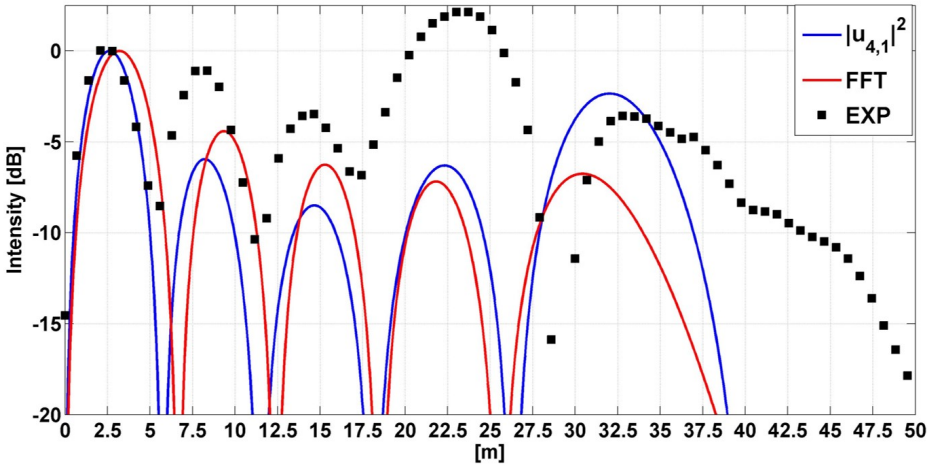

Figure 5.10: Comparison between the intensity distributions of the analytic mode $u_{4,1}$ (blue solid line), FFT semi-analytical approach (red solid line), and experimental data (black marks). The experimental data are taken from Fig. 5.9 along the white line; the coordinates were converted from spherical to Cartesian for having coherent units.

of $u_{4,1}$ and experimental result shows a good match in the central zone, but strong deviation for the fourth and fifth rings. In particular, the positions of the minima agree with the analytical model for the first three rings, but the last two are wider. Again, this behavior confirms that the effect of diffraction becomes heavy in the non-central zones, and that it is the main cause of discrepancy from the analytical solution. Similar effects are negligible in the optical domain, where the ratio between the geometric features of the mask and the wavelength is much larger.

5.6 Conclusions

LG beams with $p \neq 0$ may be interesting solutions to implement long range radio links based on OAM multiplexing. In fact, their structure seems to be promising to reduce the size of received fields. However, to verify the real efficiency of this idea, it will be presented a detailed study in next chapter.

Here, the generation of high-order beams have been made using a new technique: dielectric masks mounted either on parabolic reflectors or on traditional ones. From experiments, it has been observed that the generated fields match well the theoretical expectations in the central part of the beams, however, there are also some non-negligible and not-desired deviations in the peripheries. Mismatching is due mainly to diffraction effects, linked to the antenna and to the mask size with respect to the wavelength. A bigger source, exhibiting geometrical features several times larger than λ, should lead to a much better results, but would also occupy a much larger space region. Moreover, it has to be considered that the dielectric mask used in the experiments only modulates the field phase and not the amplitude. On the contrary, the Laguerre Polynomial within Eq. 5.2.1 modifies also the field intensity since $\left|u_{p,\ell}(\rho,\phi,z)\right| \neq 1$. Therefore, the generated beams can not be considered as LG ones but only as accurate approximated versions.

In conclusion, the generation of high-order vortex modes in the RF domain is feasible with the proposed method but, in order to yield high-accuracy beams, the relation between source size and operating wavelength must be carefully accounted for.

Chapter 6

OAM waves and MIMO systems

This chapter examines a new OAM-based multiplexing scheme studying the possibility of distinguish different OAM modes when only a small portion of the field is received. The analysis, performed using MIMO theory and a mathematical model describing the propagation of OAM beams, leads to a quantitative evaluation of OAM-based systems features. Moreover, the efficiency of the solutions proposed in the two previous chapters is examined. In the end, the communication capacities of OAM-based and MIMO-based multiplexing systems are compared under equal constraints on the antennas size.

RELATED PAPERS

Oldoni, M., Spinello, F., Mari, E., Parisi, G., Someda, C., Tamburini, F., Romanato, F., Ravanelli, R., Coassini, P. & Thide, B. *Space-Division Demultiplexing in Orbital-Angular-Momentum Based MIMO Radio Systems*. Transactions on Antennas and Propagation, IEEE, 63(10), 4582-4587.

&

Vallone, G., Parisi, G., Spinello, F., Mari, E., Tamburini, F. & Villoresi, P. *A general theorem on the divergence of vortex beams*. Submitted to Physical Review Letters.

6.1 Introduction

As already mentioned, the orthogonality property is one of the most interesting characteristics of OAM waves. It provides an additional degree of identification for EM fields and can be very useful, for telecommunications, to implement multiplexing systems and to better exploit the electromagnetic spectrum. However, to exploit the natural orthogonality of OAM modes, it is fundamental to consider the whole field distribution of an EM field [7]. In fact, as explained in Chap. 1, it is necessary to perform a closed line integral around the field propagation axis. The same procedure can not be applied on a local scale, except in few very peculiar cases [47]. While the full reception requirement can be easily satisfied for short range Line of Sight (LOS) communication systems, (see Chap. 2), it can be hardly achieved in long range LOS systems, as observed in Chap. 3. To overcome this problem, two proposals have been advanced: the first concerns the use of OAM modes superpositions to reduce the field dimensions (Chap. 4) and the second considers high order OAM modes, (Chap. 5). Nonetheless, some crucial aspects need to be clarified, for example the maximum length of an OAM-based radio link, as limited by diffraction, or the performances of OAM-based systems with respect to equivalent MIMO ones.

For all these reasons, this chapter will extensively study the orthogonality exploitation problem, with particular attention to the requirement of receiving the whole field. It will examine the possibility of distinguish different OAM modes when only a small portion of wave is received and it will draw a quantitative analysis of OAM based communication systems features. The analysis will be performed considering the MIMO formalism and looking, at the same time, at the physical structure of OAM waves. Within this study, OAM-based systems and conventional MIMO ones will be compared, under equal constraints on the size of the antennas and in a reflection-free environment.

To this purpose, a new parameter, called *phase slope* or phase gradient, will be defined to assess the capability of an antenna system to resolve overlapping beams (and so to distinguish different channels). Analytical expressions of the phase slope will be derived for a point source, for Laguerre-Gauss OAM beams, for coherent superpositions of two or more OAM modes and for a general field with OAM. The phase slopes of OAM-carrying fields will finally be compared with those obtained with conventional MIMO systems and proper conclusions will be drawn. The whole analysis stems on intrinsic properties of the transmitted field distributions, regardless of the system internal arrangement like, for example, the characteristics of antennas. Moreover, it complements and broadens the formal study made by Edfors [12], which was restricted only to circular arrays.

6.2 A new reception scheme

As explained in Chap. 1, the most popular example of OAM-carrying field is a Laguerre-Gauss beam. In cylindrical coordinates (ρ, ϕ, z), assuming that the state of polarization of the beam is uniform and represented by a constant unit vector $\hat{\mathbf{a}}$, the electric field can be expressed as:

$$E_{p,\ell}(\rho,\phi,z) = \hat{\mathbf{a}}\sqrt{\frac{p!}{\pi(p+|\ell|)!}}\frac{1}{w(z)}\left(\frac{\sqrt{2}\rho}{w(z)}\right)^{|\ell|} L_p^{|\ell|}\left(\frac{2\rho^2}{w(z)^2}\right)\cdot \tag{6.2.1}$$

$$\cdot\, \mathrm{e}^{-\rho^2/w(z)^2}\,\mathrm{e}^{\frac{-ik\rho^2}{2R(z)}}\, e^{i\left(2p+|\ell|+1\right)\zeta(z)} e^{-i\ell\phi},$$

where all the parameters keep the same meaning explained in Chap. 1. As schematically illustrated in Fig. 6.1, for a topological charge $\ell \neq 0$, a finite beam waist w_0, and a radial index $p = 0$, the radiation pattern is "doughnut" shaped: the radiated power density vanishes on axis, increases radially up to a maximum, at an angle θ_M, and then decreases monotonically to zero. Changes for a radial index $p \neq 0$ have been discussed in Chap. 5, and are not relevant to the present purpose. The phase of the field, along a circular path perpendicular to the axis and centered on it, makes an integer number ℓ of 2π rad turns.

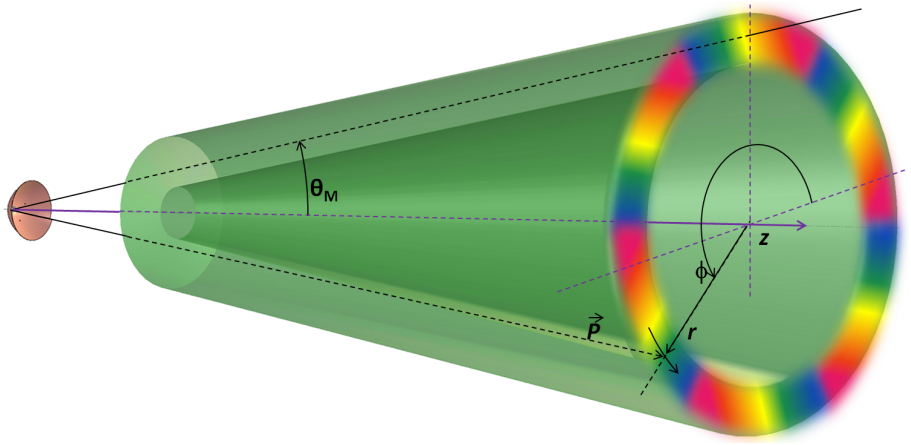

Figure 6.1: Schematic representation of the doughnut-shaped radiation pattern of the power density of a LG beam with $\ell = 6$.

When OAM modes are used in a long range communication systems implemented with antennas of practical diameter, the receiving antenna falls in the doughnut hole, where the available power density decreases like $z^{-2\left(|\ell|+1\right)}$, due to the $\left(\frac{\sqrt{2}\rho}{w(z)}\right)^{|\ell|}$ field term [142], (as can be observed from Eq. 6.2.1); too fast for medium- and long-distance applications. In order to compete with standard radio systems, it is necessary not to waste power. For this reason, an interesting idea

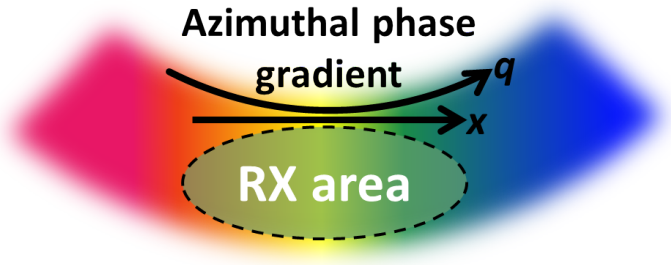

Figure 6.2: Off-axis placement of a general Rx not to waste power. Background colors represent field phase: its azimuthal gradient at the center of the Rx area is horizontal, and can be used as approximation of phase variation over the entire Rx area.

consists in trading orthogonality for power, and place receiver (Rx) close to the doughnut peak (angle θ_M from z axis), where the power density decay follows the classic z^{-2} law, (the so-called Friis formula [19]). To reach this purpose, a planar array of N_r identical elements can be used as Rx antenna,. They must be placed in a region whose center, as seen from the center of transmitter (Tx), is at an angle $\theta \approx \theta_M$ with respect to the z-axis, and whose oblong shape follows the local curvature of the radiation peak (maximum power density), as shown schematically in 6.2. If the link length is large enough, the local curvature is negligible, and one can use a simple linear array, (like in a 1D MIMO setting).

Having disregarded the natural isolation offered by OAM modes, the receiver must implement a different strategy to discriminate different values of ℓ. The field amplitudes experienced by the N_r elements are essentially equal. At this stage, the only variable that can be considered for channel de-multiplexing is the field phase. It can be used a reception approach identical to the one adopted by MIMO systems where the increase in capacity is limited by the mutual correlation of the signals available at the Rx antennas, which in turn depends on the phase gradient of the field. So, to assess the relative merits of this new option, it is necessary to evaluate the ability of OAM systems to “squeeze” more phase information (phase gradient) into a given spatial length, or, conversely, to minimize array length for a given phase difference. Considering the similarities with the behavior of a generic MIMO system, this method inevitably leads to a fair comparison between OAM and MIMO approaches.

6.3 The phase slope parameter

To quantify the ability of a generic transmitting system to induce a phase gradient into a given spatial length, it is useful to introduce a new parameter called *linear phase slope*. It is defined, at an observation point $\vec{P}$, as the derivative of field phase $\Psi(\rho, \phi, z)$ with respect to a curvilinear co-

ordinate of unit metric coefficient, q, defined on a circle centered on the beam axis and orthogonal to it:

$$L(\mathbf{P}) = \frac{\partial \Psi(\rho, \phi, z)}{dq} \tag{6.3.1}$$

The linear phase slope relates to the length of an array required to experience a given phase shift from one end to the other; the relationship between linear phase slope and antenna size will then assess the Rx performance as a space-division de-multiplexer.

When the local curvature of the region occupied by Rx is negligible, then, with a suitable choice of the reference system, q can be replaced by a cartesian coordinate, x; as will be done several times (Fig. 6.2). When dealing with a field whose phase is a function of two spatial coordinates, the concept of phase slope can be generalized, and a *phase gradient* can be defined, (see the next section).

6.3.1 Importance of the phase slope parameter

To stress the importance of the phase slope parameter, it is useful to examine a practical example based on MIMO formalism, (App. C). As a proof of concept, consider a set of N arbitrary channels. Let $L^{(n)}$, $(n = 1, \ldots, N)$, denote the phase slope induced by the n-th channel at a given observation point, along a given direction, x (1 D case). The phase factors observed at a set of M receiving points, $s(m)$, $(m = 1, ..., M)$, aligned along a Rx axis, can be organized as an $M \times N$ channel matrix: $\mathbf{H} = \left\{ e^{i\phi(m,n)} = e^{is(m)L^{(n)}} \right\}$. Whatever the receiving positions $s(m)$, the matrix rows differ from one another only because of $L^{(n)}$. Now, consider a MIMO receiver. In its simple zero-forcing solution, it tries to recover each channel, interference-free, recombining the received signals through $\mathbf{H}^{+}$, the pseudo-inverse [105] of $\mathbf{H}$.

When two channels have the same phase slope, it can be shown by properties of the Singular Value Decomposition of $\mathbf{H}$ [143], that the pseudo-inverse is unable to satisfy $\mathbf{H}^{+}\mathbf{H} = \mathbf{I}$, where $\mathbf{I}$ is the identity matrix. Off-diagonal terms appear, and this entails inability to resolve two (or more) channels.

In case of two phase slopes very close to each other but not exactly equal, the pseudo-inverse matrix formally exhibits $\mathbf{H}^{+}\mathbf{H} = \mathbf{I}$, but noise enhancement arises instead: $\mathbf{H}^{+}$ can be computed via SVD, but the involved channels yield (at least) one singular value λ_i close to zero. The input noise power is thus amplified by a factor $|\lambda_i|^{-2}$, that drastically reduces the available signal-to-noise ratio (SNR).

This reasoning shows that providing significantly different phase slopes is a major target, in the design of a Tx for spatial-multiplexing, regardless of the Rx array conformation.

Clearly, the concept of phase slope has a practical meaning only when applied to iso-frequency channels. The dominant parameter for assessing the discriminability of channels is, in such a case, the difference of phase slopes. Indeed, it is obvious that a common phase slope can always

be factored out from $\mathbf{H}$, leaving a "core" matrix where only differences appear in the phase factors of the various elements. Therefore, a fair parameter in the comparison between systems is, for instance, the overall size of a Tx array, (or of a Tx antenna), required in order to achieve a given difference of phase slopes. In the following, for simplicity, when dealing with arrays, each element will be supposed to be negligibly small with respect to the array size, in order to neglect the elemental radiation pattern.

6.4 Phase slope of a point source

An ideal point source (isotropic radiator) is the basic ingredient for designing a general communication system: its uniform radiation pattern highlights the role of geometrical phase delay as the foremost factor affecting the channel matrix. The simplest way to use it is as element of two paral-

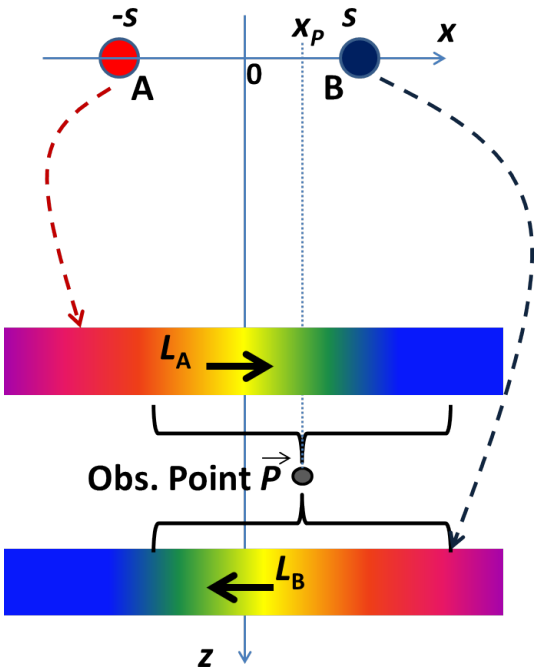

Figure 6.3: Linear phase slopes L_A and L_B at the observation point $\vec{P} = x_P\hat{\mathbf{x}} + z\hat{\mathbf{z}}$ generated by two point sources (A and B), in a standard MIMO configuration with spacing $2s$.

lel one-dimensional linear arrays, Tx and Rx, although the forthcoming reasoning and conclusions can be extended to a 2D placement too. For this reason, it is interesting to calculate the phase slope along the Rx array axis, x, at a distance z from the center of Tx, the z axis being orthogonal to the x one. Let $x = s$ for the transmitting point source, $x = x_P$ for the receiving element under

consideration (the observation point), $x = 0$ at the centers of both arrays, as shown in Fig. 6.3. Clearly, by applying Pythagoras theorem,

$$\Psi(x_P) = -k\sqrt{(s - x_P)^2 + z^2} = -kz\sqrt{1 + \left(\frac{s - x_P}{z}\right)^2} \tag{6.4.1}$$

If Rx is very far from Tx so that $\frac{s-x_P}{z} \ll 1$, (as in long range systems), the following approximation holds:

$$\Psi(x_P) \approx -kz - k\frac{(s - x_P)^2}{2z} \tag{6.4.2}$$

The linear phase slope of Eq. 6.3.1 can be computed neglecting the curvature of the curvilinear coordinate and assuming $q \approx x$; as a consequence, the linear phase slope at midpoint, $x_P = 0$, reads:

$$L_{MIMO} = \left.\frac{\partial \Psi}{dq}\right|_{q=0} = k \left.\frac{(s - x_P)}{z}\right|_{x_P=0} = k\frac{s}{z} \tag{6.4.3}$$

which depends linearly on s. This confirms that in conventional MIMO systems the phase slope at Rx increases if the Tx antenna spacing increases. Hence, to achieve a given total phase shift, a bigger Tx enables a smaller Rx. Incidentally, this remark confirms that the phase slope in conventional MIMO systems is a purely geometrical effect, due to the relative placements of array elements, and irrespective of properties of the individual antennas, as long as their radiation pattern is approximately constant over the whole receiver.

6.5 Phase gradient of a Laguerre-Gauss beam

As mentioned before, the LG beams here examined are characterized by an electric field uniformly polarized, so that it is proportional to the scalar field of Eq. 6.2.1, which satisfies the wave equation in the paraxial approximation. The in-plane components of the phase gradient, in the far field, can be computed in cylindrical coordinates from the argument of Eq. 6.2.1. However, the axial symmetry of the beam can be exploited: it is sufficient to evaluate only the x, y components of the phase gradient on the $-y$ axis (corresponding to $\phi = -\pi/2$ according to Fig. 6.1). It is straightforward to derive, from Eq. 6.2.1, the phase slope for a generic point identified by the θ angle (Fig. 6.4):

$$\left.\frac{\partial \angle LG_{p,\ell}(\vec{P})}{\partial x}\right|_{x=0;y=-z\tan\theta} = \frac{1}{\rho}\left.\frac{\partial \angle LG_{p,\ell}(\vec{P})}{\partial \phi}\right|_{\rho=z\tan\theta} = -\frac{\ell}{z\tan\theta} \tag{6.5.1}$$

$$\left.\frac{\partial \angle LG_{p,\ell}(\vec{P})}{\partial y}\right|_{x=0;y=-z\tan\theta} = -\left.\frac{\partial \angle LG_{p,\ell}(\vec{P})}{\partial \rho}\right|_{\rho=z\tan\theta} = k\tan\theta, \tag{6.5.2}$$

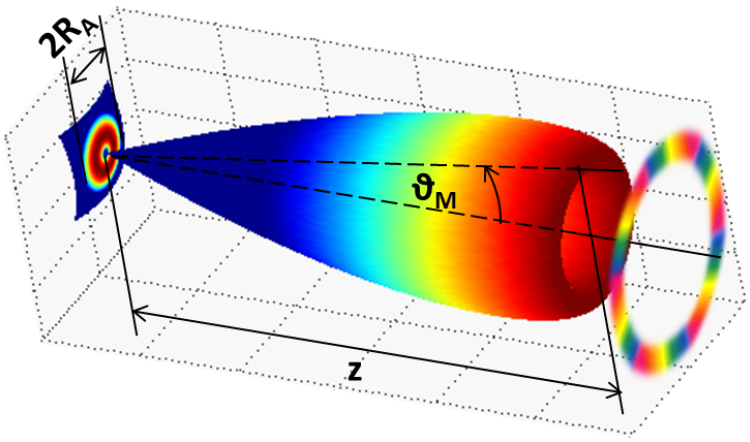

Figure 6.4: Schematic representation of the doughnut-shaped radiation pattern of a single $\ell = 6$ LG beam generated by an antenna of $2R_A$ diameter.

where $\angle$ represents the argument operator and, being in far field, $w(z) \approx \frac{2z}{kw_0}$ when $z_R \ll z$. The value of θ which corresponds to the doughnut maximum, θ_M, is simple to compute for a single-ringed OAM beam (radial index $p = 0$) from Eq. (3) in [142]:

$$\theta_M = \frac{\sqrt{2\,|\ell|}}{kw_0}. \tag{6.5.3}$$

The final expression can then be obtained letting $\theta = \theta_M$ in the previous equations. This step is left for the next subsection, where it fits as a particular case of a wider problem, and will be accompanied by additional comments which apply also to superpositions of LG beams.

6.6 Phase slope of a superposition of concordant and consecutive Laguerre-Gauss beams

The linear momentum radiation pattern of a pure LG beam, sketched in Fig. 6.4, has an intrinsic drawback: in the far field power spreads uniformly over an annular radiation lobe, whose cross section is much wider than any practical receiving antenna. This entails a power budget that can be significantly worse than in ordinary radio links. To mitigate this effect, a coherent superposition of LG beams has been proposed in Chap. 4, which involves $N = |\ell_{max}| - |\ell_{min}| + 1$ consecutive LG modes, from ℓ_{min} to ℓ_{max} all with the same sign. The N modes carry equal powers and have equal beam waists, w_0. This yields a much better confined main radiation lobe, while, at the same time, the field phase variations on a transverse plane are essentially those of the highest-order mode involved in the superposition, ℓ_{max}. An example is shown in Fig. 6.5 and explains why the jargon name for such a beam is “smile”. In Chap. 4, a quantity called azimuthal phase slope, $A_{ps} = \frac{\partial \Psi}{d\phi}$, has been defined, where Ψ is the argument of the (uniformly polarized, hence

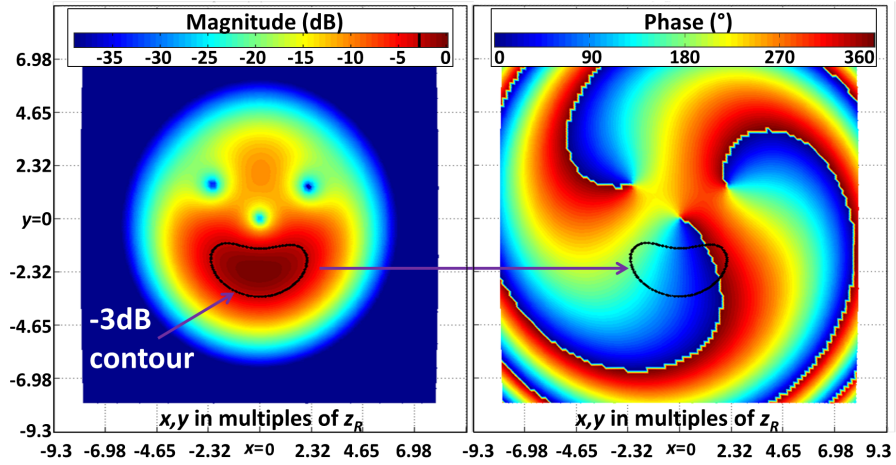

Figure 6.5: Magnitude (left) and phase (right) of a coherent superposition of $\ell = 1$, $\ell = 2$ and $\ell = 3$ LG beams with same beam waist ($w_0 = 11$cm) and equal unitary power. The 3-dB contour (black) is also overlayed on the phase plot as reference.

scalar) electric field, and estimated to be, on average in the main lobe, $A_{ps} \approx \ell_{max}$, which reflects the fact that Ψ would make ℓ_{max} complete (from 0 to 2π) turns while the observation point goes around a circular path, $\phi \in [0; 2\pi]$. To transform this azimuthal phase slope into a linear one, it is necessary to consider the radial coordinate of the observation point - quite likely, placed at the field amplitude peak. An exact expression for the coordinates of the maximum intensity is, unfortunately, not available; it would require the roots of a high-degree polynomial. However, it has been shown in Chap. 4 that the following expression is a good approximation for the radius of a circle close to the peak:

$$s(z) = w(z)\sqrt{\frac{N+1}{2} + |\ell_{min}|} \approx \frac{2z}{kw_0}\sqrt{\frac{N+2|\ell_{min}|+1}{2}} \tag{6.6.1}$$

This yields the following linear phase slope (from 6.3.1), as a function of the beam waist radius shared by all the superimposed modes, w_0:

$$L_{super} = \frac{2\pi A}{2\pi s(z)} \approx \frac{kw_0\ell_{max}}{2z\sqrt{\frac{N+2|\ell_{min}|+1}{2}}} \tag{6.6.2}$$

By Love's equivalence theorem, [19], the total field on the origin $z = 0$ plane can be used as a continuous equivalent distribution of electric sources radiating the same far field for $z > 0$. Assuming that the field source (Tx antenna) has a radius R_A equal to the spot size of the field located at $z = 0$,

$$R_A = s(0) = w_0\sqrt{\frac{N+2|\ell_{min}|+1}{2}}, \tag{6.6.3}$$

then w_0 can be expressed as a function of R_A, and replace into Eq. 6.6.2. The final result is:

$$|L_{super}| \approx \frac{kR_A}{z}\frac{|\ell_{min}|+N-1}{N+2|\ell_{min}|+1} \leq \frac{kR_A}{z} \tag{6.6.4}$$

where the last inequality becomes a good approximation (as an equality) when $|\ell_{min}|$ is much smaller than N. So, the linear phase slope has an upper bound that is proportional to the source size R_A, and independent of the OAM characteristics (ℓ_{min} and N). Notice that this result holds also in the case of a single LG beam, i.e. for $N=1$, $\ell_{min}=\ell_{max}$, with w_0 as the beam waist.

6.7 Phase slope of a generic OAM beam

As introduced in the first chapter, there exist several type of paraxial OAM beams, in addition to LG ones, that can be analytically described. They are all considered in the Circular Beams (CiBs) expression [39, 144], that is the most general solution with OAM of the paraxial wave equation. In fact, by properly setting the CiBs parameters, one can determine the specific analytical expression for a particular beam type as: the standard [145] or elegant [146] Laguerre Gauss beams, Bessel Gauss beams [147], optical vortex beams [51] and others [39].

However, because of the completeness and the bi-orthogonality of LG beams [6] with respect to both ℓ and p parameters, a generic field carrying an OAM quantity equal to ℓ, in a cylindrical reference system, can be represented by a superposition of normalized LG modes as [144]:

$$E_\ell(\rho,\phi,z) = A(\rho,\phi,z)\exp\left(-i\ell\phi\right) = \sum_{p=0}^{\infty} a_p LG_{p,\ell}(\rho,\phi,z) \tag{6.7.1}$$

where a_p are complex amplitude factors and each LG beam is described by Eq. 6.2.1. Moreover, for simplicity but without loss of generality, the a_p coefficients can be assumed to be normalized such that $\sum_{p=0}^{\infty}|a_p|^2=1$.

As for the previous section, it is not possible to determine, analytically, the radial position r_{max} of the field maximum intensity. However, as discussed in Chap. 4, a good estimation of r_{max} can be obtained calculating the field occupancy size $s(z)$ as:

$$s(z) = \int_0^{\infty}\int_0^{2\pi}\rho^2|E_\ell(\rho,\phi,z)|^2\rho d\rho d\phi = \int_0^{\infty}\int_0^{2\pi}\rho^2\left|\sum_{p=0}^{\infty}a_p LG_{p,\ell}(\rho,\phi,z)\right|^2\rho d\rho d\phi \tag{6.7.2}$$

that with some calculations leads to:

$$s(z) = \sqrt{\frac{w^2(z)}{2}\left[1+|\ell|+\Phi-\Re\left(e^{2i\zeta(z)}\beta\right)\right]} \tag{6.7.3}$$

with

$$\Phi = 2\sum_{p=0}^{\infty}p|a_p|^2 \tag{6.7.4}$$

and

$$\beta = 2\sum_{p=0}^{\infty}\sqrt{2p\big(|\ell|+p\big)}a_p a_{p+1}^{*} \tag{6.7.5}$$

Hence, considering Eq. 6.7.3 and the fact that the field phase is characterized only by the $\exp(i\ell\phi)$ term (which describes ℓ turns from 0 to 2π around the beam propagation axis), the phase slope near the field peak can be expressed as:

$$L_{gen} = \frac{2\pi\ell}{2\pi s(z)} = \frac{\sqrt{2}\pi w_0 \ell}{z\lambda\sqrt{1+|\ell|+\Phi+\Re(\beta)}} \tag{6.7.6}$$

However, to complete the phase slope calculation, it is necessary to link the beam waist w_0 with the antenna size R_A. Unfortunately, in this case, $E_\ell(\rho,\phi,z)$ is a completely general field and it can not be assumed that its minimum size s_{min} is equal to $s(0)$, as for the consecutive LG beams superpositions in the previous section. For this reason, first of all, it is necessary to minimize Eq. 6.7.3 with respect to z. After some calculations, it can be found that:

$$R_A = s_{min} = \frac{w_0}{\sqrt{2}}\sqrt{\frac{\big(1+|\ell|+\Phi\big)^2-\big|\beta\big|^2}{1+\big|\ell\big|+\Phi+\Re(\beta)}} \tag{6.7.7}$$

Hence, the phase slope can be expressed as:

$$L_{gen} = \frac{2\pi\ell}{2\pi s(z)} = \frac{kR_A}{z}\frac{\ell}{\sqrt{\big(1+|\ell|+\Phi\big)^2-\big|\beta\big|^2}} \tag{6.7.8}$$

where the square root term can be expressed as:

$$\sqrt{\big(1+|\ell|+\Phi\big)^2-\big|\beta\big|^2} = \sqrt{\Big[\big(1+|\ell|+\Phi\big)+\big|\beta\big|\Big]\Big[\big(1+|\ell|+\Phi\big)-\big|\beta\big|\Big]} \tag{6.7.9}$$

Now, considering that $\beta = 2\sum_{p=0}^{\infty}\sqrt{2p\big(|\ell|+p\big)}a_p a_{p+1}^{*}$, $\sum_{p=0}^{\infty}|a_p|^2 = 1$ and using the triangle inequality [148], it can be proven that

$$\sqrt{\big(1+|\ell|+\Phi\big)^2-\big|\beta\big|^2} \geq 1+|\ell| \tag{6.7.10}$$

For this reason, the final expression of the phase slope is equal to:

$$L_{gen} \leq \frac{kR_A}{z}\frac{\ell}{\big(1+|\ell|\big)} \leq \frac{kR_A}{z} \tag{6.7.11}$$

As can be observed, also in this case the phase slope does not depend by the OAM value carried by the field but only by the transmitting antenna size. Moreover, the same result can be obtained also considering non paraxial beams that are characterized by a greater divergence rate with respect to paraxial ones.

6.8 Comparison

In their simplest form, Eq. 6.4.3, 6.6.4 and 6.7.11 state that, in order to achieve a certain phase slope, the only parameter to be modified is the transmitting antenna size, regardless the field carries OAM or not. More in detail, looking at the examples previously introduced, the MIMO placement in Fig. 6.3 requires a spacing equal to the diameter of a circular OAM antenna, which can be implemented, for example, with a circular array. Circular OAM antennas, however, involve a 2D distribution, whereas the considered MIMO array is 1D. So, comparison seems to be in favor of the latter but, on the other hand, many more OAM channels can be radiated by the 2D structure and the comparison becomes more complicated. General 2D distributions allows for one more direction along which phase gradients can exist, but this is subject to the same constraints and the overall phase-squeezing capability of such an OAM system still equates that of a 2D MIMO setting.

For all these reasons, the capabilities of the two communication approaches (OAM and MIMO) are confirmed to be equal, also using coherent superpositions of LG beams, which had been postulated to be a tool for improving performances of OAM systems thanks to their reduced source size. The same conclusion applies also to higher order OAM modes, as proven in the last section by examining general OAM fields.

These results perfectly agree with a previous investigation performed by Edfors et al. [12] which was restricted to circular arrays. They developed their formal study by considering a 2D MIMO distribution with circular arrays (both in Tx and Rx) and proving that the MIMO eigenmodes coincide with simple superpositions of OAM-carrying modes, i.e. the two approaches are equivalent. The comparison performed in this chapter, on the other hand, investigates general OAM antennas and allows to consider also one-dimensional source distributions. Moreover, it is independent of the antennas configuration.

6.9 Conclusions

To summarize, an OAM-based MIMO radio system is equivalent to a conventional MIMO one, under the viewpoint of channel spatial multiplexing. In fact, the capability of “squeezing” phase information into small space regions, where to place the receivers, is essentially the same for the two approaches and only depends by antennas size. These results, however, are restricted to line of sight reflection free communication systems and well apply to long range point-to-point links.

In conclusion, the choice between OAM and conventional MIMO appears to be essentially a matter of signal processing complexity, when present-day detectors sensitive to power density, i.e. *linear momentum* of the EM field are used. The performances of OAM systems may be improved, in the future, studying for new antennas sensitive only to angular momentum.

Chapter 7

Opposite-sign OAM modes superpositions

This chapter examines opposite-sign OAM modes superpositions and their application to telecommunication systems. Opposite sign superpositions, in fact, are characterized by simpler and more regular field distributions, with respect to single OAM modes, and can simplify both transmission and reception of an OAM-based multiplexing link. To test these characteristics, various outdoor experiments in a real urban environment are performed, together with a theoretical comparison between OAM-based and MIMO-based communication systems.

RELATED PAPERS

Spinello, F., Someda, C. G., Ravanelli, R. A., Mari, E., Parisi, G., Tamburini, F., Romanato, F., Coassini, P. & Oldoni, M. *Radio channel multiplexing with superpositions of opposite-sign OAM modes*. Submitted to AEU-International journal of electronics and communications.

7.1 Introduction

Previous chapters examined how OAM fields can be applied to long range radio communications in order to implement multiplexing systems. The analysis identified the main advantages of this application and also the most critical aspects, like the partial orthogonality exploitation when only a small portion of OAM field is received. Moreover, it has been shown that OAM based systems has the same communication capacity of MIMO ones; the main differences between the two approaches only rely on antennas configuration and on the intrinsic orthogonality of OAM modes that can be exploited directly at physical layer, without digital post processing.

As previously observed, the full reception of single OAM modes over long distances is not a simple task, mainly for two reasons: the large size of fields due to diffraction and the spiral phase distributions. To simplify this last problem, it will be examined, in this chapter, a new approach to OAM modes transmission. It relies on the dramatic simplification of the field phase distribution in space that is obtained if one radiates, instead of one single wave characterized by an integer OAM value, two superimposed waves with equal amplitudes and *opposite* values of their OAMs. The two counter-rotating helices, both propagating through $\hat{z}$ in a cylindrical reference system (ρ, ϕ, z), generate a “standing wave" in the azimuthal direction. Different OAM values can then be discriminated simply by counting the number of peaks (and/or nulls) around a closed path concatenated with the propagation axis z - e.g., a circle lying on a constant-z plane [8].

The theoretical equivalence, in terms of capacity, between this approach and the use of individual OAM modes, has been already discussed both in Chap. 6 and in [12]. Still, it has been considered that this approach was worth an experiment - to the best of today knowledge, unprecedented - since it has some potential advantages. First of all, it releases the receiver from the burden of accurate phase measurements. Second, a further benefit can be exploited if a circular antenna array is used as the radiating element. In fact, in the single-OAM-mode approach, signals feeding the individual antennas must obey strict phase requirements; hence, the bandwidth of the array is limited by that of the phase shifters encompassed in its feeding network. In the “plus and minus ℓ” configuration one phase shift of 180° is enough and, as well known, this can be a geometry-based built-in property of suitable microwave junctions, which can increase significantly the array bandwidth. A third potential benefit may stem from the fact that the field of a standing wave vanishes identically over $|\ell|$ longitudinal planes (i.e., planes passing through the propagation axis). If the antennas are designed so that one of these planes coincides with a discontinuity in the medium, (typically, the ground), propagation may be immune to reflection on this plane.

In the following, it will be reviewed the basic features about the superposition of two OAM modes with equal amplitudes, equal absolute values, but opposite signs of topological charge. Their properties will be outlined using, once again, the Laguerre-Gauss beams. Then, it will be presented the criteria adopted in the design of a series of experiments performed at the unlicensed

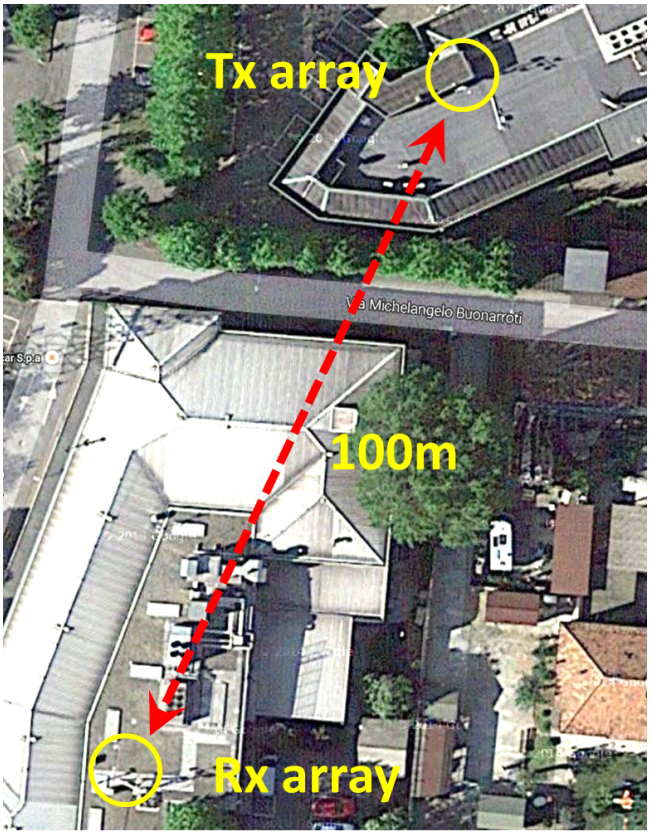

Figure 7.1: Top view of the experimental communication link performed in Cologno Monzese. The link length is about 100m. Note that the experiment has been performed in an urban environment.

frequency of 17.2GHz, on an outdoor link (see Fig. 7.1), about 100m long, on the premises of SIAE Microelettronica S.p.A. in Cologno Monzese, Italy. Finally, the experimental results will be presented together with a comparative analysis with state-of-the-art MIMO systems.

7.2 Opposite sign superpositions properties

As written above, probably the simplest way to describe the basic properties of OAM-carrying EM waves is through Laguerre-Gauss (LG) beams. From previous chapters, it is known that the field of such beams can be described as:

$$E(\rho,\phi,z)_{p,\ell} = \frac{A}{w(z)}\left(\frac{\sqrt{2}\rho}{w(z)}\right)^{|\ell|} L_p^{|\ell|}\left(\frac{2\rho^2}{w(z)}\right) e^{-i\ell\phi} \cdot e^{-\frac{\rho^2}{w^2(z)}} e^{\frac{-ik\rho^2}{2R(z)}} e^{i(2p+|\ell|+1)\xi(z)} \tag{7.2.1}$$

where all the parameters keep the same meaning previously described and the term $\exp(-i\ell\phi)$ characterizes the OAM quantity carried by the field. This latter term is also contained in the mathematical description of other fields, different from LG beams but carrying OAM, as observed in Chap. 6. From now on, for simplicity, only LG beams will be considered but this does not entail any loss of generality.

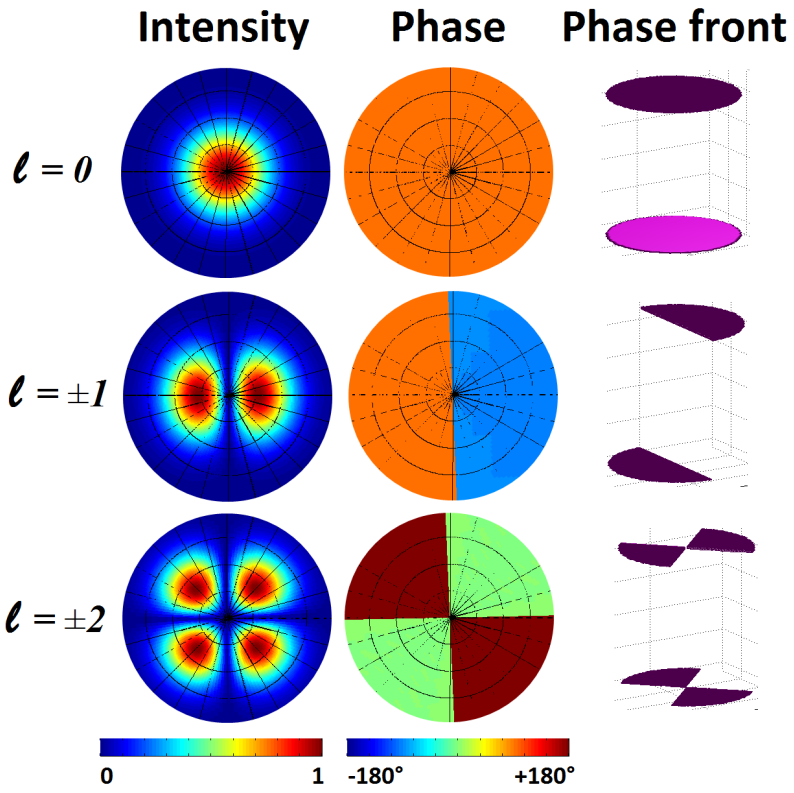

Figure 7.2: Examples of superpositions of opposite-sign OAM modes. First column: intensity distributions of the electric field. Second column: phase distributions. Third column: shape of the phase front. Intensities and phases are evaluated on $z = 0$ plane of the cylindrical reference system previously introduced.

Let's now focus on the superposition (either sum or difference) of two LG beams whose OAM values are equal to $+\ell$ and $-\ell$, respectively, while all their other parameters are equal. Two examples, for different values of ℓ, are shown in Fig. 7.2 where the first column shows intensity distributions of the electric field; the second one shows phase distributions on a plane perpendicular to the propagation axis, and the third one shows sketches of the shape of the phase front. The resulting polarized component of electric field $E_{TOT} = E_{+\ell} \pm E_{-\ell}$ can be expressed, using

Euler's rule, as:

$$E_{TOT}(\rho,\phi,z) = \frac{2A}{w(z)}\left(\frac{\sqrt{2}\rho}{w(z)}\right)^{|\ell|} L_p^{|\ell|}\left(\frac{2\rho^2}{w(z)}\right)\begin{pmatrix}\cos(\ell\phi)\\ i\sin(\ell\phi)\end{pmatrix} \cdot e^{-\frac{\rho^2}{w^2(z)}} e^{\frac{-ik\rho^2}{2R(z)}} e^{i(2p+|\ell|+1)\xi(z)} \tag{7.2.2}$$

This equation shows that, owing to well-known features of the cosine and sine functions, the superposition field has the following properties:

- it consists always of an even number of $2|\ell|$ lobes of equal azimuthal width, separated by $2|\ell|$ field radial nodes;
- within each lobe the field phase is constant, (evaluated on a spherical surface centered in (x,y,z)=0 and with radius equal to $R(z)$);
- the phase difference between adjacent lobes is always equal to $180°$.

These new fields form a complete orthogonal basis for ℓ from 0 to ∞. Like conventional LG modes, their orthogonality can be exploited for channel multiplexing; the difference with respect to [8, 56], or Chap. 3 consists in that each channel is now associated with a combination of two OAM states of equal $|\ell|$. From now on, for simplicity, the field resulting from such superpositions will be referred as the $|\ell|$-th one, specifying, whenever necessary, if it is originated by the cosine or by the sine term.

It is evident that such fields are much simpler, in terms of phase distribution, than the "parent" ones. If suitably exploited, this simplification can be advantageous because phase detection at microwave frequencies is, in general, more demanding than intensity detection. Moreover, special attention must be addressed to the case where sources and detectors are arranged in uniform circular arrays because of their versatility; in this case the advantages of the "plus and minus ℓ combination" are most evident [12]. Indeed, to radiate a field with a uniquely defined OAM, equal to ℓ, the currents feeding the array elements must satisfy two conditions: they must be all equal in intensity and the incremental phase shift between two adjacent elements must equal $\Delta_\phi = 2\pi\ell/N_{ant}$, where N_{ant} is the number of antennas in the array, which must satisfy:

$$N_{ant} \geq 2\ell + 1 \tag{7.2.3}$$

to ensure an acceptable sampling of the generated field [66].

Although the intrinsic benefits of the superpositions are known, it can be useful to recall them briefly:

- for a circular array to radiate a superposition mode, its feeding network does not require any phase shifter. On the contrary, to generate a single $+\ell$ OAM mode, the feed signal for

the n-th antenna requires a factor $e^{-i\ell\phi_n}$ (ϕ_n being the angular position of that antenna), i.e. one phase shifter per antenna. To realize the $(+\ell, -\ell)$ superposition, the only phase shift that is needed is of $180°$: at least in principle, it is enough to reverse the signal polarity. A practical solution can be to insert a $\lambda/2$ - long guiding element (whose price, though, is to limit the tuning bandwidth of the setup) or to use other devices, like couplers or splitters [149]. Clearly, attenuators are needed, since the feed signal for each antenna must be proportional to $\cos(\ell\phi_n)$ or to $\sin(\ell\phi_n)$, but a network without phase shifters is more robust and less expensive;

- one circular array - provided its antennas are numerous enough - can be easily implemented to radiate simultaneously two or more superposition modes, corresponding to two or more values of $|\ell|$. The various feeding signals can be simply summed at the terminals of each array element. Conversely, simultaneous radiation of two or more single $+\ell$ OAM modes requires, for each array element, as many phase shifters as the OAM modes, or, alternatively, two or more concentric circular arrays, one for each mode - a highly unpractical solution;

- the tidy shape of the fields is beneficial at the receiver. In particular, it is simple to identify how to align the receiving antennas. Furthermore, in a full duplex link, due to its symmetry, the feed network which connects the antennas to the radio is identical both at transmitting and receiving side. (If the link is full duplex, each array act as transmitter and need a network composed by attenuators and guiding elements to generate the proper field distributions. On the contrary, if the link is half duplex, only $\lambda/2$ - long guiding element are required in the receiving array network to correctly combine the contributions sampled by the antennas; no attenuators are needed. Finally, only for simple special cases in which the arrays antenna number allows to avoid the use of attenuators, the feeding network of both receiving and transmitting arrays are identical, also in the full duplex configuration).

7.3 Experimental Setup

From now on, for simplicity, only the sums of LG modes and so the cosine functions will be considered, unless the contrary is explicitly stated. Starting from what has been exposed in the previous section, it has been planned a set of experiments whose aim was a preliminary test of this channel multiplexing scheme at microwave frequencies. Therefore, two different double channel half duplex links have been built. The links are based on the following OAM modes configurations: $|\ell| = 1$ (synthesized with two and four antennas) and $\ell = 0$ for the first one and $|\ell| = 2$ and $\ell = 0$ for the second one.

7.3.1 Array design: theoretical background

Propagation of an ideal LG beam is schematically illustrated in Fig. 7.3A, where the field travels from left to right focusing at the $z = 0$ plane. Notice that the transmitting and the receiving set-ups are placed on the opposite sides of the beam waist plane, $z = 0$. The first problem to be considered is how to generate a reasonable approximation of such a field using a single-ring circular array with a finite number of antennas, and how to detect it with another identical array. Also the radius of the arrays was a point of major practical concern. So,

- it has been supposed to use directional antennas, e.g. parabolic ones;
- it has been tried to reproduce the focusing effect that a LG beam exhibits on the l.h. side of its waist plane $z = 0$, by tilting slightly the parabolic antennas of the transmitting array;
- the distance between the transmitting (Tx) and receiving (Rx) arrays D has been set equal to twice the Rayleigh range, z_r[31]. Since z_r represents the region where the beam divergence is minimal, this choice is believed to make the whole system as compact as possible. At the same time, it provides a simple, straightforward rule for the antenna tilts: owing to LG beams properties, the axes of the transmitting parabolas must converge at the center of the receiving array, and vice-versa[150]

The antennas of the Tx and Rx arrays should be placed, radially, where the field intensity reaches its theoretical peak. The field maximum intensity position can be found by calculating the zeros of the derivative of Eq. 7.2.2 with respect to the ρ coordinate. It is simple to derive, with straightforward algebra, the radius of the arrays:

$$r_{arr} = \sqrt{\ell \frac{2D\lambda}{\pi}} \tag{7.3.1}$$

Hence, the optimum array radius depends on the link length and on the chosen OAM value. As the distance between the available sites is about 100m, and the tests were to be performed at the unlicensed frequency of 17.2GHz, the resulting theoretical array radius for the $|\ell| = 1$ experiment is $r_{|\ell|=1} = 0.52$m, while for the $|\ell| = 2$ it is $r_{|\ell|=2} = 0.73$m. The trade-offs imposed by practical constraints will be pointed out in the following. Clearly, the channel multiplexing experiments become more meaningful if the conventional $\ell = 0$ mode is transmitted over the same path, at the same time. To do this, it has been decided to use a pair of dedicated parabolic antennas, placed at the centers of the two arrays. Alternatively, one could use the arrays themselves, with all their elements fed in phase. The power budget for the $\ell = 0$ mode link will be lower, (theoretically, by 12dB if only one dedicated element is used). Nonetheless, since there were no power-limits in this experiment, the first approach was preferred because it greatly simplifies the feeding networks, and avoids signal pre- or post-processing for the $\ell = 0$ mode.

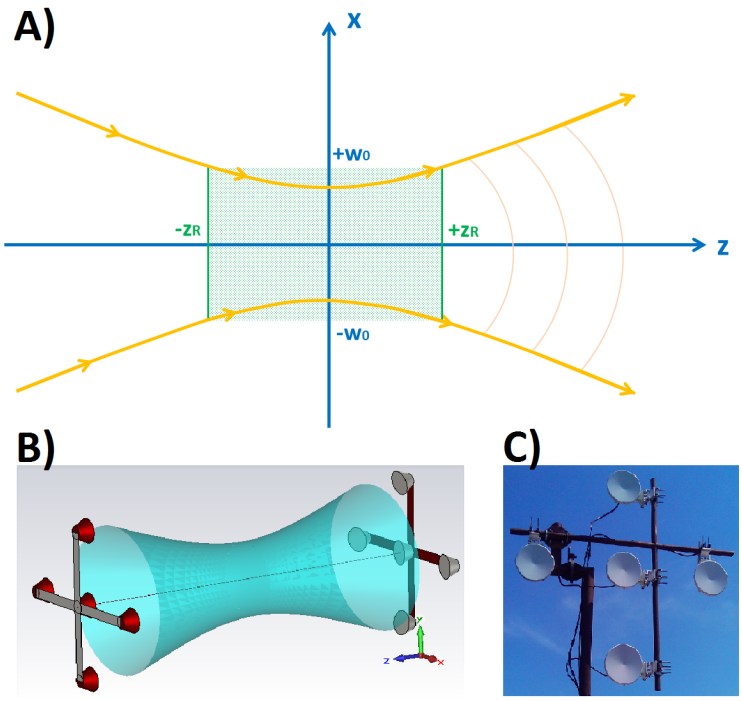

Figure 7.3: A) propagation of a Laguerre-Gauss beam; the green area represents the Rayleigh range. B) scheme of the communication link and sketch of the desired field distribution. C) photograph of the actual array.

7.3.2 Experiment design: practical trade-offs

Following the criteria described above, two identical arrays consisting each of 4 parabolic antennas (diameter equal to 360mm) have been built and mounted on a cross-shaped steel structure (see part (C) of Fig. 7.3). The array radius (length of the cross arm) was 0.95m, significantly different from the ones calculated in the previous sub-section. In fact, technical and infrastructural constraints in the horizontal arm of the cross did not allow to implement the optimum values. Similarly, it has been necessary to use the same array radius for both experiments. Consequently, the following results can be looked at as a test of robustness to system impairments.

The signal feeding networks, schematically shown in in Fig. 7.4, consist of passive elements, namely, flexible waveguides, 2-way splitters, and attenuators. Special attention was paid to the length of the feeding waveguides. Branch length differences larger than λ were carefully avoided, to prevent digital modulation inter-symbol interference. The maximum allowed branch length difference was of $\lambda/2$, required for signal phase inversion. As signal source, for each channel, commercially available outdoor transmitting/receiving radio units manufactured by SIAE Microelettronica, (ALFOplus series [118]), have been employed. They are completely settable in all parameters

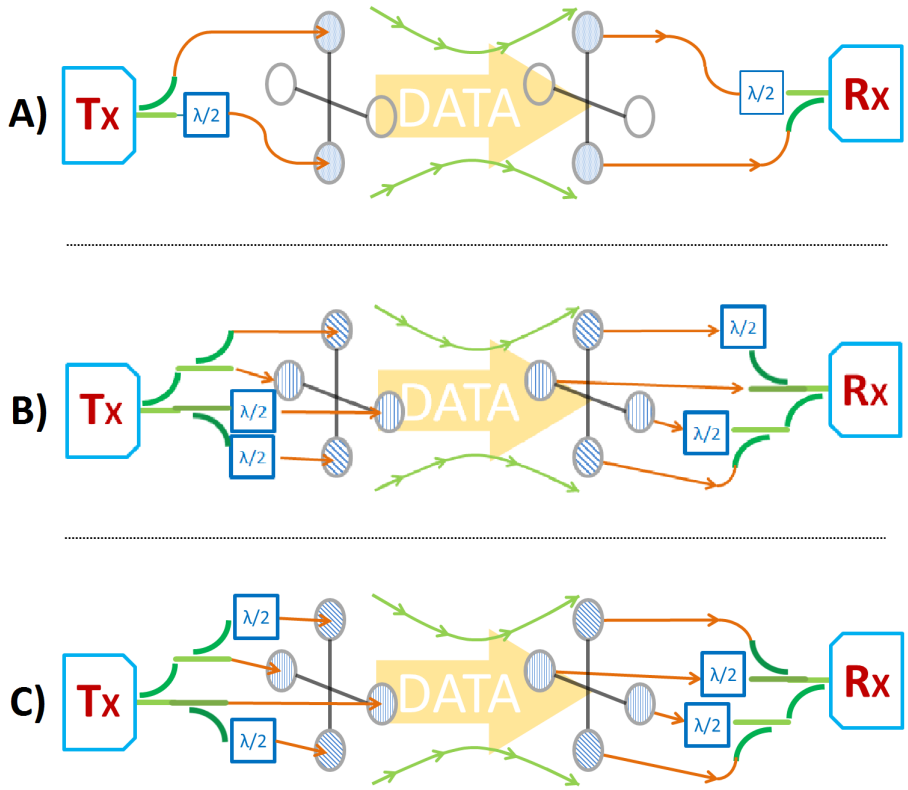

Figure 7.4: Connection schemes: A) transmitting and receiving $|\ell| = 1$ with two antennas; B) transmitting and receiving $|\ell| = 1$ with four antennas, C) transmitting and receiving $|\ell| = 2$ with four antennas. In all schemes, for simplicity, the central antenna dedicated to the $\ell = 0$ mode is omitted. Red lines represent waveguides connections while the green elements are the two-way splitter/combiner.

of interest (transmitted power, QAM constellation scheme, carrier frequency, channel bandwidth, etc.).

Notice that, while the sampling rule of Eq. 7.2.3 seems to indicate that generating the $|\ell| = 2$ state would require at least 5 antennas, the experimental array consists of only 4. This apparent paradox is easy to resolve: the fifth antenna would be essential to discriminate the $\ell = +2$ from the $\ell = -2$ mode, but for their superposition 4 antennas are enough. In fact, it is not possible to distinguish the $\exp(i2\phi)$ function from the $\exp(-i2\phi)$ one when only four sampling points are used. On the contrary, 4 points are enough to reproduce the behavior of the $\cos(2\phi)$ function. Similarly, also 2 antennas are enough to generate the $|\ell| = 1$ field. This statement is confirmed by the data reported below.

7.3.3 Experiment simulations

The previous sub-sections pointed out why there are discrepancies between the theoretical optimum design of the experimental set-up, and its practical layout. Consequently, numerical simulations of the field distributions radiated by the actual arrays are highly recommended as benchmarks for the experimental data. All the simulations of $|\ell| = 1$ (with two and four antennas) and $|\ell| = 2$ modes were made with the Method of Moments (MoM). Field intensities and phases were calculated on four planar surfaces of suitable size, orthogonal to the direction of propagation and located, respectively, at 25, 50, 75 and 100m from the transmitting array. The fields at the receiver distance (100m) are to be compared with predictions based on LG beam analytical theories.

The results shown in Fig. 7.5 confirm the basic expectations previously exposed, i.e. the proper number of lobes, separated by nulls and with phase differences of $180°$. Still, the agreement with LG beam theory is only qualitative, as shown, for example, by the presence of secondary lobes, which appear to be due to the fact that these arrays sample LG beams in a too gross way. Simulations indicate also that the size and the precise location of the main lobes at the receiver do not coincide with LG-based theoretical expectations. There are at least two non-mutually-exclusive explanations for these discrepancies. The first is the already mentioned different size of the array, with respect to the optimum one. The second one can be identified analyzing the simulated field plots at intermediate distances, along the link. They do not exhibit any indication of the focusing at mid path shown in Fig. 7.3A. This discrepancy has been interpreted as an indication that the parabolic antennas composing the array are not numerous enough to emulate a wavefront of a LG beam. Finally, notice that for $|\ell| = 1$, if one sticks - as made in these simulations - to the design criteria described in the previous section, then the receiving antennas turn out to be, roughly, on the top of a secondary lobe, not on the main one. This is expected to entail a slight deterioration of the power budget. Nonetheless, it has been decided to proceed with the experiment, given that its main purpose, (to demonstrate OAM-based space-division multiplexing), was compatible with this deteriorated power budget.

7.4 Results

Before starting the communication tests, the received electric fields have been mapped, to compare them with simulations. Each intensity was sampled along a vertical line passing through the center of the receiving array. A typical example of these measurements, (intensity distribution of the $|\ell| = 1$ field generated with two vertical antennas, as in Fig. 7.4A), is shown in Fig. 7.6. Comparing this with the simulation data extracted from Fig. 7.5A, a very good matching can be observed.

After repeating this operation with the other transmission modes, and checking that the align-

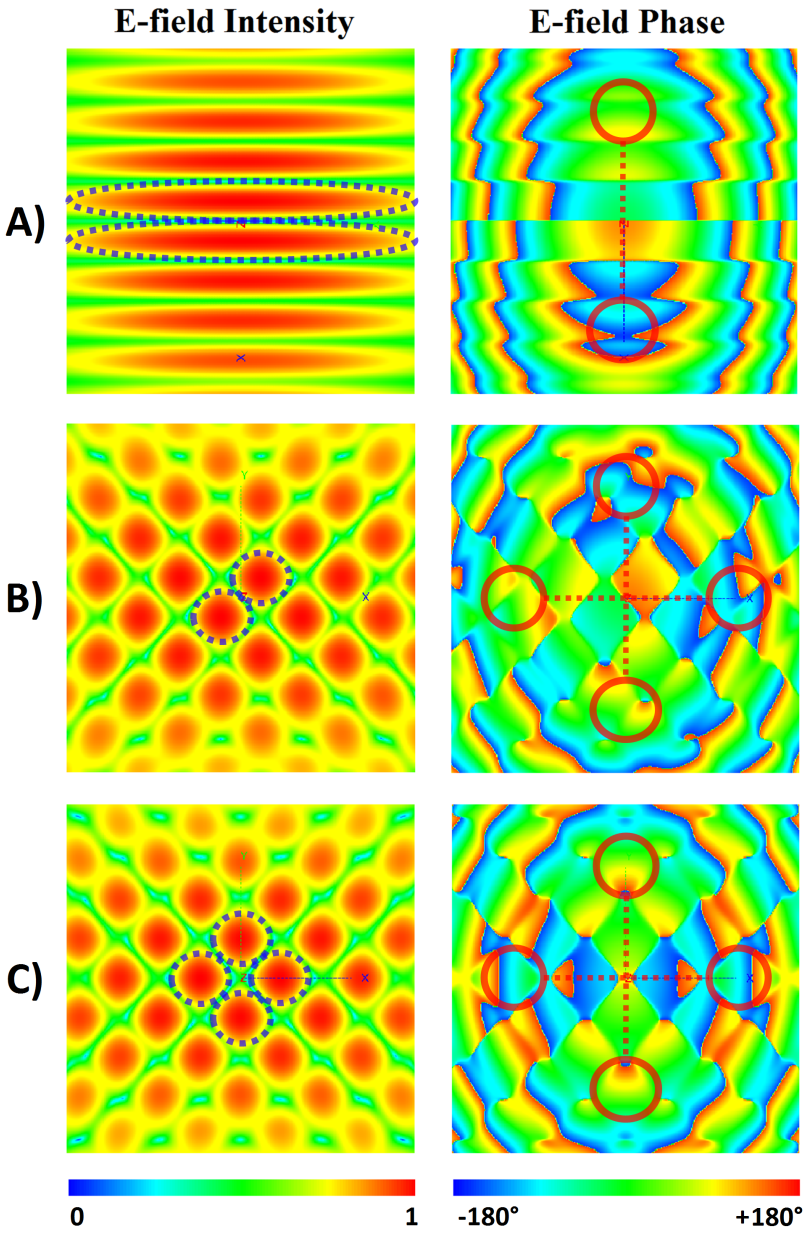

Figure 7.5: Electric field distributions of various OAM modes superpositions calculated on a 4m x 4m planar surface centered on the receiving array position, 100m from the transmitting array. A) field of $|\ell| = 1$ synthesized with two antennas; B) field of $|\ell| = 1$ synthesized with four antennas; C) field of $|\ell| = 2$ synthesized with four antennas. The main lobes of each field magnitude distribution, depicted in the left column, are encircled with dashed lines. On the contrary, the array configurations used in the simulations are depicted in transparency over the phase distributions of the right column.

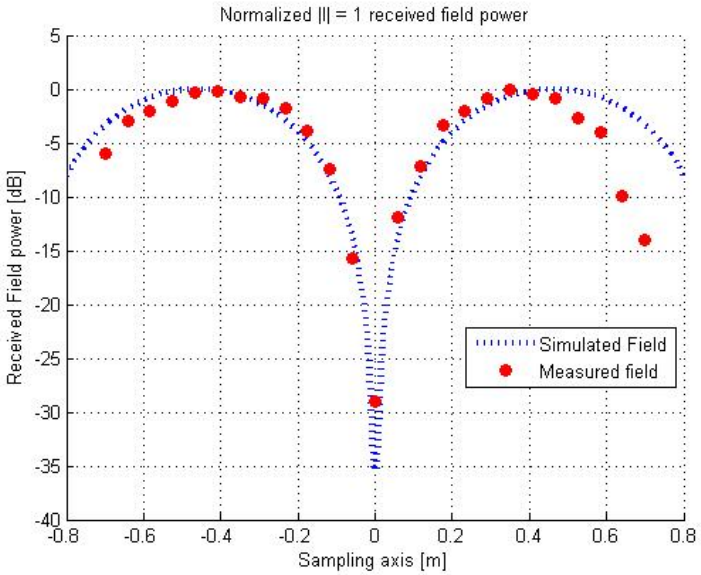

Figure 7.6: Simulated (blue dashed line) and measured (red dots) $|\ell| = 1$ field along a vertical line at the center of the receiving array. The $|\ell| = 1$ mode is generated with two antennas.

ment of the receiving array is correct, the transmission tests over the three link configurations described in the previous sections started according to the following procedure:

1. implement the feeding networks of the arrays according to the desired value of $|\ell|$;
2. set the configurable radio units to transmit their simplest modulation format (4-QAM) and minimum bandwidth ($B = 4$MHz), this configuration clearly being the most robust;
3. set the transmitted powers as to equalize the received powers for the two simultaneously transmitted modes. This operation is essential, given that the two modes are radiated by a different number of antennas and, furthermore, the radii of the Tx and Rx arrays (see the previous sections) do not correspond to the points of field maximum intensity, given by Eq. 7.3.1;
4. check the equality between the measured and the calculated link budgets;
5. check, with a Vector Network Analyzer (VNA), that the outputs at the terminals of all receiving antennas have the expected intensities and phases. More precisely, check the $180°$. phase shifts, and equal intensities;
6. record the Signal to Noise and Interference Ratio (SNIR) of each channel and the relative modulation scheme;

7. go back to 2), and repeat all the previous points, increasing gradually the complexity of the modulation scheme and the signal bandwidth. The constellation schemes are: 4 - 16 - 32 - 64 - 128 - 256 - 512 - 1024-QAM; the available bandwidths are 7 - 14 - 28 - 56 MHz.

Typical examples of the collected data are shown in Figs. 7.7 and 7.8. Fig. 7.7 reports an

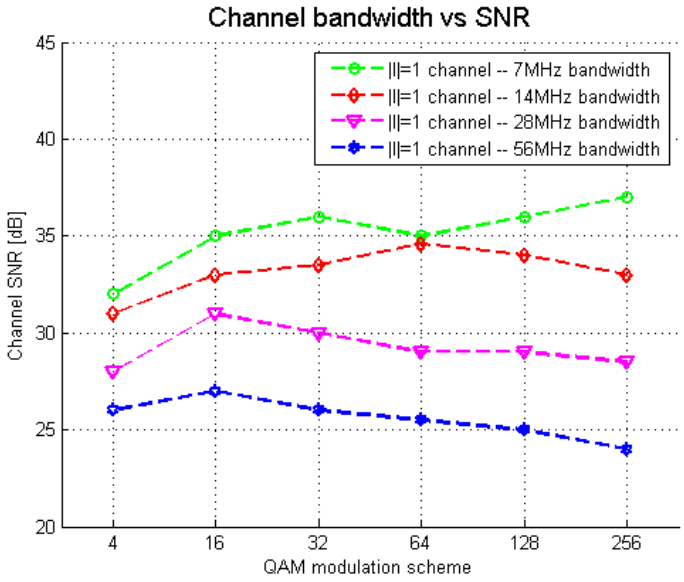

Figure 7.7: SNIR of the $|\ell| = 1$ channel for a transmitted signal with bandwidth from 7 to 56 MHz.

example of the SNIR behavior for the double link based on the $|\ell| = 1$ (with 2 antennas) and $\ell = 0$ OAM modes. In particular, it depicts the SNIR variation of the $|\ell| = 1$ channel for a transmitted signal with four different bandwidth. The values are between 24 and 36 dB, and the maximum reached modulation scheme is 256-QAM. As can be observed, the SNIR values decreases as the signal bandwidth increase. Notice that these results refer to the first test, in which the antenna feed signal intensities and phases were carefully controlled; conversely, a careful equalization of the feeding waveguide lengths was overlooked. The residual length unbalance was responsible for inter-symbol interference at the receiving side, which deteriorated the reception quality, and limited the reachable SNIR level. After equalizing more carefully the waveguide lengths, it was possible to push the modulation schemes to their highest values. An example is reported in Fig. 7.8, which shows the SNIR behavior for the double link made with the $|\ell| = 2$ and $\ell = 0$ OAM modes. It shows an increase in SNIR up to about 35dB; moreover, the maximum modulation scheme, achieved with error-free performance, improved up to 1024-QAM. The same behavior was found for the SNIR in a double link based on the OAM modes $\ell = 0$ and $|\ell| = 1$ synthesized with four antennas.

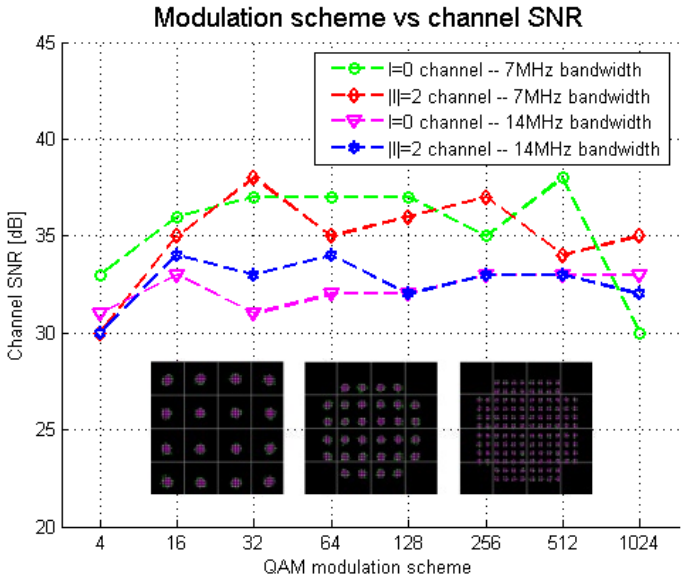

Figure 7.8: SNIR of the half-duplex double-channel link based on the $|\ell| = 2$ and $\ell = 0$ OAM modes. Transmitted signal bandwidth: 7 and 14 MHz. Inset: examples of constellation schemes; from left to right: 16-QAM, 32-QAM and 64-QAM.

7.5 Comparison with theoretical models

A theoretical analysis of ideal performances of the setups previously described will now be presented. All the setups are assumed to keep the same Tx and Rx antenna configuration, over the same distance. The mathematical model, used to make the performances evaluation, has been derived using the classical MIMO formalism based on linear algebra and on the ray tracing characterization of the communication channel. The approach is the same adopted in [12]: different link configurations are compared with the same Single Input Single Output (SISO) link, used as reference. In this way it is possible to find the configuration that gives the best performances with respect to the same reference. The comparison can be based on various metrics parameters, for example: the overall system capacity, the Signal to Noise and Interference Ratio (SNIR) of each channel, the power gain of each channel, etc. In particular, in [12] the comparison parameter is the system capacity; on the contrary, here it will be considered the SNIR. Let's now switch to the results obtained from the comparative study; more details and a full description of the mathematical model can be found in App. C.

The results report the SNIR variation Δ_{SNIR} of each channel with respect to a common SISO link characterized by a Signal to Noise Ratio of 30dB. Firstly, it has been examined the OAM-based system, where each data stream is associated with an OAM mode. In particular, as in the experiments, the $\ell = 0$ mode was associated to a single antenna and not to the whole array.

Next, the evaluation has been repeated for a conventional MIMO system with the same channels number and antenna configuration. In this case, the mathematical model has been configured to implement a Channel State Information (CSI) MIMO, both at the transmitter and at the receiver [105]. This choice means that the benchmark for the OAM-based system is the *best performing* MIMO system, perfectly adapted to the antennas configuration. From theory, it is well known that a similar MIMO scheme can support more channels, theoretically, as many as the antennas. But, in spite of this, the examined MIMO configurations have been restricted to the same channel number as the OAM ones, given that comparison between the systems is based on channels SNIR and not on the overall capacity. The calculation results are reported in Table 7.1.

Table 7.1: Δ_{SNIR} of the OAM based links and of the MIMO based ones.

Array radius	**Link channel**	**Antennas per channel**	$\boldsymbol{\Delta}_{\text{SNIR}}$
r = 0.52m	$\lvert\ell\rvert = 1$	2	4.3dB
	$\ell = 0$	1	0dB
r = 0.52m	$\lvert\ell\rvert = 1$	4	4.3dB
	$\ell = 0$	1	0dB
r = 0.52m	MIMO-ch1	3	7.8dB
	MIMO-ch2	3	4.3dB
r = 0.73m	$\lvert\ell\rvert = 2$	4	8.5dB
	$\ell = 0$	1	0dB
r = 0.73m	MIMO-ch1	5	10dB
	MIMO-ch2	5	8.5dB

First of all, considering only the OAM links, it is clear that the Δ_{SNIR} of the $\ell = 0$ channels is always equal to zero. This confirms the fairness of the adopted mathematical model, since each $\ell = 0$ channels is identical to the reference one. Moreover, the Δ_{SNIR} for the $|\ell| = 1$ channels does not depend on the number of antennas involved in the mode generation, (the equivalence between 2- and 4-element $|\ell| = 1$ arrangement can also be mathematically proven for an arbitrary common radius r). Second, observe that the Δ_{SNIR} values for the $|\ell| = 1$ and $|\ell| = 2$ channels are quite different. This is caused by the fact that the ideal array sizes are calculated with an ideal model of electromagnetic propagation. Remember that, as illustrated by numerical simulations (Fig. 7.5) and measurements (Fig. 7.6), the receiving fields are quite different from ideal assumptions, so the receiving antennas are not placed exactly on the fields maximum leading to a degradation of the link budgets.

In the end, it is straightforward to notice that the theoretical Δ_{SNIR} values for the OAM-based systems and for the MIMO ones are comparable. However, the MIMO systems exhibit slightly better values because of two factors. First, the inner structure of a CSI MIMO can fully adapt

to better exploit the link infrastructure. Second, each MIMO channel exploits all the antennas of the array, while the $\ell = 0$ mode does not. However, the price paid by a CSI MIMO is a more complicated feed network structure, when compared to the OAM approach implemented in a given technology (hardware or, more typically, software).

7.6 Conclusions

The main task of the work reported in this chapter was to test, experimentally, whether suitable superpositions of opposite-sign orbital angular momentum modes can yield any advantage, compared to single valued OAM modes, for space division multiplexing in medium range radio communications. The basic aim was to simplify the system, in particular for what concerns phase detection. To this purpose, an experimental link has been designed and tested, performing also numerical simulations. Finally, for the sake of completeness, the performances of the examined system have been compared with those of a conventional MIMO one by means of a theoretical analysis. Considering all the data that have been collected and the results obtained from experiments it is possible to make the following considerations. First, the experimental results confirm that OAM-carrying EM waves can indeed be used to achieve radio channel spatial multiplexing, over medium-range distances (about 100m) in a typical urban environment. The comparison with MIMO configurations shows that the communication performances, in terms of SNIR, are very similar to those of the best possible MIMO systems, essentially reconfirming a prediction of [12] exposed in Chap. 1. In fact, the theoretical SNIR in the MIMO configuration is slightly better, but only when the system is optimized with respect to the link dimensions and if losses in the antenna feed networks are neglected. A complex network is expected to have more losses with respect to a simple one.

In summary, the experiments demonstrate that suitably combined OAM-carrying waves can be a valid tool for implementing a communication system with performances comparable with state-of-the-art solutions. In particular, the combinations tested in this work may yield other advantages, which encourage further works. The simple structure of the transmitting and receiving arrays, the simple and highly symmetrical distributions of the generated EM fields, the presence in them of nulls that can be exploited to prevent harmful reflections, and the physical mutual orthogonality of the different OAM modes, are attractive hints, as they might help reducing the complexity of the antenna array networks and the load of numerical post-processing, which characterize conventional MIMO systems.

Chapter 8

Short range OAM-based communications

This chapter examines the application of OAM waves to short range multiplexing systems by studying a radio link composed by circular arrays of patch antennas. The link is analyzed both theoretically and experimentally, in order to determine its communication performances with respect to antennas alignment. Moreover, a new application of OAM modes is considered: the enhancement of the communication security level directly at the physical layer.

RELATED PAPERS

Spinello, F., Mari, E., Oldoni, M., Ravanelli, R. A., Someda, C. G., Tamburini, F., Romanato, F. & Parisi, G. (2015). *Experimental near field OAM-based communication with circular patch array*. Submitted to IEEE Transactions on Antennas and Propagation.

8.1 Introduction

OAM waves are particularly interesting for communication systems because of their natural orthogonality. They can be used to implement multiplexing systems where different information channels, on the same frequency, are distinguished directly at the physical layer, without any digital post processing. However, as exposed in previous chapters, it is clear that the use of such waves in long range links is quite complicated: there are several problems in orthogonality exploitation when dealing with large field distributions. Moreover, the performances of OAM-based systems and MIMO-based ones have the same upper limit which only depends by the transmitting antennas size. Therefore, the use of OAM waves in long range links appears to be not so advantageous with respect to other techniques just implemented in today commercial systems.

On the other hand, OAM waves may be a powerful resource for short range communication systems (characterized by a distance lower than the Fraunhofer one [151]), where the received fields present smaller dimensions and can be completely received with practical antennas. Here, OAM modes can be used to implement multi-channel high-rate data links with low complexity processing that can be adopted, for example, in wireless communications within data centers or within server farms. The study of such applications, however, is fairly recent. Some authors started with theoretical analysis, looking in particular at the system performances and limitations [81, 152]; other authors performed communication experiments exploiting optical techniques at millimeter wavelengths [8].

In this context, this chapter analyzes a short-range OAM based communication system implemented by means of circular arrays composed by patch antennas. Circular arrays have already been considered in literature but only as OAM generators [2, 71]; this is the first experimental test in which patch arrays are used bilaterally for OAM-based communication purposes. In the end, the chapter also examines a new application of OAM waves that allows to enhance the communication security level directly on the physical layer.

8.2 Circular arrays background

As explained in Chap. 1, OAM waves can be generated and detected by several devices [73, 117, 153, 154]. However, among all, circular antenna arrays are particularly interesting because of their versatility.

To generate an OAM mode with topological charge equal to $\pm\ell$, the antennas are fed with the same signal amplitude, but with phase delays such that the phase is incremented by $\pm 2\pi\ell$ over a complete turn (i.e., 2π radians). In other words, there is a phase shift between neighboring antennas of $2\pi|\ell|/N_{ant}$ rad, where N_{ant} is the number of (equally spaced) antennas in the circular array, either clockwise (-ℓ) or counter-clockwise ($+\ell$). Moreover, that generation of an OAM mode

of order $|\ell|$ requires a proper number of antennas, $N_{ant} \geq 2|\ell| + 1$ [66], otherwise the beam phase distribution would be under-sampled, according to Nyquist theorem. Also, using circular arrays it is possible to control the angular direction of the main radiation lobe, and the secondary lobes distribution, acting on the array radius [67].

Circular arrays composed by elementary dipoles [66], patches [68, 72], and Vivaldi antennas [70], have been simulated before, for OAM generation. A patch array prototype has also been designed, at the frequency of 2.5GHz [69], but according to the literature, it was not tested in a communication system.

8.3 Experimental setup design

In the experimental setup, two circular arrays are used for generating and receiving OAM modes. Each array is composed by 9 patch antennas. One patch, placed at the center, generates or receives the $\ell = 0$ mode, whereas eight patches, equally spaced around a circle, are designed for the $\ell = \pm 1$ modes. An overview of the system is shown in Fig. 8.1. Each patch is fed through a coaxial cable, linked with a SMA connector. The cable lengths introduce the proper phase delays of the feeding signal, to generate the desired OAM mode. The cables are connected to

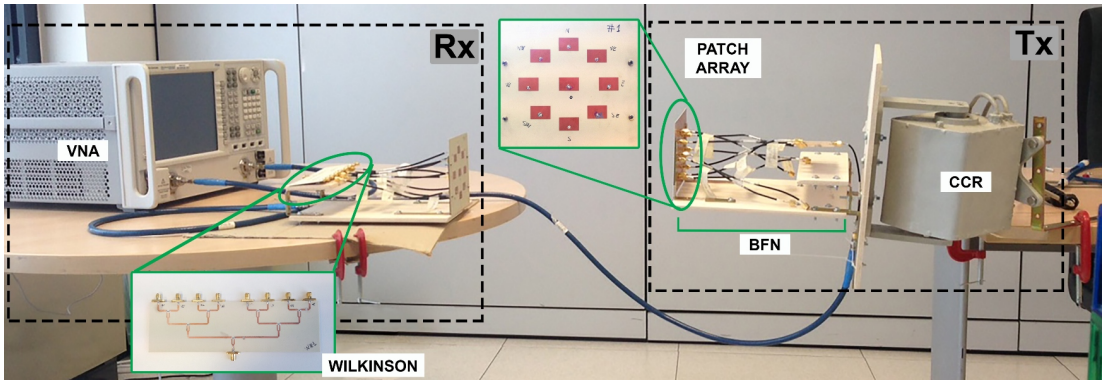

Figure 8.1: Overview of the experimental setup. From left to right: Vector Network Analyzer (VNA), receiving array and transmitting array with their Beam Forming Networks (BFN). Transmitting array is mounted on the Computer Controlled Rotator (CCR). Left and right insets: Wilkinson power divider and the array structure, respectively.

the outputs of a Wilkinson power divider, which splits evenly the input signal. The set of cables and the Wilkinson power divider form the so-called beam forming network (BFN). To generate the $\ell = \pm 1$ modes, the coaxial cables connected to the patches of the circular array are tailored to introduce a relative phase delay of 45° between consecutive antennas.

The entire array was designed and optimized, by means of a FEM code, to operate at fre-

quency a of 5.75 GHz. The patches are 19.58mm wide and 13.07mm high. Patches are realized

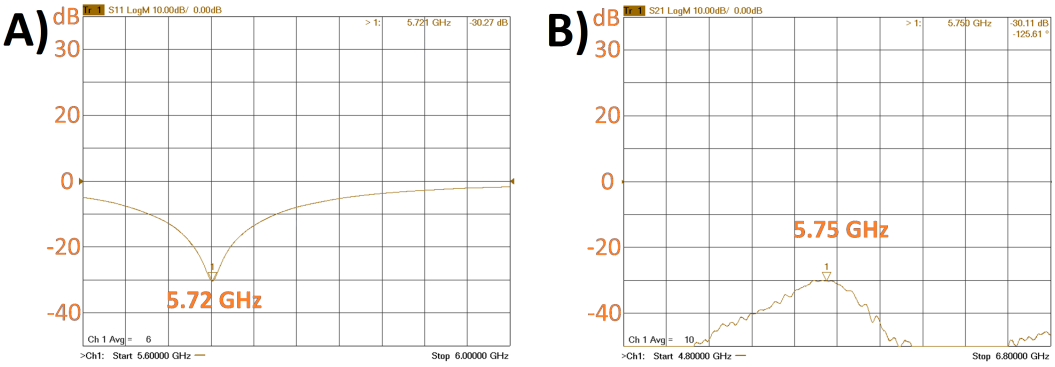

Figure 8.2: A) example of S_{11} measurement of a single patch. At the resonance frequency of 5.72GHz $S_{11} = -30.3$dB. B) example of mutual-coupling measurement (S_{12}) between the central patch of the array and the one on its left. At the working frequency of 5.72GHz $S_{12} = -30.1$dB.

on a ceramic copper substrate (Isola IS680-345) with a thickness of 0.75mm and dielectric constant $\epsilon = 3.45$. The connector pin feed is centered on the non-resonant side of the patch, at 3.57mm from the lower edge. The patches have been characterized by using a Vector Network Analyzer (VNA) Agilent PNA-N5222A, measuring the proper S-parameters. S_{11} measurements allowed to observe that the patch resonant frequency is at 5.75 GHz $\pm$ 30 MHz. Moreover, the S_{11} values at the working frequency are all below -15dB, thus proving a good match of the $50\ \Omega$ line impedance. A measurement example is reported in Fig. 8.2A.

As briefly reported, eight patches, dedicated to the generation of the $\ell = \pm 1$ OAM modes, are equally angularly placed along a circumference with a radius of 40mm. With this choice, the patch mutual-coupling value (S_{ij} where $i \neq j$ are patch indexes) is predicted to be lower than -20dB. Measurements confirmed that the designed array satisfies this constraint, as required. An example is reported in Fig. 8.2B where a mutual-coupling diagram is shown.

A detailed list of the cables parameters are reported in Table 8.1. First column labels the i-th cable, $i = 1, ..., 8$. Second and third columns contain modulus and phase of the S_{21} parameter, respectively, describing the input-output relation of each cable. The fourth column reports the phase delay difference between two consecutive - i-th and $(i+1)$-th - cables. Phase differences are equal to $45° \pm 1°$. This result is, indeed, suitable for the generation of $\ell = \pm 1$ OAM modes.

As already mentioned, the second component of the BFN is the Wilkinson unit, composed of an 8-lines power splitter (see inset of Fig. 8.1). In the BFN at the transmission (Tx) side, the i-th cable is connected with the i-th divider output line. The same is done to realize the BFN at the reception (Rx) side. As a first step, the Wilkinson unit was designed and optimized by means of FEM simulations at the same working frequency, 5.75 GHz. Then, the structure was built on the

Table 8.1: A cable set characterization.

Cable ID	$\|S_{21}\|$[dB]	$\angle S_{21}[^\circ]$	$\Delta\angle S_{21}[^\circ]$
1	0.41	117	44
2	0.43	161	46
3	0.43	-153	45
4	0.40	-108	45
5	0.42	-63	44
6	0.43	-19	46
7	0.41	27	45
8	0.41	72	45

same laminate used to build the patches. To realize a characteristic impedance of 50 Ω, the input-output lines of the divider are 1.7mm wide; the connectors used are SMA. Again, using the VNA the S-parameters have been measured. The resulting amplitude of the reflection coefficient at the input port of the Wilkinson dividers, S_{99}, is lower than -18dB for a 100MHz bandwidth around the working frequency. Table 8.2 reports the measured S_{i9} parameters, with $i = 1, ..., 8$ labeling the i-th divider output line. Second and third columns of the table refer to the Tx divider, fourth and fifth columns to the Rx one. The results show that the Wilkinson systems divide (recombine)

Table 8.2: Characterization of two Wilkinson power divider.

OUT	$\|S_{i9}\|$[dB]	$\angle S_{i9}[^\circ]$	$\|S_{i9}\|$[dB]	$\angle S_{i9}[^\circ]$
1	-11.4	140	-11.0	141
2	-11.6	141	-11.1	140
3	-11.8	140	-11.4	139
4	-11.5	142	-11.2	141
5	-11.4	143	-10.9	140
6	-11.3	144	-10.9	141
7	-11.0	144	-11.0	139
8	-11.0	143	-11.2	138

evenly the transmitted (received) signal, both in amplitude and phase, with tolerances of ± 0.4dB and $\pm 3^\circ$, respectively.

8.4 Experimental results

The patch arrays just described have been employed to perform several experiments. First of all, the generation of $\ell = \pm 1$ OAM fields has been tested and then a communication link at short range, 0.15m, has been implemented. The distance of 0.15m has been chosen in order to have a practical setup, easily to be managed in laboratory. However, by properly rescaling the size of antennas, it is possible to design short range OAM-based communication systems on higher

distances. For example, with antennas of 1m diameter it is possible to reach distances up to 50m.

8.4.1 Field maps

The first experiments consisted in generating the $\ell = 1$ and $\ell = -1$ modes by means of the patch arrays described in the previous section. One array at a time was mounted as transmitter on a computer controlled rotator (PRO.SIS.TEL. PST-CS9), moving along a spherical surface both in elevation and azimuth with a resolution of $0.2°$. On the receiving side, a single patch antenna was placed at 0.15m distance, to probe the generated field. In fact, after 0.15m the generated OAM doughnut intensities have the same diameter of the designed circular arrays (80mm) and so this is an optimal distance for the communication tests to be performed. The input of the BFN at the Tx side was connected to the first port of the VNA, set to measure the S_{21} parameter at the frequency of 5.75GHz, and the probing patch to the second port. The VNA was set to transmit

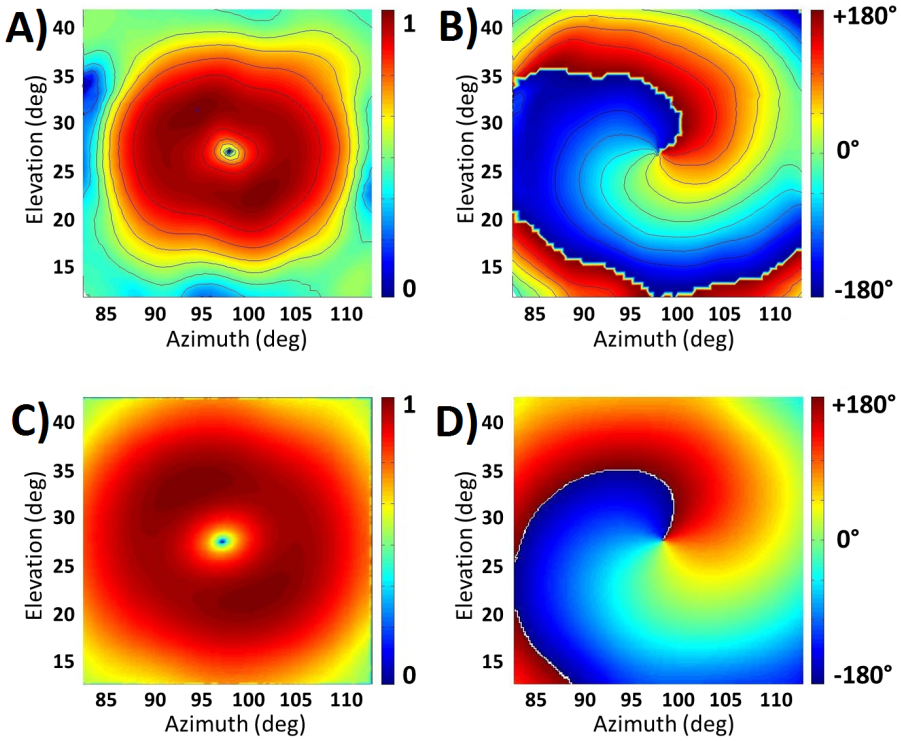

Figure 8.3: Electric field generated by a 8 patches circular array configured to produce a $\ell = +1$ OAM beam. A) measurement and C) simulation of the normalized intensity distribution. B) measurement and D) simulation of the phase distribution.

a dummy signal at 0dBm power. All the measurements were performed in a typical laboratory environment, and the sampled data were collected into 2D maps. The experimental results were then compared with numerical FEM based simulations. Two examples of simulated and measured

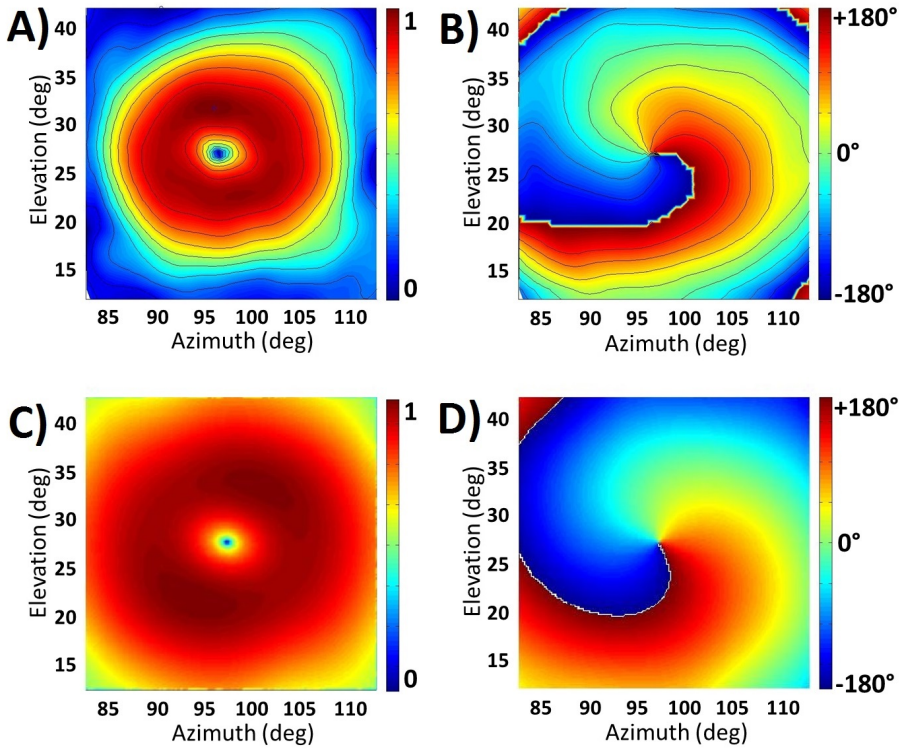

Figure 8.4: Electric field generated by a 8 patches circular array configured to produce a $\ell = -1$ OAM beam. A) measurement and C) simulation of the normalized intensity distribution. B) measurement and D) simulation of the phase distribution.

maps, of $\ell = 1$ and a $\ell = -1$ beam, are reported in Fig. 8.3 and 8.4, respectively. Azimuth and elevation values reported on the map axis correspond to the coordinates of the CCR on which the Tx array was mounted. So, the center of the map corresponds to the configuration where the transmitting and receiving antennas are aligned.

A good match between the expected fields and the measured ones was found. In fact, the experimental fields are characterized by a well defined doughnut distribution and the beams phase show the characteristic vortex shape with the central singularity. Vortices turn clockwise or counterclockwise, according to the negative or positive OAM value, by convention. From experimental results, the radiation pattern maximum gain is approximately equal to 10.5dBi both for the $\ell = 1$ and the $\ell = -1$ modes, in good agreement with FEM simulations, predicting about 11dBi.

On the other hand, also the OAM content carried by the experimental fields has been calculated. To this purpose, it has been used the spiral spectrum algorithm [45], which consists of projecting the EM field on helical harmonics, ($\exp(i\ell\phi)$ terms), similarly to a Fourier series. The spectra of the measured fields are shown in Fig. 8.5.

As can be observed, the fundamental azimuthal harmonics carry 90% and 85% of total power,

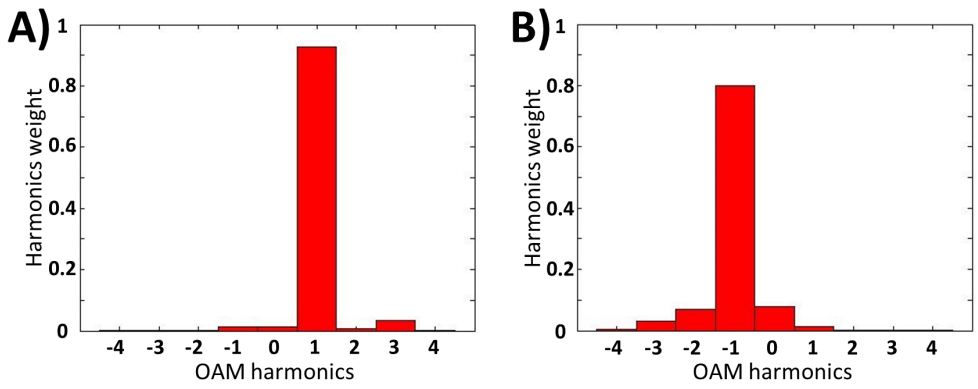

Figure 8.5: Spiral spectrum decompositions of the OAM field generated by circular arrays. A) spectrum of the $\ell = +1$ field shown in Fig. 8.3; B) spectrum of the $\ell = -1$ field shown in Fig. 8.4. The fundamental harmonic, in both cases, carries 90% and 82% of total fields energy, respectively.

for $\ell = 1$ and $\ell = -1$, respectively. Spurious harmonics are present, due to field imperfections; still, such spectra confirm the good quality of the generated OAM modes.

8.4.2 OAM waves synthesis robustness

A second series of experiments tested the dependence of the generated OAM fields on the number of radiating patch antennas. First, it has been sampled and observed an $\ell = 1$ field generated by eight radiating elements. In subsequent steps, the patch antennas were switched off one at a time, disconnecting them from their feeding cables, down to only one connected antenna. In order to prevent impedance mismatch at the Wilkinson output, the disconnected cables were closed on 50Ω dummy loads.

Fig. 8.6 reports some significant examples of field distributions, both in amplitude and phase, generated by array configurations with even numbers of patches.

The most important aspect to be stressed is that the phase singularity is present only when the sampling rule $N_{ant} > 2|\ell| + 1$ is satisfied. When the antenna number, N_{ant}, does not satisfy the condition for generating an $\ell = +1$ mode (see Fig. 8.6E-8.6F), the phase singularity disappears.

8.4.3 OAM-based communication

This section examines the experimental results of a communication system which exploits the mutual orthogonality of OAM states.

However, before continuing, it is useful to recall, in terms of geometrical properties, how the orthogonality plays a role in the OAM communication. When an OAM antenna (in this case, an array and its BFN) is used on the reception side, it behaves as an inverse phase plate, because the propagation direction is reversed (Chap. 2). In particular, this Rx OAM antenna imparts to

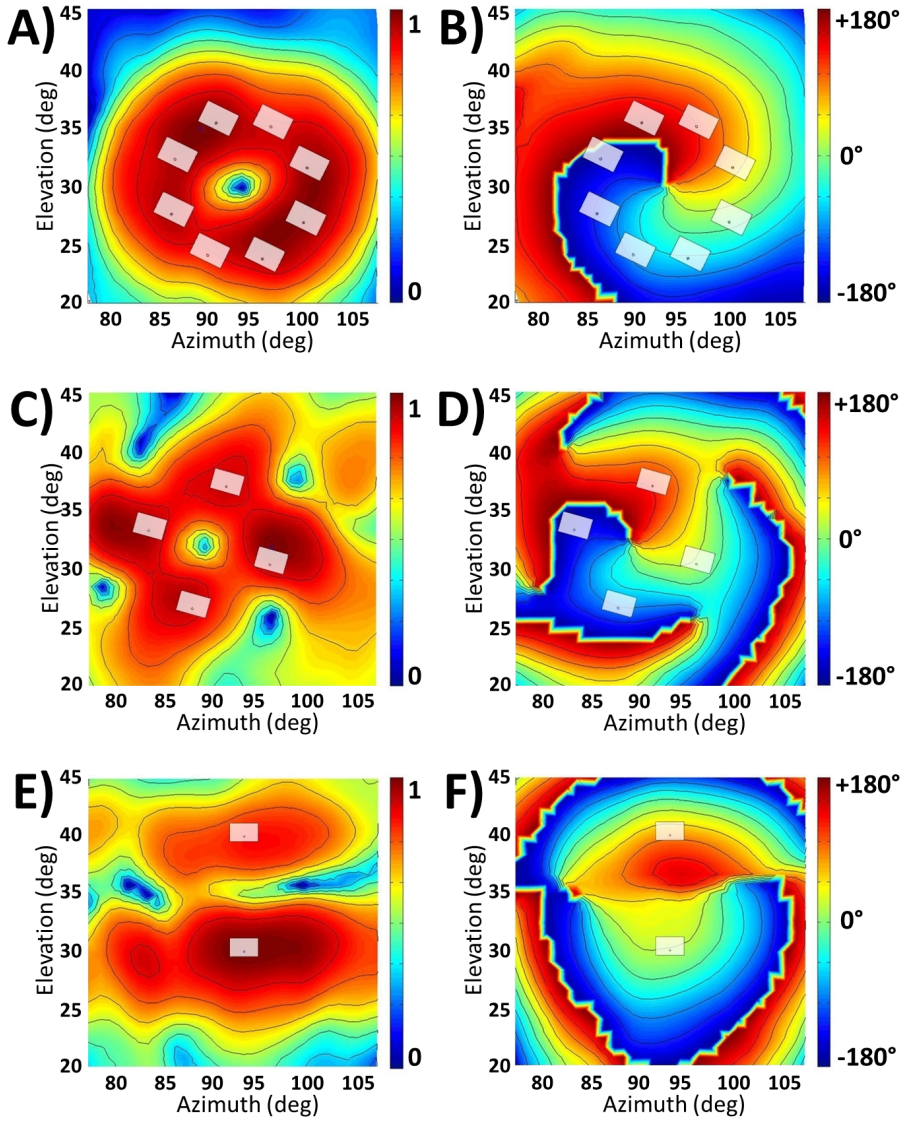

Figure 8.6: Normalized A), C), E) intensity and B), D), F) phase distributions of an $\ell = +1$ OAM beam generated by arrays composed by 8, 4 and 2 patches, respectively. The patch positions are shown on the maps by superimposed gray rectangles.

the i-th received field a phase delay $\exp(\mp i|\ell|\phi_n)$, ϕ_n being the angular position of the n-th patch, with $n = 1, ..., 8$. This phase is the opposite of what it would impart if used in transmission. Hence, an incoming field with left-handed (right-handed) topological charge is sampled in a right-handed (left-handed) way by the Rx array elements. In other words, a transmitting $\ell = +1$ antenna receives like a $\ell = -1$ one. The signal at the output of the Rx antenna sums the topological charge of the impinging beam to the topological charge of the Rx antenna in the reception mode.

Based on this, high output powers are expected when the Tx and Rx antennas are identical, much lower powers in all other cases.

To test such an OAM-based communication scheme, a system was assembled with the same ingredients used for the maps that were presented in the previous section. The Tx array was mounted on the CCR, while the Rx one was kept fixed, at 0.15m from Tx. The VNA, connected to the input and output ports of the BFN of the Tx and Rx sides, respectively, measured the S_{21} parameter, both in amplitude and phase in order to evaluate the channel gain for each position of the Tx array. The resulting data were reported on 2D maps.

In the first test, a transmitting $\ell = +1$ antenna communicates with an identical receiving one ($\ell = -1$ in reception mode, according to the change of propagation direction). In this case, intensity and phase distributions of Fig. 8.7 and Fig. 8.8 both resemble a standard (i.e., non-OAM) $\ell = 0$ field. These results prove that indeed two arrays of patch antennas designed for the

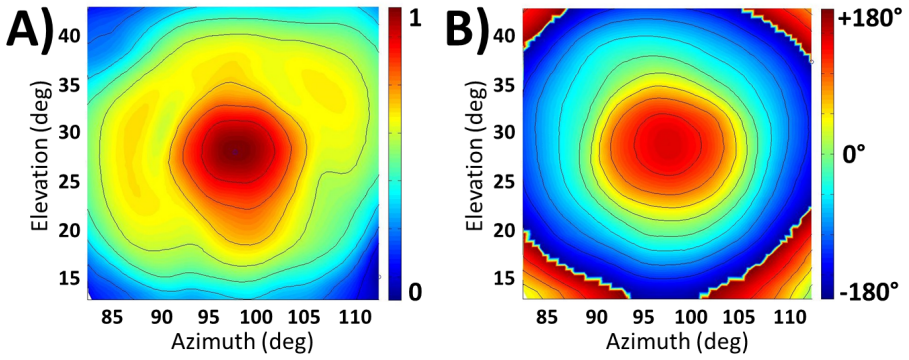

Figure 8.7: Normalized A) intensity and B) phase distributions of the electric field produced by a $\ell = +1$ wave received by means of a $\ell = -1$ circular array. As expected, the topological charge of the $\ell = +1$ wave is reset to zero by the receiving array: $\ell_{\text{wave}} + \ell_{\text{Rx}} = +1 - 1 = 0$.

same OAM topological charge can efficiently communicate with each other.

As a second test, the Tx array set to produce a $\ell = +1$ operated in pair with an opposite one, i.e., a patch array with BFN set to produce a $\ell = -1$, acting in reception mode as an $\ell = +1$, as stated above. The received twisted field is transformed into an $\ell = +2$ beam, as shown in Fig. 8.9. The split of singularities, visible in Fig. 8.9, is due to imprecision in the experimental setup, as confirmed by a vast literature dealing with generation of high-order OAM modes [155]. In this experimental setup, such deviations are mainly due to inaccuracies of the arrays and of their feeding lines. In fact, the feeding signals are affected by errors in amplitude and phase, as reported in Table 8.1-8.2 in the previous section. Even if these errors are very small, nonetheless the field patterns generated/recombined by the arrays are not perfectly balanced.

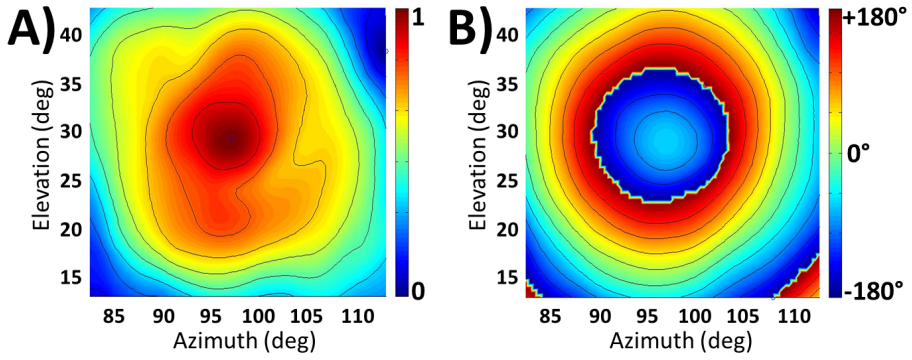

Figure 8.8: Normalized A) intensity and B) phase distributions of the electric field produced by a $\ell = -1$ wave received by means of a $\ell = +1$ circular array. As expected, the topological charge of the $\ell = -1$ wave is reset to zero by the receiving array: $\ell_{\text{wave}} + \ell_{\text{Rx}} = -1 + 1 = 0$.

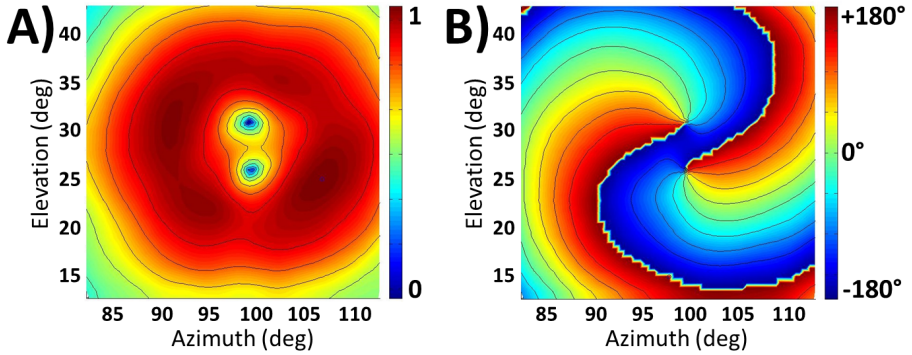

Figure 8.9: Normalized A) intensity and B) phase distributions of the electric field produced by a $\ell = 1$ wave received by a $\ell = +1$ circular array. An increase of the topological charge of the transmitted field is observed: $\ell_{\text{wave}} + \ell_{\text{Rx}} = +1 + 1 = +2$.

8.4.4 Tolerance to non-ideal position

The fourth series of experiments investigates the sensitivity of OAM-based communications to lateral shift and to angular tilt between the transmitting and the receiving arrays. For this purpose, two tests are developed. First, the system tolerance to a lateral shift of the transmitting array is tested, (see Fig. 8.10A). For different shifts, with respect to the perfect alignment, the powers of $\ell = 0$ and $\ell = 1$ modes, transmitted one at time and received by an $\ell = 0$ antenna are measured. In such a way, it is examined the relation between antennas alignment and modal isolation. For simplicity, these two powers are identified as P_{00} and P_{10}, respectively, where the fist index identifies the topological charge of the transmitting antenna, and the second one identifies that of the receiving one. The $\ell = 1$ mode was generated by 8 patch antennas, with the proper BFN, while the central patch antenna generated the standard $\ell = 0$ beam. The $\ell = 0$ and

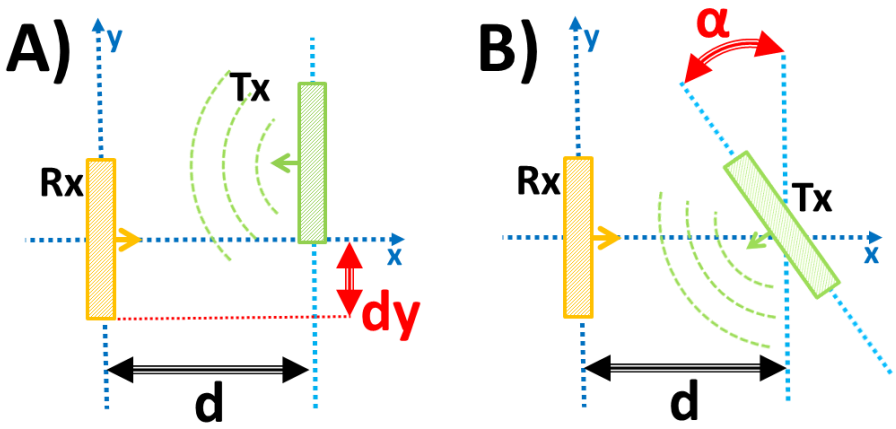

Figure 8.10: Outline of the Tx array movements: A) translation and B) tilt. d represents the distance between Tx and Rx arrays while d_y and α represent translation and tilt offsets, respectively.

the $\ell = 1$ antennas were connected alternatively, with a switch, to the first port of the VNA. The two modes were received by a single patch antenna, connected to the second port of the VNA, set to measure the S_{21} parameter. Tx and Rx antennas were positioned face to face at a distance equal to 0.15m. The Rx array was kept fixed, while the Tx one could move along a ruler parallel to the Rx array (see Fig. 8.11). At each translation step along the ruler, acting on the switch at

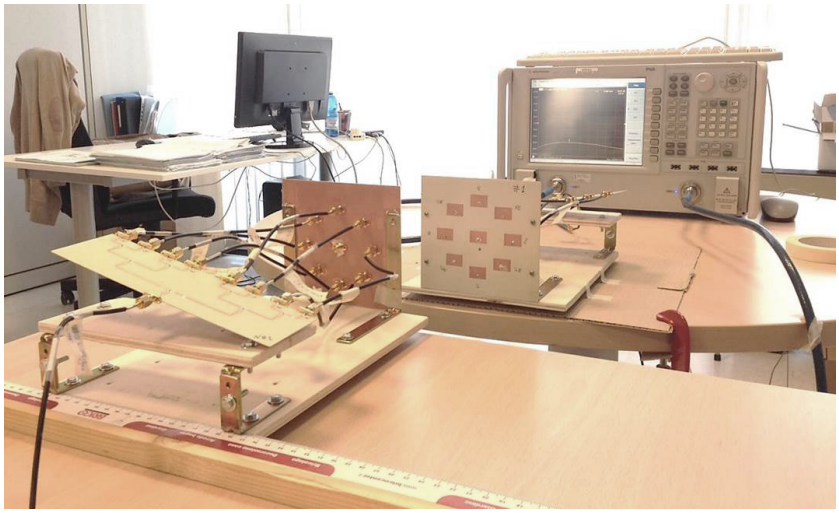

Figure 8.11: Experimental setup for the evaluation of the tolerance with respect to a lateral shift of the Tx array. The ruler, used to measure the translation shift, is visible on the bottom side.

Tx side, it has been transmitted once the $\ell = 0$ mode, once the $\ell = +1$ one. So, the receiving

antenna probed, alternately, powers from the two transmitted modes. The ratio P_{00}/P_{10} is shown in Fig. 8.12 (red dotted line) as a function of the lateral shift.

The entire procedure was then repeated after replacing the receiving single antenna with an $\ell = 1$ array. In this case, P_{11}/P_{01} was calculated, whose values vs. position are shown by the blue dotted line of Fig. 8.12. Both the red and the blue lines in Fig. 8.12 are characterized by a single

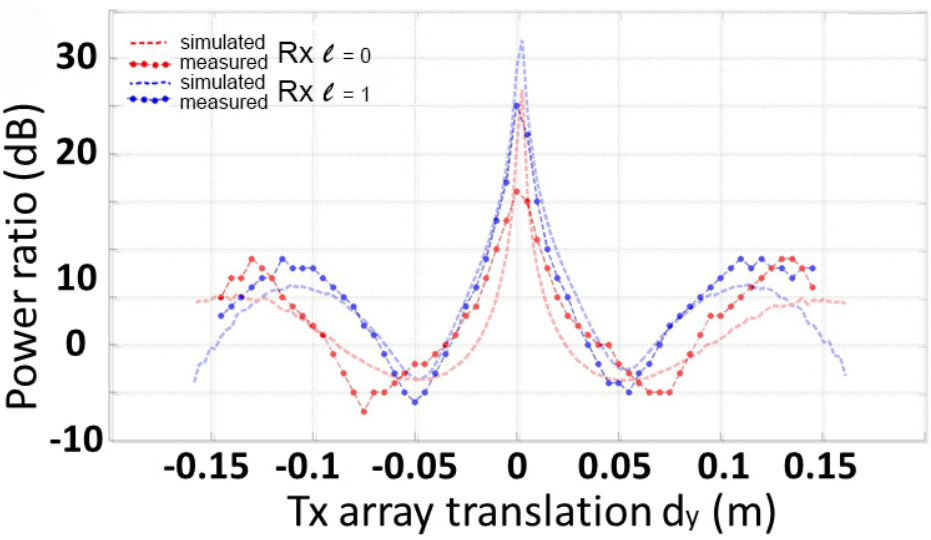

Figure 8.12: Measured and simulated power ratio as function of translated position d_y. Blue lines: P_{00}/P_{10}. Red lines: P_{11}/P_{01}. Dashed lines show simulated results while dotted lines show experimental ones.

central peak, that corresponds to perfect alignment between Tx and Rx arrays. This confirms that alignment is very important for modal isolation. The maximum of $\ell = 1$ channel is higher than the $\ell = 0$ one. This is due to the different number of active antennas (8 for the $\ell = 1$ mode, only one for the $\ell = 0$ mode). Both lines present steep edges: a little translation, with respect to perfect alignment, is sufficient to cause a strong degradation in power ratios. In particular, with these experimental conditions, a 1cm shift is sufficient to significantly enhance modal interference, with a drop of about 10dB in the power ratios.

For the sake of completeness, some simulations of these communication experiments have been performed by means of a numerical MIMO-based model [105] (App. C). Simulation have been performed taking into account phase errors on the patch feeding signals, reported in Table 8.1-8.2. Simulated results are given in Fig. 8.12: P_{00}/P_{10} is the red dashed line, P_{11}/P_{01} the blue dashed line. A good match between measurements and simulations is observed: the curve behavior, the peak positions, the minimum and inflection points coincide with good approximation. On the contrary, a small discrepancy is observed about the peak values. This can be explained

by the mathematical model applied for simulations. In fact, the simulated arrays are composed by elementary point sources and by loss-less BFN's, thus neglecting the dissipation of real BFN, and coupling between patches.

A second set of experimental tests was performed in order to evaluate the sensitivity of the OAM-based communication system to angular tilt between Tx and Rx arrays, (see Fig. 8.10B). Fig. 8.13 shows the Tx antenna, connected to the switch, mounted on the CCR. The antenna radiated alternatively the $\ell = 0$ mode and the $\ell = +1$ one, depending on the switch setting. Again,

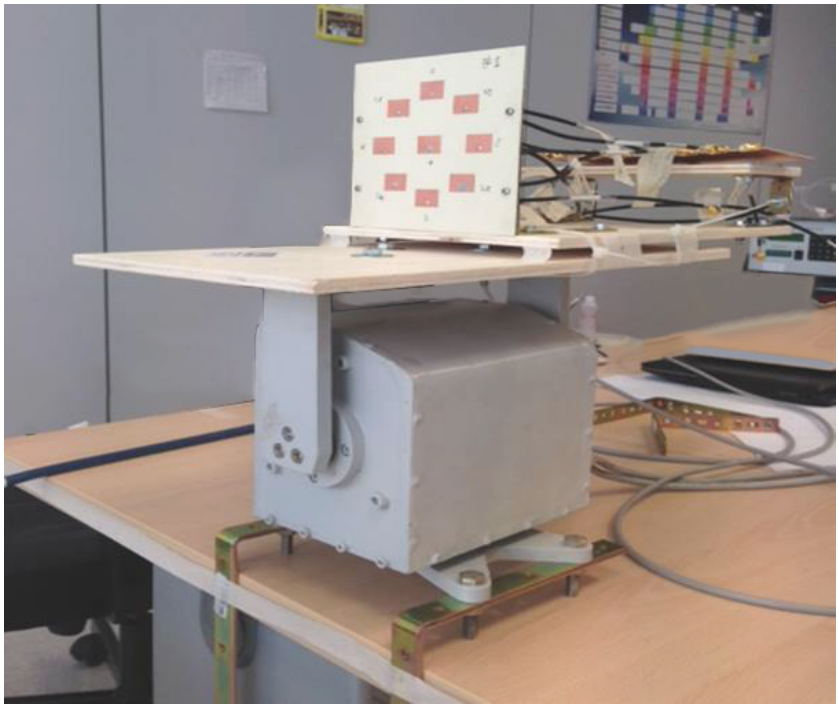

Figure 8.13: Experimental setup for the evaluation of the tolerance with respect to an angular tilt of the Tx array. Tx array is fixed on a CCR. These two devices share the same rotation axis.

the power ratios P_{00}/P_{10} and P_{11}/P_{01} are calculated, as functions of the tilt angle of the Tx array. The results are shown by the red and the blue dotted lines, respectively, in Fig. 8.14. Again, the central peak corresponds to perfect alignment. A tilting angle of 4° is sufficient to cause a drop of about 10dB in power ratio, for both lines.

Also this case presents strong similarities and some difference between simulated and measured power ratios. The main differences concern the slope of the curves, especially near the peaks, and their maximum values. These differences are ascribed to imperfect alignment between the axis of the CCR and that of the Tx array, which was mounted manually. Moreover, mechanical impairments of this low-cost setup could have caused additional small misalignment during the measurements. As in the previous case, simulations assumed arrays composed by

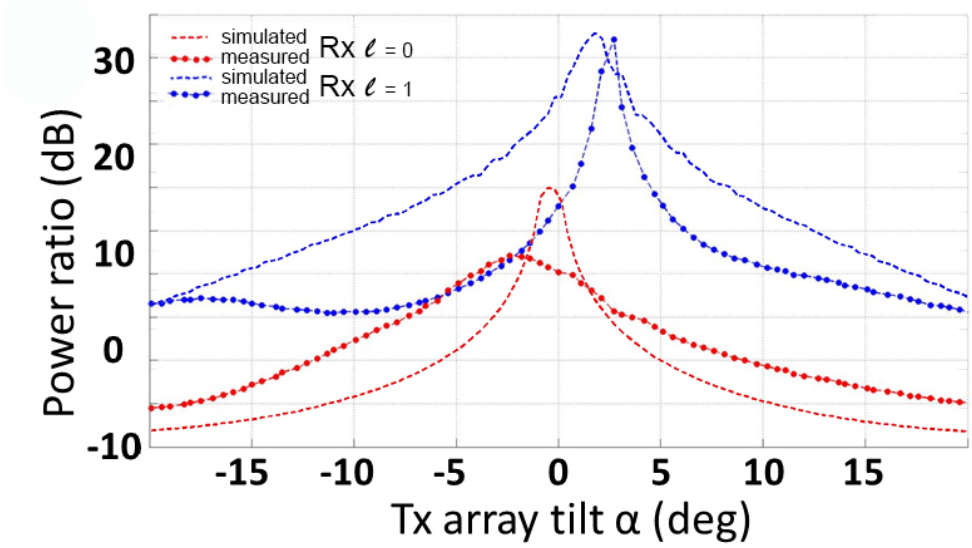

Figure 8.14: Measured and simulated power ratio as function of angularly tilted position α. Blue lines: P_{00}/P_{10}. Red lines: P_{11}/P_{01}. Dashed lines show simulated results while dotted lines show experimental ones.

elementary point sources, and loss-less BFNs. So, once again, the lower level of experimental curves is not surprising. Also, notice that the peaks of experimental power ratio are at different angular positions. This can be attributed to phase errors introduced by the BFN, as confirmed by simulated curves obtained introducing little random deviations in the matrices that describe the BFN behavior. Therefore, in conclusion, both simulations and experimental data show that in a communication system based on OAM modes the alignment between Tx and Rx antennas is of paramount importance. Moreover, special attention has to be paid also to the BFN of Tx and Rx antennas, in order to avoid unwanted inaccuracies.

8.5 OAM-based communication: a security application

The results presented in the previous section show how deeply the relative position between the Rx and Tx array affect the performances of a Line Of Sight (LOS) OAM-based link. In order to exploit OAM mode orthogonality, the Tx and Rx array planes must be aligned (Fig. 8.12, 8.14) and at a proper distance, such that the Rx array efficiently collects the main doughnut-shaped lobe of the emitted radiation. Deviations from this optimal configuration deteriorate communication rather drastically by means of mutual interference.

On one side, these geometrical constraints limit the applicability of an OAM-based communication, in terms of physical space suitable for receiving, but, on the other hand, this feature can

be of major interest in terms of security, for those applications where it is crucial that information exchanged between Tx and Rx cannot be intercepted by a third party, like exchange of personal data, electronic payments, etc. For an OAM-based communication link, the physical space where the signal can be intercepted can be much smaller than for a conventional system. To stress this point, an example can be helpful, where:

- Tx and Rx antennas are circular arrays, each comprising 9 linearly polarized patch antennas. As in the setup previously examined, one central patch is equipped for $\ell = 0$ mode, and 8 patches, placed along a circle, are for the $\ell = \pm 1$ ones;
- mutual coupling between patches of the same array is neglected;
- the system operation frequency is $f_0 = 5.75$GHz;
- the array radius is equal to $R = 0.05$m;
- BFNs are loss-less and designed to transmit/receive simultaneously 3 signals, carried by the $\ell = -1$, $\ell = 0$ and $\ell = +1$ OAM modes;
- the three signals are transmitted with equal powers;
- the Tx and Rx arrays face each other, aligned at a distance $d = 0.15$m; (notice that d is smaller than the array Fraunhofer length: $d_F = 2R^2/\lambda = 0.87$m, thus allowing OAM channel multiplexing [12]). Distance d has been calculated with the mathematical model described in the App. C, and imposing, for the three channels, a SNIR equal to 25dB;
- each of the three channels supports a digital modulation whose bit error rate is zero until the channel SNIR is larger than 15dB.

As previously discussed, a misalignment between Tx and Rx antennas causes a degradation of OAM modes orthogonality, and consequently an enhancement of channel cross-talk. To quantify this, the mathematical model described in Appendix C can be adopted to calculate the channel SNIR at different positions of the Rx array, while the Tx one is fixed. Numerical simulations allow then to determine the spatial boundaries within which all 3 channels can be received without errors.

The first simulation aims at studying the effects on the SNIR of a lateral shift between the array centers (similarly to Fig. 8.10A). Each position of the Rx array is identified by two parameters, the lateral displacement d_y and the distance d from the Tx array. From the simulation results, a receiving map can be drawn. As shown in Fig. 8.15A, all 3 channels can be received only within a limited area - red lines - around the perfect alignment position. In the yellow zone and in the green one, on the contrary, at most two channels can be correctly received. As previously suggested, this peculiar behavior can be exploited to enhance security: if the transmitted information is split

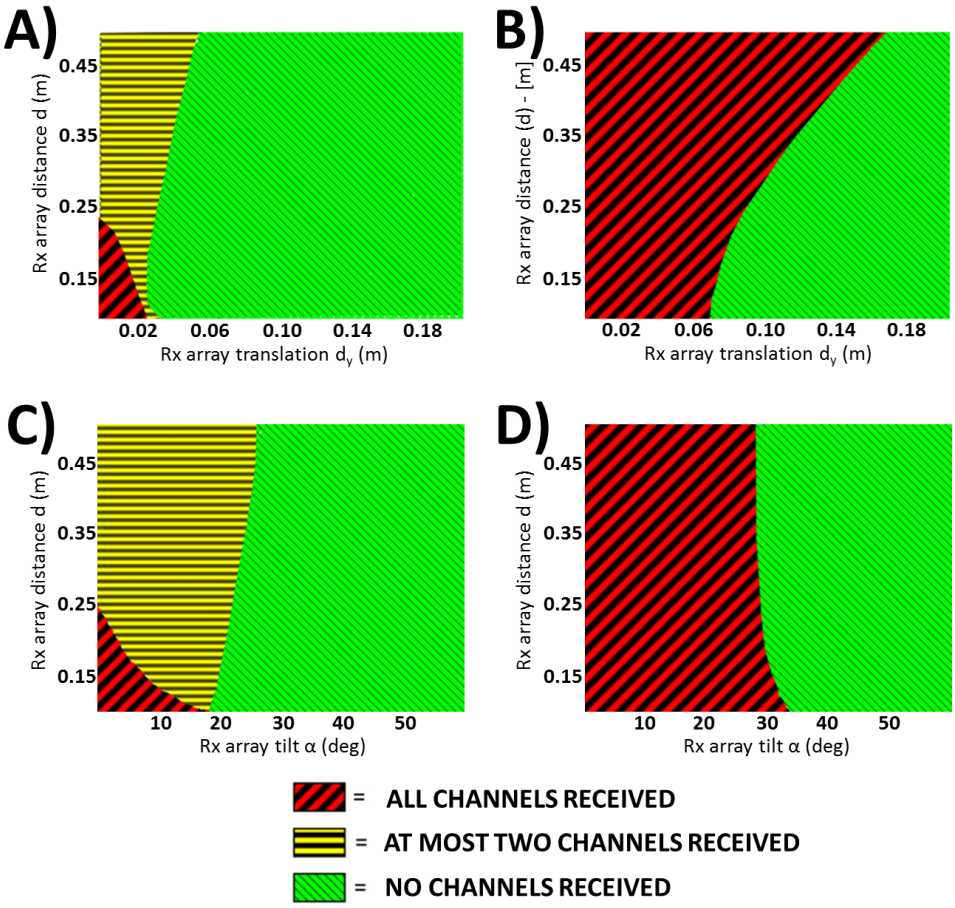

Figure 8.15: Maps of reception zones for A), C) multi-channels OAM based communication system and for B), D) single channel traditional ones. Vertical axis reports the distance between Tx and Rx arrays. Horizontal axis indicates A), B) lateral shift or C), D) angular tilt between Rx and Tx array. Red areas indicates physical space where the Rx array receives three channels. In yellow and green areas at most two channels can be correctly received.

over the three channels, it becomes very difficult to catch and reconstruct the whole data stream exchanged between Tx and Rx. The only way for an eavesdropper to intercept all the information is to stay very close to the legitimate Rx and almost perfectly aligned.

To better appreciate the advantage of OAM-based communications in terms of security, it is useful to study the behavior of an equivalent conventional system, with the same antenna structure, but based on a single channel over an $\ell = 0$ mode. The results obtained from simulations are collected in the map shown in Fig. 8.15B. This map consist only of two zones, only one channel being present in the communication process. The red zone, where information can be received correctly, is much larger than in the previous case. Comparing the two maps of Fig. 8.15A and B,

it is clear that the second configuration is more vulnerable to eavesdropping.

To complete this study, it is interesting to repeat the two aforementioned simulations in the presence of an angular tilt of the Rx array. The position of the Rx array is now identified by a tilt angle α, and by its distance d from the Tx array. The results are collected in the maps of Fig. 8.15C and Fig. 8.15D for the OAM-based system and for the conventional one, respectively. As expected, also in this second configuration the OAM-based system is characterized by a smaller reception volume, with respect to the traditional one. In fact, the tilt misalignment prevents the Rx array from correctly recognizing the transmitted OAM modes, with a consequent increase of channel cross-talk.

8.6 Conclusions

This chapter examined line of sight short range communications based on OAM modes. In particular, it studied a near field communication link, composed by circular arrays of patch antennas, that transmit and receive OAM fields with topological charge $\ell = -1, 0, +1$ at the frequency of 5.75GHz. By means of simulations and experiments, it evaluated the link communication performances with respect to Tx and Rx antennas alignment. The results proved that, also in a short range context, the natural orthogonality of OAM modes can assure a high channel isolation, provided the Tx and Rx OAM-antennas are well aligned. These results strengthen the idea that OAM modes are valuable tools in order to develop new multi-channel high-rate data links with low complexity processing, as already suggested by [91].

In addition to that, it has been examined a new application of OAM modes. As proved by numerical simulations, OAM fields can be used to increase the security level of communications, preventing non-authorized interceptions much more efficiently that conventional systems comparable in size and physical complexity. Up to now, the potential of this new application has been confirmed by numerical simulations which clearly underlined the security enhancement of OAM-based systems. However, the mathematical model used in numerical simulations has been validated by experimental results.

For all these reasons, OAM waves represents a promising tool to improve different short range communication characteristics directly at the physical layer, without digital post processing.

Conclusions

The aim of this thesis was to study the application of OAM waves to radio communication systems, with particular attention to long range and short range line-of-sight links. In fact, since OAM waves form a complete orthogonal set, they represent an interesting tool to implement new multiplexing systems where several channels, associated to different OAM modes, can be transmitted on the same frequency.

The study of this topic started with the experimental verification of OAM waves orthogonality in the radio domain. Afterward, long range multiplexing systems have been considered and different line-of-sight radio links have been tested in urban environments. The experiments, however, showed that orthogonality can not be naturally exploited when only a small portion of field is received. For this reason, different techniques have been proposed to solve this issue, like the superposition of fields with consecutive and opposite values of OAM or higher order OAM modes. Also partial reception schemes, where different OAM waves are distinguished by means of MIMO systems, have been considered and, later, used to compare the communication performances of OAM-based systems with respect to MIMO ones. In the end, the application of OAM waves to short range communication systems has been evaluated since, in such configurations, the orthogonality can be naturally exploited. In particular, it has been examined how OAM modes can be used to enhance the communication security level and to prevent non-authorized interceptions.

Looking at the main results described in the thesis, it is possible to draw two main conclusions about the application of OAM waves in line-of-sight communications. First of all, a generic spatial multiplexing system presents the same performances whether it is based on OAM waves or on MIMO techniques. In other words, the use of OAM modes in a generic communication link do not allow to reach higher data rates with respect to current MIMO technology. Second, in order to take advantage of OAM modes natural orthogonality and to avoid the requirement of digital post processing, it is fundamental to properly align both the transmitting and the receiving antennas and to ensure that the whole electromagnetic field is received. This latter feature represents a strong constrain to a profitable application of OAM waves because, even though OAM fields

are naturally orthogonal, they represent a less versatile solution with respect to modern MIMO techniques.

In conclusion, as suggested by several results presented in the thesis, OAM waves may be an interesting tool only when applied to short range communication systems. Here, they can be employed to implement static high-rate low-power consumption data links that can be used, for example, within data centers or server farms. Moreover, they can represent a promising solution also for future applications in which high security communications are required.

Appendix A

Angular spectrum representation

It is well known, from linear algebra, that there exist several ways to represent a vector in space. In particular, the representation depends on the chosen reference system in which the vector is inserted. In other words, the same vector can be expressed in different ways depending on the base that is used. The same concept can be applied also to EM fields that can be represented using an appropriate sum of waves belonging to a complete orthogonal set.

The method that will be examined in this appendix is the so called *angular spectrum representation* that consist in expressing an EM field by sum of plane and evanescent waves [19, 141]. This technique is particularly useful for two reasons: the simple expression of the plane wave set and its simplicity to describe generic fields.

The angular spectrum of a generic electric field $\mathbf{E}(\mathbf{r},t) = \mathbf{E}(\mathbf{r})e^{-i\omega t}$, propagating along $\hat{\mathbf{z}}$ in an isotropic, homogeneous, linear and source-free Cartesian space $\mathbf{r} = (x,y,z)$, can be calculated, considering the field distribution in a z-constant plane as:

$$\tilde{\mathbf{E}}(k_x,k_y,z) = \frac{1}{2\pi}\int_{-\infty}^{\infty}\int_{-\infty}^{\infty}\mathbf{E}(x,y,z)e^{-i(k_x x+k_y y)}\,dxdy \tag{A.0.1}$$

where ω is the field frequency and k_x and k_y are the so called *spatial frequencies* or reciprocal coordinates. From Eq. A.0.1 it is clear that the angular spectrum calculation can be viewed as a 2D Fourier Transform (FT) where the Fourier harmonics are represented by plane waves with different wave-vectors: k_x and k_y. Reminding the properties of FT, the inverse process is:

$$\mathbf{E}(x,y,z) = \frac{1}{2\pi}\int_{-\infty}^{\infty}\int_{-\infty}^{\infty}\tilde{\mathbf{E}}(k_x,k_y,z)e^{i(k_x x+k_y y)}\,dk_x\,dk_y \tag{A.0.2}$$

Since $\mathbf{E}(\mathbf{r})$ is an EM wave, it has to satisfy Helmholtz equation $(\nabla^2+K^2)\mathbf{E}(\mathbf{r}) = 0$, with $K = \omega\sqrt{\mu\epsilon}$ its wave-number. This leads to a new expression for the field angular spectrum:

$$\tilde{\mathbf{E}}(k_x,k_y,z) = \tilde{\mathbf{E}}(k_x,k_y,0)e^{\pm ik_z z} \tag{A.0.3}$$

where the parameter k_z is defined as:

$$k_z = \sqrt{K^2 - k_x^2 - k_y^2} \tag{A.0.4}$$

Eq. A.0.3 describes the propagation along $\hat{\mathbf{z}}$ of each plane wave of the spectrum only by means of the $e^{\pm ik_z z}$ factor. Moreover, each wave direction can overlap with the positive direction of the $\hat{\mathbf{z}}$ axis or with the negative one, as stated by the $\pm$ sign. Eq. A.0.3 is a valuable tool because it allows to calculate the field spectrum at a generic z-plane only by means of the distribution at the $z = 0$ one. On the other hand, Eq. A.0.4 states also that there are no restrictions on the k_z parameter: it can be either real or imaginary. Depending on its value, determined by k_x and ky, the angular spectrum is composed by plane or evanescent waves.

A.0.1 Angular spectrum of paraxial waves

Paraxiality is a particular property of EM fields concerning their propagation: it states that the longitudinal field components varies slowly than the transversal ones. In other words, a paraxial beam is characterized by a very weak diffraction rate. Considering its angular spectrum, it will be composed by plane waves with a $\mathbf{k} = (k_x, k_y, k_z)$ wave vector almost parallel to the field propagation direction. In other words, the vector components k_x and k_y are very small with respect to $|\mathbf{k}|$ and k_z can be approximated as:

$$k_z = \sqrt{K^2 - k_x^2 - k_y^2} \approx K - \frac{k_x^2 + k_y^2}{2K} \tag{A.0.5}$$

For all these reasons, the angular spectrum of a paraxial field is always composed by propagating waves and not by evanescent ones.

A.1 Angular spectrum of a Gaussian beam

The angular spectrum decomposition can be very useful to describe generic electromagnetic fields. As example, a Gaussian beam within a Cartesian reference system (x, y, z) will be examined. For simplicity, the field time dependence $\exp(i\omega t)$ is omitted.

The beam electric field components, in the $z > 0$ space, can be expressed as [156]:

$$E_x(\mathbf{r}) = \int_{-\infty}^{+\infty} \int_{-\infty}^{+\infty} A_x(k_x, k_y) \exp\left[i(k_x x + k_y y + k_z z)\right] dk_x dk_y, \tag{A.1.1}$$

$$E_y(\mathbf{r}) = \int_{-\infty}^{+\infty} \int_{-\infty}^{+\infty} A_y(k_x, k_y) \exp\left[i(k_x x + k_y y + k_z z)\right] dk_x dk_y, \tag{A.1.2}$$

$$E_z(\mathbf{r}) = -\int_{-\infty}^{+\infty} \int_{-\infty}^{+\infty} \left[\frac{k_x}{k_z} A_x(k_x, k_y) + \frac{k_y}{k_z} A_y(k_x, k_y)\right] \exp\left[i(k_x x + k_y y + k_z z)\right] dk_x dk_y, \tag{A.1.3}$$

where the z-axis is taken to be the propagation direction and Eq. A.1.3 has been determined combining Maxwell divergence equation 1.2.2 in a space free of charges with Eq. A.1.1 and A.1.2. The field wave vector square magnitude is equal to $K^2 = \left(\omega\sqrt{\mu\epsilon}\right)^2 = k_x^2 + k_y^2 + k_z^2$ with:

$$k_z = \sqrt{\left(K^2 - k_x^2 - k_y^2\right)} \tag{A.1.4}$$

for propagating waves and

$$k_z = i\sqrt{\left(k_x^2 + k_y^2 - K^2\right)} \tag{A.1.5}$$

for evanescent ones.

To find the coefficients A_x and A_y it can be used Eq. A.0.3 together with a boundary problem approach. First of all, it is necessary to determine an Ansaz for the electric field at origin plane $z = 0$: it is reasonably to assume that its distribution is Gaussian, polarized along $\hat{\mathbf{x}}$ and equal to:

$$E_x(x, y, 0) = E_{0x} \exp\left(- \frac{\rho^2}{2w_0^2}\right), \tag{A.1.6}$$

where E_{0x} is the field magnitude factor and w_0 is a parameter called *beam waist* accounting for the beam radius. Using the inverse Fourier transform, $A_x(k_x, k_y, 0)$ can be determined as

$$A_x(k_x, k_y, 0) = E_{0x} \frac{w_0^2}{2\pi} \exp\left(- k^2 w_0^2/2\right), \tag{A.1.7}$$

where $k^2 = k_x^2 + k_y^2$. Now, since a Gaussian beam is invariant under rotations around the z-axis, cylindrical coordinates can be employed rather than Cartesian ones. Replacing $dk_x dk_y$ with $kdkd\theta$, performing the angular integration and introducing the zeroth and first-order Bessel function of the first kind, the desired field components can be derived:

$$E_x(\mathbf{r}) = E_{0x} \int_0^\infty w_0^2 \exp\left(- k^2 w_0^2/2\right) \exp\left(ik_z z\right) J_0\left(k\rho\right) kdk, \tag{A.1.8}$$

$$E_z(\mathbf{r}) = -iE_{0x} \sin\theta \int_0^\infty \frac{k^2 w_0^2}{k_z} \exp\left(- k^2 w_0^2/2\right) \exp\left(ik_z z\right) J_1\left(k\rho\right) dk, \tag{A.1.9}$$

with $\sin(\theta) = x/\rho$. As can be noticed, the field y-component is no longer present due to polarization assumption and the z-one is different from zero in order to satisfy the divergence Maxwell equations in a space free of charges.

A.1.1 Contributions of Evanescent and Propagating Waves

To determine the contribution of evanescent and propagating waves on the field just derived in Eq. A.1.8 and A.1.9 it is necessary to separate the integration performed over *k* as $\int_0^{k_0} + \int_{k_0}^\infty$ with $k_0 = K$. In fact, the first and the second integrations correspond to propagating and evanescent

waves, respectively. To avoid the paradox that occurs at $k = k_0$, which is equivalent to $k_z = 0$, the integration must be performed over the normal component of the wave vector:

$$E_x(\mathbf{r}) = \left[\int_0^{k_0} - \int_0^{i\infty} \right] E_{0x} w_0^2 \exp\big(- k^2 w_0^2/2\big) \exp\big(ik_z z\big) J_0\big(k\rho\big) k_z dk_z, \tag{A.1.10}$$

$$E_z(\mathbf{r}) = \left[\int_0^{k_0} - \int_0^{i\infty} \right] E_{0x} w_0^2 \exp\big(- k^2 w_0^2/2\big) \exp\big(ik_z z\big) J_1\big(k\rho\big) k dk_z, \tag{A.1.11}$$

In a more detailed form, Eqs. (A.1.10) and (A.1.11) become

$$E_{x,pro}(\mathbf{r}) = E_{0x} \int_0^{k_0} w_0^2 \exp\Big[- (k_0^2 - k_z^2) w_0^2/2 \Big] \exp\big(ik_z z\big) J_0\Big(\sqrt{k_0^2 - k_z^2}\rho \Big) k_z dk_z, \tag{A.1.12}$$

$$E_{x,eva}(\mathbf{r}) = E_{0x} \int_0^{\infty} w_0^2 \exp\Big[- (k_0^2 + \alpha^2) w_0^2/2 \Big] \exp\big(i\alpha z\big) J_0\Big(\sqrt{k_0^2 + \alpha^2}\rho \Big) \alpha d\alpha, \tag{A.1.13}$$

$$E_{z,pro}(\mathbf{r}) = E_{0x} \int_0^{k_0} w_0^2 \exp\Big[- (k_0^2 - k_z^2) w_0^2/2 \Big] \exp\big(ik_z z\big) J_1\Big(\sqrt{k_0^2 - k_z^2}\rho \Big) \sqrt{k_0^2 - k_z^2} dk_z, \tag{A.1.14}$$

$$E_{z,eva}(\mathbf{r}) = -iE_{0x} \int_0^{\infty} w_0^2 \exp\Big[- (k_0^2 + \alpha^2) w_0^2/2 \Big] \exp\big(i\alpha z\big) J_1\Big(\sqrt{k_0^2 + \alpha^2}\rho \Big) \sqrt{k_0^2 + \alpha^2} d\alpha, \tag{A.1.15}$$

where the subscript *eva* and *pro* mean that the integration corresponds to the evanescent and propagating waves, respectively. One can immediately note, from Eq. A.1.13 and A.1.15, that the integration that represents the evanescent waves is real for the x component and imaginary for the *z* one. The integrations represented by Eqs. A.1.12 - A.1.15 can be inconvenient to perform. However, with the use of some smart mathematical tools, they can be written as an infinite sum of terms. In particular they result to be a power series of the $\lambda/(2\pi w_0)$. A more detailed mathematical description can be find in [156].

Since Eq. A.1.12 - A.1.15 are mathematically complicated, the amount of propagated and evanescent waves can be observed with the help of graphics. In Fig. A.1, A.2, A.3 the module of the field components are represented both for propagating (Eq. A.1.12 and A.1.14) and for evanescent contributions, (Eq. A.1.13 and A.1.15), for three particular configuration of λ and w_0.

First, $w_0 < \lambda$ is examined. Looking very close to the field origin at $z = 5\lambda$ (see Fig. A.1) it results that the maximum peak of the z-component is $\approx 2.4\%$ with respect to the x-one and the evanescent contribution are relevant with respect to the total field. However, when moving far from origin on the z-axis, (at $z = 50\lambda$ in Fig. A.2), the ratio between the maximum peaks of x- and the z-components is still quite the same ($\approx 2.6\%$) that in Fig. A.1 but the evanescent contribution are negligible. On the contrary, if $w_0 = \lambda$ as in Fig. A.3 the contribution of the evanescent field is definitely negligible, just at few λ of distance together with the z-component of the electric field.

From this example it is clear that the contribution of evanescent waves is completely negligible, in general, when the beam size at the origin is greater than the wavelength, $w_0 \gtrsim \lambda$. On the

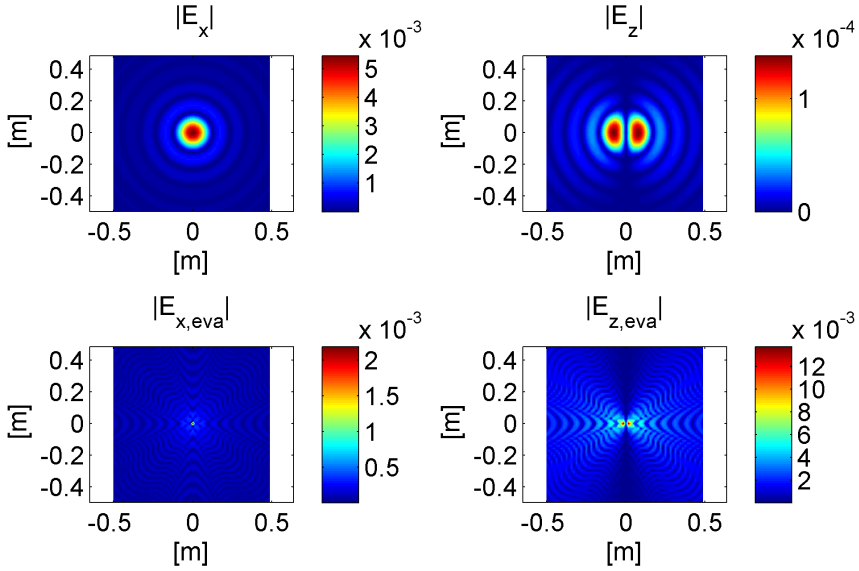

Figure A.1: Intensity of total components A.1.10, A.1.11 (top) and evanescent components A.1.13, A.1.15 (down) of electric field at $z = 5\lambda$ and $w_0 = 0.5\lambda$

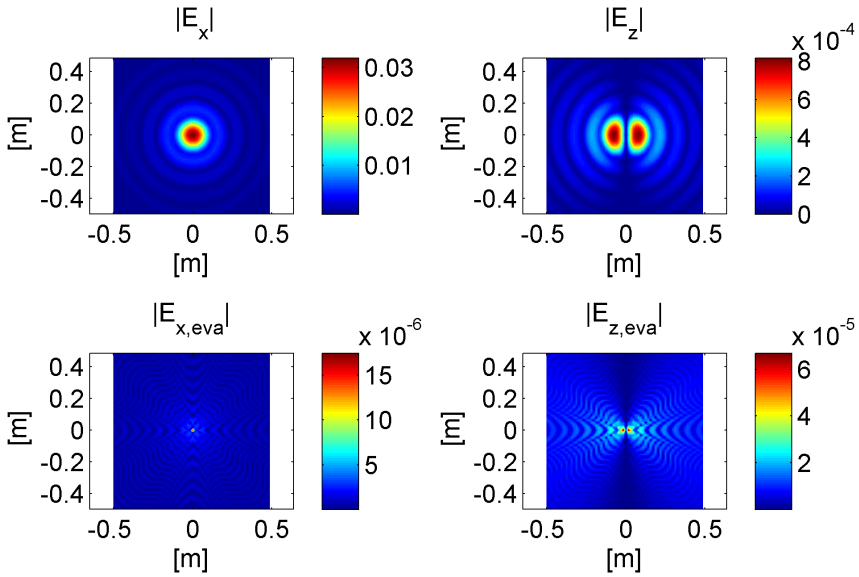

Figure A.2: Intensity of total components A.1.10,A.1.11 (top) and evanescent components A.1.13, A.1.15 (down) of electric field at $z = 50\lambda$ and $w_0 = 0.5\lambda$

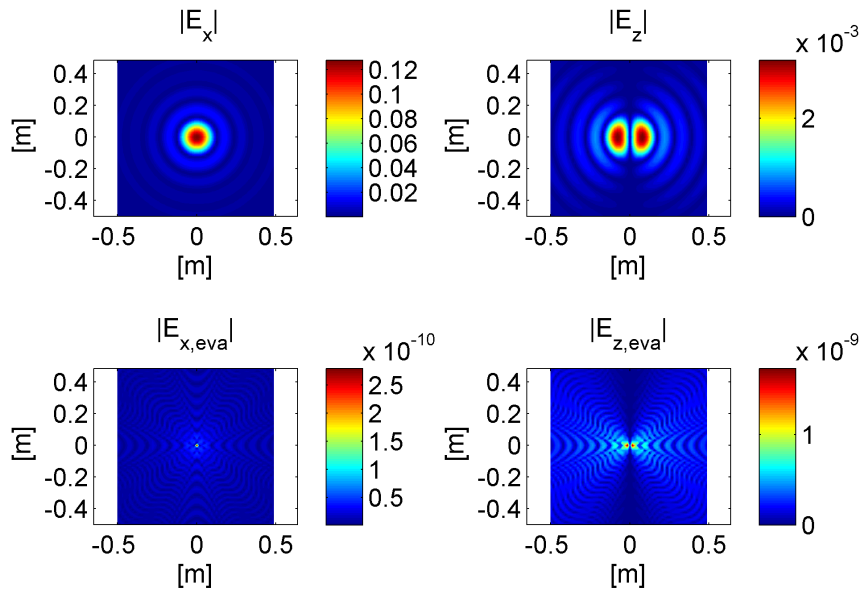

Figure A.3: Intensity of total components A.1.10, A.1.11 (top) and evanescent components A.1.13, A.1.15 (down) of electric field at $z = 5\lambda$ and $w_0 = \lambda$

contrary, even the z-component of the electric field have an important role in the far field zone when the beam is generated by a sub-wavelength aperture. In the end, remembering the previous section, it appears that a paraxial Gaussian beam can be generated only from an aperture greater than λ.

The same behavior can be observed also for the main lobe of electromagnetic fields generated by circular arrays: when the array diameter is greater than λ the contribution of evanescent waves is negligible. On the contrary, when the diameter is smaller than λ, the contribution of evanescent waves is fundamental in the angular field representation. For this reason, to generate a field with a paraxial main lobe by using a circular array it is mandatory to choose an array diameter greater than λ.

Appendix B

The paraxiality estimator

In this appendix it will be examined a quantity called *degree of paraxiality operator* or *paraxiality estimator* $\mathcal{P}$, which allows to determine if a generic EM field is paraxial [157, 158].

A generic monochromatic time independent electric field $\mathbf{E}(\mathbf{r})$, in a Cartesian reference system $\mathbf{r} = (x, y, z)$, propagating along $\hat{\mathbf{z}}$, fulfills the vector Helmholtz Equation (HE):

$$\nabla^2\mathbf{E}(\mathbf{r}) + k^2\mathbf{E}(\mathbf{r}) = 0 \tag{B.0.1}$$

where k is the wave vector magnitude. Assuming that $\mathbf{E}(\mathbf{r})$ is paraxial, it can be written as

$$\mathbf{E}(\mathbf{r}) = \mathbf{A}(\mathbf{r})e^{ikz} \tag{B.0.2}$$

where $\left|\partial_z^2\mathbf{A}(\mathbf{r})\right| \ll |2ik\partial_z\mathbf{A}(\mathbf{r})|$ as stated from the paraxial approximation. Therefore, Eq. B.0.1 simplifies into the Paraxial Equation (PE):

$$\nabla_t^2\mathbf{A} + 2ik\partial_z\mathbf{A} = 0, \tag{B.0.3}$$

with the Laplacian operator broken up into its transversal and longitudinal components. If the paraxial approximation is fulfilled, Eqs. B.0.1 and B.0.3 are physically equivalent. However, from a mathematical point of view, they present different *propagation invariants*, i.e. different quantities that remain constant during propagation.

To find the propagation invariant of Eq. B.0.1 it is useful to assume that an electric field $\mathbf{E}_h$, with a finite intensity distribution ($\lim_{x,y\to\pm\infty}\mathbf{E}_h = 0$), is a solution of Eq. B.0.1. After some algebraic manipulations and integrating over a transverse plane $z =$ const., it results that:

$$\frac{\partial}{\partial z}\left[\int_{-\infty}^{+\infty} \mathrm{Im}\left\{\mathbf{E}_h^* \cdot \partial_z\mathbf{E}_h\right\} dxdy\right] = 0, \tag{B.0.4}$$

Therefore $\int_{-\infty}^{+\infty} \mathrm{Im}\left\{\mathbf{E}_h^* \cdot \partial_z\mathbf{E}_h\right\} dxdy$ is a propagation invariant of Eq. B.0.1. In addition, the electromagnetic power carried by the field and crossing the infinite plane $z =$ const. can be determined

from Eq. B.0.4 as:

$$W_{HE} = \epsilon\omega \frac{\int_{-\infty}^{+\infty} \text{Im}\left\{\mathbf{E}_h^* \cdot \partial_z \mathbf{E}_h\right\} dxdy}{2k^2} \tag{B.0.5}$$

For this reason, $\int_{-\infty}^{+\infty} \text{Im}\left\{\mathbf{E}_h^* \cdot \partial_z \mathbf{E}_h\right\} dxdy$ is also called HE-*power invariant*.

On the other hand, to find the propagation invariant of Eq. B.0.3, it is useful to assume that an electric field $\mathbf{E}_p$, with a finite intensity distribution ($\lim_{x,y\to\pm\infty}\mathbf{E}_p = 0$), is a solution of Eq. B.0.3. After some algebraic manipulations and integrating over a transverse plane $z =$ const. it results that:

$$\frac{\partial}{\partial z}\left[\int_{-\infty}^{+\infty} \mathbf{E}_p \cdot \mathbf{E}_p^* k dxdy\right] = 0, \tag{B.0.6}$$

so that $\int_{-\infty}^{+\infty} \mathbf{E}_p \cdot \mathbf{E}_p^* k dxdy$ is and invariant of Eq. B.0.3. Similarly to the previous case, the electromagnetic power crossing an infinite plane $z =$ const., can be calculated from Eq B.0.6 as:

$$W_{PE} = \epsilon\omega \frac{\int_{-\infty}^{+\infty} \mathbf{E}_p \cdot \mathbf{E}_p^* k dxdy}{2k^2} \tag{B.0.7}$$

and $\int_{-\infty}^{+\infty} \mathbf{E}_p \cdot \mathbf{E}_p^* k dxdy$ is also called PE-*power invariant*.

It is now interesting to examine the ratio between the above power invariants when a paraxial field is considered. Keeping a field $\mathbf{E}(\mathbf{r})$ expressed as product of magnitude and phase, $\mathbf{E}(\mathbf{r}) = \bar{\Psi}(\mathbf{r})e^{i\phi(\mathbf{r})}$, it results that the ratio W_{HE}/W_{PE} is equal to:

$$\frac{\int_{-\infty}^{+\infty} \text{Im}\left\{\mathbf{E}_h^* \cdot \partial_z \mathbf{E}_h\right\} dxdy}{\int_{-\infty}^{+\infty} \mathbf{E}_p \cdot \mathbf{E}_p^* k dxdy} = \frac{\int_{-\infty}^{+\infty} \Psi_h^2 (k + \partial_z \phi_h) dxdy}{\int_{-\infty}^{+\infty} \Psi_p^2 k dxdy}. \tag{B.0.8}$$

It is immediate to notice that if the paraxial approximation fulfils $\Leftrightarrow k \gg |\partial_z \phi_h| \Leftrightarrow \bar{\Psi}_h \cong \bar{\Psi}_p$ then the HE and the PE solutions are physically equivalent. Under such condition, the ratio of Eq. B.0.8 is almost equal to 1. Otherwise, if $|\partial_z \phi_h|$ is not much less than k, (i.e. the field is not paraxial), then $\bar{\Psi}_h \ncong \bar{\Psi}_p$ and the ratio of Eq. B.0.8 is different from 1. This behavior is caused by the fast oscillations of the non paraxial field that are not completely described by e^{ikz} term but only by the $e^{i\phi(\mathbf{r})}$one.

The above analysis suggests that Eq. B.0.8 is the base by which to define an efficient *paraxiality estimator* $\mathcal{P}$ as

$$\mathcal{P} = \frac{\int_{-\infty}^{+\infty} \text{Im}\left\{\mathbf{E}^* \cdot \partial_z \mathbf{E}\right\} dxdy}{\int_{-\infty}^{+\infty} \mathbf{E} \cdot \mathbf{E}^* k dxdy}. \tag{B.0.9}$$

Eq. B.0.9 can lead to some problems when trying to explicitly compute such integral energy flows. In particular, the partial derivation in z could sometimes represent a waist in terms of computational power. For this reason, it is possible to invoke Parseval theorem and find an equivalent, much easier, expression for $\mathcal{P}$ which can be written as:

$$\mathcal{P} = \frac{\int_{-\infty}^{+\infty} \text{Im}\left\{\bar{\epsilon}^* \cdot \partial_z \bar{\epsilon}\right\} dudv}{\int_{-\infty}^{+\infty} \bar{\epsilon} \cdot \bar{\epsilon}^* k dudv}. \tag{B.0.10}$$

where $\bar{\epsilon}(u,v) = \mathcal{F}^{-1}\big(\mathbf{E}(\mathbf{r})\big)$ is the vectorial plane-wave spectrum for the electric field $\mathbf{E}$ on $z =$ const. plane, (see App. A).

Concluding, $\mathcal{P}$ represents the paraxiality degree of an EM beam. It is clear that $0 < \mathcal{P} < 1$ always holds. For a fully non-paraxial field, the denominator in Eq. B.0.9 is much larger than the numerator and $\mathcal{P}$ vanishes. On the contrary, $\mathcal{P} = 1$ for a completely paraxial field, since the two integrals in Eq. B.0.9 tend to coincide. In all intermediate situations, the field will be partially paraxial.

Appendix C

MIMO mathematical model

In this appendix the mathematical model used to describe MIMO systems of Chap. 7 and 8 will be examined. The model consists in a description of MIMO behavior by means of linear algebra and by a characterization of the communication channel through the ray tracing method. The reader interested in a full description of all these tools can refer to [105].

A generic communication system based on spatial multiplexing, (Fig. C.1), consists of the following elements: input data streams, precoder, transmitting (Tx) array, communication channel, receiving (Rx) array, postcoder, and output data streams. Input and output data can be described with column vectors, respectively $\mathbf{x} \in \mathbb{C}^{N_s}$ and $\mathbf{y} \in \mathbb{C}^{N_s}$, where N_s is the number of independent streams. The precoder, whose purpose is to map the input data streams onto the set of Tx antennas, determines the physical power fed into each Tx element. It can be modeled with a matrix $\mathbf{P} \in \mathbb{C}^{N_{Tx} \times N_s}$ where N_{Tx} is the number of transmitting antennas. Also the communication

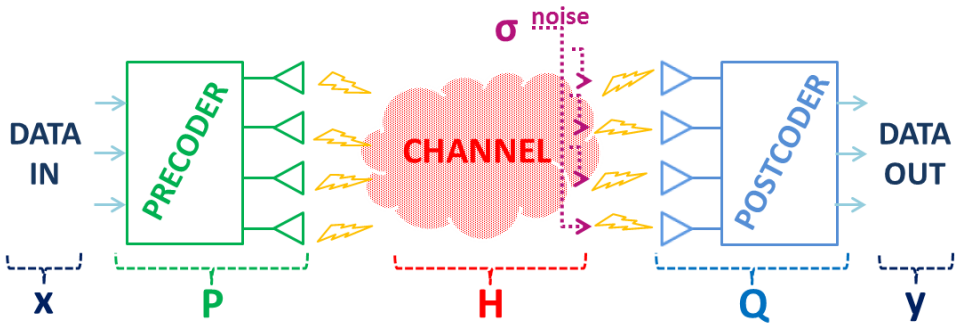

Figure C.1: Scheme of a generic multiplexing communication system

channel, i.e. the mathematical model of the physical medium where the EM waves propagate, can be described by a matrix $\mathbf{H} \in \mathbb{C}^{N_{Tx} \times N_{Rx}}$, where N_{Rx} is the number of receiving antennas. This

matrix is the core of the system; its (m, n)-elements characterize the relationship between the m-th antenna belonging to the Tx array and the n-th one of the Rx array. When modeling conventional MIMO systems, the elements of $\mathbf{H}$ are often assumed to be random variables, depending on the environment. Here, for simplicity, we assume that $\mathbf{H}$ is fully deterministic, and calculate its elements using the ray tracing method [105]. In other words, each antenna is modeled as a point source and the propagation factor between each antenna pair is calculated. Keeping in mind Friis equation, each element of $\mathbf{H}$ is equal to:

$$h_{m,n} = \frac{\lambda}{4\pi d_{m,n}} \exp\left(ikd_{m,n}\right) \tag{C.0.1}$$

where $d_{m,n}$ is the distance between the m-th and the n-th antennas of the Rx and Tx systems respectively while $k = 2\pi/\lambda$ is the wave-number. However, this model can be improved with a more accurate calculation of $\mathbf{H}$. Instead of considering the antennas as ideal isotropic sources it is possible to account for their gains, as depicted in Fig. C.2. In such a way, Eq. C.0.1 become:

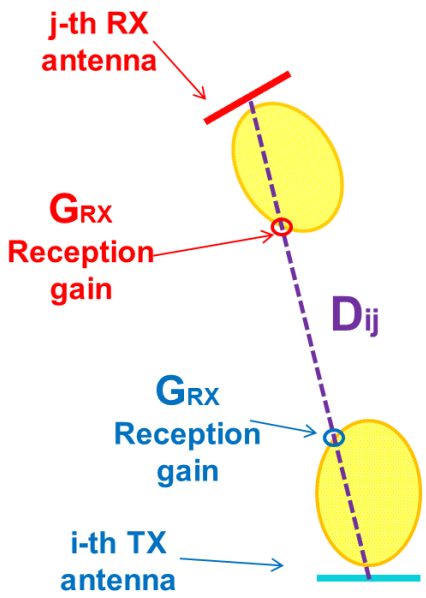

Figure C.2: Calculation of the $\mathbf{H}$ matrix using the ray tracing method and accounting for the antennas directivity. The yellow bubbles represent the antennas radiation pattern while the purple dashed line represents the ray connecting the i-th antenna belonging to the Tx array and the j-th one of the Rx array.

$$h_{m,n} = G_{TX} G_{RX} \frac{\lambda}{4\pi d_{m,n}} \exp\left(ikd_{m,n}\right) \tag{C.0.2}$$

Finally the postcoder, which processes (linearly) the signals from the receiving antenna and provides the output data streams, can also be described by a matrix, $\mathbf{Q} \in \mathbb{C}^{N_S \times N_{Rx}}$.

All these elements together yield the overall system equation:

$$\mathbf{y} = \mathbf{QHPx} + \mathbf{y_n} \tag{C.0.3}$$

where $\mathbf{y}_n$ is the vector of additive white noise to be accounted at the receiver input. If the system was ideal, $\mathbf{y}_n$ would be equal to zero, and the product of $\mathbf{Q}, \mathbf{H}$, and $\mathbf{P}$ would yield a unitary matrix; in such a case, perfect reception of the transmitted signals can be done and $\mathbf{y} = \mathbf{x}$. In other words, an ideal system is characterize by having $\mathbf{Q} = (\mathbf{HP})^{-1}$. This condition, clearly, is unrealistic.

In practice, one has to monitor the quality of each output stream evaluating, for each channel, the Signal to Noise and Interference Ratio (SNIR). The SNIR calculation of the *i*-th data stream can be expressed as:

$$\text{SNIR} = \frac{P_{st}}{P_{int} + P_n} \tag{C.0.4}$$

where P_{st} is the *i-th* data stream received power, and P_{int} and P_n are, the interference powers due to other data streams and to noise, respectively.

To determine the SNIR value of each data stream one can simply measure the powers required by Eq. C.0.4 and compute the ratio. On the contrary, an alternative and more interesting way can be followed. In fact, it is possible to calculate the SNIR values as a variation, Δ_{SNIR}, with respect to the Signal to Noise Ratio SNIR_0 of a Single Input Single Output (SISO) reference system. Pay attention that to exploit this trick it is important that both the examined and the reference links have the same length. Moreover, each data stream have to be transmitted with the same RF power P_{str}. To calculate the *i*-th Δ_{SNIR}, consider the structure of the matrix product $\mathbf{QHP} = \mathbf{K}$, and its role on the system behavior:

$$\begin{bmatrix} y_1 \\ y_2 \\ \vdots \\ y_{N_s} \end{bmatrix} = \begin{bmatrix} k_{11} & k_{12} & \cdots & k_{1N_s} \\ k_{21} & k_{22} & \cdots & k_{2N_s} \\ \vdots & \vdots & \ddots & \vdots \\ k_{N_s1} & k_{N_s2} & \cdots & k_{N_sN_s} \end{bmatrix} \begin{bmatrix} x_1 \\ x_2 \\ \vdots \\ x_{N_s} \end{bmatrix} \tag{C.0.5}$$

As can be observed , the power gain of the i-th data stream is equal to k_{ii}^2, while the interference power gain for the same stream is $\sum_{j \neq i}(k_{ij})^2$. To evaluate the noise power, on the contrary, it is necessary to account for two preliminary assumptions. First, assume that the noise input point is located in correspondence of the receiving antennas, (as for the reference SISO link). Second, assume that the noise contributions at different antennas are mutually uncorrelated and of equal powers σ^2. Examining the postcoder matrix $\mathbf{Q}$, the input-output relation for the noise is:

$$\begin{bmatrix} y_{n_1} \\ y_{n_2} \\ \vdots \\ y_{n_{N_s}} \end{bmatrix} = \begin{bmatrix} q_{11} & q_{12} & \cdots & q_{1N_s} \\ q_{21} & q_{22} & \cdots & q_{2N_s} \\ \vdots & \vdots & \ddots & \vdots \\ q_{N_s1} & q_{N_s2} & \cdots & q_{N_sN_s} \end{bmatrix} \begin{bmatrix} \sigma_1 \\ \sigma_2 \\ \vdots \\ \sigma_{N_s} \end{bmatrix} \tag{C.0.6}$$

Consequently, the noise power gain for the i-th data stream will be $\sum_{j=1}^{N_s}(q_{ij})^2$. Hence, the received power associated to the i-th data stream is equal to $P_s = P_{str}k_{ii}^2$. On the contrary, the

interference power is $P_i = P_{str} \sum_{j \neq i} k_{ij}^2$ and the noise power $P_n = \sigma^2 \sum_{j=1}^{N_s} q_{ij}^2$. Combining these quantities in Eq. C.0.4 and remembering that the SNR_0 of the reference SISO system is equal to $\text{SNR}_0 = P_{str}/\sigma^2$ it results that, for the i-th data stream, Δ_{SNIR} is equal to:

$$\Delta_{\text{SNIR}_{dB}} = 10Log_{10}\left(\frac{k_{ii}^2}{\text{SNIR}_0 \sum_{j \neq i} k_{ij}^2 + \sum_{j=1}^{N_s} q_{ij}^2}\right) \tag{C.0.7}$$

In the end, before concluding, let's point out what is meant as Channel State Information (CSI) MIMO. A CSI MIMO is a system where both the transmitter and the receiver are supposed to know the communication channel structure. In other words, both Tx and Rx know the structure of the $\mathbf{H}$ matrix. In such a way, it is possible to calculate the best configurations of $\mathbf{P}$ and $\mathbf{Q}$ matrices in order to have the best exploitation of the antennas configuration. To make this, it is sufficient to calculate the so-called Singular Value Decomposition [159] (SVD) of the channel matrix: $\mathbf{H} = \mathbf{U}\Sigma\mathbf{V}^H$ and to take the $\mathbf{U}$ matrix as the precoder. The $\mathbf{U}$ matrix, in fact, contains the natural radiation modes of the system that guarantee the lowest level of interference at the receiver. The postcoder matrix, on the contrary, must be taken equal to $\mathbf{U} = (\mathbf{HP})^{-1} = (\mathbf{HU})^{-1}$. In such a way, it is possible to have a perfect reception, without data stream mutual interference, since it results that: $\mathbf{y} = \mathbf{QHPx} + \mathbf{y_n} = \mathbf{Ix} + \mathbf{y_n}$.

Bibliography

[1] A. F. Molisch, *Wireless communications*, vol. 15. John Wiley & Sons, 2010.

[2] S. M. Mohammadi, L. K. Daldorff, J. E. Bergman, R. L. Karlsson, B. Thidé, K. Forozesh, T. D. Carozzi, and B. Isham, "Orbital angular momentum in radio - a system study," *Antennas and Propagation, IEEE Transactions on*, vol. 58, no. 2, pp. 565–572, 2010.

[3] G. Gibson, J. Courtial, M. Padgett, M. Vasnetsov, V. Pas' ko, S. Barnett, and S. Franke-Arnold, "Free-space information transfer using light beams carrying orbital angular momentum," *Optics Express*, vol. 12, no. 22, pp. 5448–5456, 2004.

[4] J. D. Jackson and J. D. Jackson, *Classical electrodynamics*, vol. 3. Wiley New York etc., 1962.

[5] L. Allen, M. W. Beijersbergen, R. Spreeuw, and J. Woerdman, "Orbital angular momentum of light and the transformation of laguerre-gaussian laser modes," *Physical Review A*, vol. 45, no. 11, p. 8185, 1992.

[6] D. L. Andrews and M. Babiker, *The angular momentum of light*. Cambridge University Press, 2012.

[7] S. Franke-Arnold, S. M. Barnett, E. Yao, J. Leach, J. Courtial, and M. Padgett, "Uncertainty principle for angular position and angular momentum," *New Journal of Physics*, vol. 6, no. 1, p. 103, 2004.

[8] Y. Yan, G. Xie, M. P. Lavery, H. Huang, N. Ahmed, C. Bao, Y. Ren, Y. Cao, L. Li, Z. Zhao, *et al.*, "High-capacity millimetre-wave communications with orbital angular momentum multiplexing," *Nature communications*, vol. 5, 2014.

[9] J. Wang, J.-Y. Yang, I. M. Fazal, N. Ahmed, Y. Yan, H. Huang, Y. Ren, Y. Yue, S. Dolinar, M. Tur, *et al.*, "Terabit free-space data transmission employing orbital angular momentum multiplexing," *Nature Photonics*, vol. 6, no. 7, pp. 488–496, 2012.

[10] M. Krenn, R. Fickler, M. Fink, J. Handsteiner, M. Malik, T. Scheidl, R. Ursin, and A. Zeilinger, "Communication with spatially modulated light through turbulent air across vienna," *New Journal of Physics*, vol. 16, no. 11, p. 113028, 2014.

[11] F. Tamburini, E. Mari, G. Parisi, F. Spinello, M. Oldoni, R. Ravanelli, P. Coassini, C. G. Someda, B. Thidé, and F. Romanato, "Tripling the capacity of a point-to-point radio link by using electromagnetic vortices," *Radio Science*, 2015.

[12] O. Edfors and A. J. Johansson, "Is orbital angular momentum (oam) based radio communication an unexploited area?," *Antennas and Propagation, IEEE Transactions on*, vol. 60, no. 2, pp. 1126–1131, 2012.

[13] T. K. Sarkar, R. J. Mailloux, A. A. Oliner, M. Salazar-Palma, and D. L. Sengupta, "The genesis of maxwell's equations," *History of Wireless*, pp. 189–214, 2006.

[14] H. Hertz, "Ueber sehr schnelle electrische schwingungen," *Annalen der Physik*, vol. 267, no. 7, pp. 421–448, 1887.

[15] O. E. Dunlap, *Marconi, the Man and his Wireless*. The Macmillan company, 1941.

[16] A. F. Molisch, *Wireless communications*. John Wiley & Sons, 2007.

[17] A. M. Yao and M. J. Padgett, "Orbital angular momentum: origins, behavior and applications," *Advances in Optics and Photonics*, vol. 3, no. 2, pp. 161–204, 2011.

[18] R. A. Beth, "Mechanical detection and measurement of the angular momentum of light," *Physical Review*, vol. 50, no. 2, p. 115, 1936.

[19] C. G. Someda, *Electromagnetic waves*. CRC Press, 2006.

[20] B. Thidé, *Electromagnetic field theory*. Upsilon Books Uppsala, 2004.

[21] B. Thidé, F. Tamburini, H. Then, C. Someda, E. Mari, G. Parisi, F. Spinello, and F. Romanato, "Angular momentum radio," in *SPIE OPTO*, pp. 89990B–89990B, International Society for Optics and Photonics, 2014.

[22] R. P. Feynman, R. B. Leighton, and M. Sands, *The Feynman Lectures on Physics, Desktop Edition Volume I*, vol. 1. Basic Books, 2013.

[23] C.-F. Li, "Spin and orbital angular momentum of a class of nonparaxial light beams having a globally defined polarization," *Physical Review A*, vol. 80, no. 6, p. 063814, 2009.

[24] S. M. Barnett and L. Allen, "Orbital angular momentum and nonparaxial light beams," *Optics communications*, vol. 110, no. 5, pp. 670–678, 1994.

[25] M. Abramowitz and I. A. Stegun, *Handbook of mathematical functions: with formulas, graphs, and mathematical tables*. No. 55, Courier Corporation, 1964.

[26] L. Allen and M. Padgett, "The orbital angular momentum of light: An introduction," *Twisted Photons: Applications of Light with Orbital Angular Momentum, First Edition*, pp. 1–12, 2011.

[27] M. Padgett and J. Courtial, "Poincaré-sphere equivalent for light beams containing orbital angular momentum," *Optics letters*, vol. 24, no. 7, pp. 430–432, 1999.

[28] G. Zhou, "Analytical vectorial structure of laguerre-gaussian beam in the far field," *Optics letters*, vol. 31, no. 17, pp. 2616–2618, 2006.

[29] H.-C. Kim and Y. H. Lee, "Hermite–gaussian and laguerre–gaussian beams beyond the paraxial approximation," *Optics communications*, vol. 169, no. 1, pp. 9–16, 1999.

[30] A. Cerjan and C. Cerjan, "Orbital angular momentum of laguerre–gaussian beams beyond the paraxial approximation," *JOSA A*, vol. 28, no. 11, pp. 2253–2260, 2011.

[31] B. E. Saleh, M. C. Teich, and B. E. Saleh, *Fundamentals of photonics*, vol. 22. Wiley New York, 1991.

[32] S. Feng and H. G. Winful, "Physical origin of the gouy phase shift," *Optics letters*, vol. 26, no. 8, pp. 485–487, 2001.

[33] T. Visser and E. Wolf, "The origin of the gouy phase anomaly and its generalization to astigmatic wavefields," *Optics Communications*, vol. 283, no. 18, pp. 3371–3375, 2010.

[34] P. Coullet, L. Gil, and F. Rocca, "Optical vortices," *Optics Communications*, vol. 73, no. 5, pp. 403–408, 1989.

[35] J. Nye, "The motion and structure of dislocations in wavefronts," in *Proceedings of the Royal Society of London A: Mathematical, Physical and Engineering Sciences*, vol. 378, pp. 219–239, The Royal Society, 1981.

[36] M. V. Berry, "Singularities in waves and rays," *Physics of Defects*, vol. 35, pp. 453–543, 1981.

[37] M. Berry, "Making waves in physics," *Nature*, vol. 403, no. 6765, pp. 21–21, 2000.

[38] J. Adachi and G.-o. Ishikawa, "Classification of phase singularities for complex scalar waves and their bifurcations," *Nonlinearity*, vol. 20, no. 8, p. 1907, 2007.

[39] M. A. Bandres, J. C. Gutiérrez-Vega, *et al.*, "Circular beams," *Optics letters*, vol. 33, no. 2, pp. 177–179, 2008.

[40] A. Bekshaev, M. Soskin, and M. Vasnetsov, "Paraxial light beams with angular momentum," *arXiv preprint arXiv:0801.2309*, 2008.

[41] J. C. Gutiérrez-Vega and C. López-Mariscal, "Nondiffracting vortex beams with continuous orbital angular momentum order dependence," *Journal of Optics A: Pure and Applied Optics*, vol. 10, no. 1, p. 015009, 2008.

[42] K. Volke-Sepulveda, V. Garcés-Chávez, S. Chávez-Cerda, J. Arlt, and K. Dholakia, "Orbital angular momentum of a high-order bessel light beam," *Journal of Optics B: Quantum and Semiclassical Optics*, vol. 4, no. 2, p. S82, 2002.

[43] M. Padgett and L. Allen, "The poynting vector in laguerre-gaussian laser modes," *Optics communications*, vol. 121, no. 1, pp. 36–40, 1995.

[44] L. Allen and M. Padgett, "The poynting vector in laguerre–gaussian beams and the interpretation of their angular momentum density," *Optics Communications*, vol. 184, no. 1, pp. 67–71, 2000.

[45] L. Torner, J. Torres, and S. Carrasco, "Digital spiral imaging," *Optics Express*, vol. 13, no. 3, pp. 873–881, 2005.

[46] L. E. Franks, *Signal theory*. Dowden & Culver, 1981.

[47] S. Zheng, X. Hui, J. Zhu, H. Chi, X. Jin, S. Yu, and X. Zhang, "Orbital angular momentum mode-demultiplexing scheme with partial angular receiving aperture," *Optics express*, vol. 23, no. 9, pp. 12251–12257, 2015.

[48] M. Vasnetsov, V. Pas' ko, and M. Soskin, "Analysis of orbital angular momentum of a misaligned optical beam," *New Journal of Physics*, vol. 7, no. 1, p. 46, 2005.

[49] J. Lin, X.-C. Yuan, M. Chen, and J. Dainty, "Application of orbital angular momentum to simultaneous determination of tilt and lateral displacement of a misaligned laser beam," *JOSA A*, vol. 27, no. 10, pp. 2337–2343, 2010.

[50] R. Martínez-Herrero and P. Mejías, "Angular momentum decomposition of nonparaxial light beams," *Optics express*, vol. 18, no. 8, pp. 7965–7971, 2010.

[51] M. Berry, "Optical vortices evolving from helicoidal integer and fractional phase steps," *Journal of Optics A: Pure and Applied Optics*, vol. 6, no. 2, p. 259, 2004.

[52] S. Oemrawsingh, J. Van Houwelingen, E. Eliel, J. Woerdman, E. Verstegen, J. Kloosterboer, G. t Hooft, *et al.*, "Production and characterization of spiral phase plates for optical wavelengths," *Applied optics*, vol. 43, no. 3, pp. 688–694, 2004.

[53] P. Schemmel, S. Maccalli, G. Pisano, B. Maffei, and M. W. R. Ng, "Three-dimensional measurements of a millimeter wave orbital angular momentum vortex," *Optics letters*, vol. 39, no. 3, pp. 626–629, 2014.

[54] E. Mari, G. Anzolin, F. Tamburini, M. Prasciolu, G. Umbriaco, A. Bianchini, C. Barbieri, and F. Romanato, "Fabrication and testing of l= 2 optical vortex phase masks for coronography," *Optics express*, vol. 18, no. 3, pp. 2339–2344, 2010.

[55] L. Cheng, W. Hong, and Z.-C. Hao, "Generation of electromagnetic waves with arbitrary orbital angular momentum modes," *Scientific reports*, vol. 4, 2014.

[56] F. Tamburini, E. Mari, A. Sponselli, B. Thidé, A. Bianchini, and F. Romanato, "Encoding many channels on the same frequency through radio vorticity: first experimental test," *New Journal of Physics*, vol. 14, no. 3, p. 033001, 2012.

[57] N. Heckenberg, R. McDuff, C. Smith, and A. White, "Generation of optical phase singularities by computer-generated holograms," *Optics letters*, vol. 17, no. 3, pp. 221–223, 1992.

[58] A. Bekshaev, O. Orlinska, and M. Vasnetsov, "Optical vortex generation with a fork hologram under conditions of high-angle diffraction," *Optics Communications*, vol. 283, no. 10, pp. 2006–2016, 2010.

[59] D. Gabor *et al.*, "A new microscopic principle," *Nature*, vol. 161, no. 4098, pp. 777–778, 1948.

[60] G. A. Deschamps, "Some remarks on radio-frequency holography," *Proceedings of the IEEE*, vol. 55, no. 4, pp. 570–571, 1967.

[61] E. Mari, *Optical Vortex diffractive optics for terrestrial and space applications*. Phd thesis, University of Padova, 2011/2012.

[62] U. Schnars and W. Jueptner, *Digital holography*. Springer, 2005.

[63] J. R. Vacca, *Holograms and Holography: Design, Techniques, and Commercial Applications*. Charles River Media, 2001.

[64] S. M. Mohammadi, L. K. Daldorff, K. Forozesh, B. Thidé, J. E. Bergman, B. Isham, R. Karlsson, and T. Carozzi, "Orbital angular momentum in radio: Measurement methods," *Radio Science*, vol. 45, no. 4, 2010.

[65] H. Wu, Y. Yuan, Z. Zhang, and J. Cang, "Uca-based orbital angular momentum radio beam generation and reception under different array configurations," in *Wireless Communications and Signal Processing (WCSP), 2014 Sixth International Conference on*, pp. 1–6, IEEE, 2014.

[66] B. Thidé, H. Then, J. Sjöholm, K. Palmer, J. Bergman, T. Carozzi, Y. N. Istomin, N. Ibragimov, and R. Khamitova, "Utilization of photon orbital angular momentum in the low-frequency radio domain," *Physical review letters*, vol. 99, no. 8, p. 087701, 2007.

[67] C. A. Balanis, *Antenna theory: analysis and design*, vol. 1. John Wiley & Sons, 2005.

[68] Q. Bai, A. Tennant, B. Allen, and M. U. Rehman, "Generation of orbital angular momentum (oam) radio beams with phased patch array," 2013.

[69] Q. Bai, A. Tennant, and B. Allen, "Experimental circular phased array for generating oam radio beams," *Electronics Letters*, vol. 50, no. 20, pp. 1414–1415, 2014.

[70] C. Deng, W. Chen, Z. Zhang, Y. Li, and Z. Feng, "Generation of oam radio waves using circular vivaldi antenna array," *International Journal of Antennas and Propagation*, vol. 2013, 2013.

[71] A. Tennant and B. Allen, "Generation of oam radio waves using circular time-switched array antenna," *Electronics letters*, vol. 48, no. 21, pp. 1365–1366, 2012.

[72] W. Wei, K. Mahdjoubi, C. Brousseau, and O. Emile, "Generation of oam waves with circular phase shifter and array of patch antennas," *Electronics Letters*, vol. 51, no. 6, pp. 442–443, 2015.

[73] X. Gao, S. Huang, J. Zhou, Y. Wei, C. Gao, X. Zhang, and W. Gu, "Generating, multiplexing/demultiplexing and receiving the orbital angular momentum of radio frequency signals using an optical true time delay unit," *Journal of Optics*, vol. 15, no. 10, p. 105401, 2013.

[74] X. Gao, S. Huang, Y. Song, S. Li, Y. Wei, J. Zhou, X. Zheng, H. Zhang, and W. Gu, "Generating the orbital angular momentum of radio frequency signals using optical-true-time-delay unit based on optical spectrum processor," *Optics letters*, vol. 39, no. 9, pp. 2652–2655, 2014.

[75] F. Bian, S. Li, Y. Song, Q. Yu, X. Gao, X. Zheng, H. Zhang, and B. Zhou, "Generation of wideband radio frequency signals carrying orbital angular momentum based on microwave photonics phase shifter," in *CLEO: QELS_Fundamental Science*, pp. JW2A–15, Optical Society of America, 2014.

[76] S. Zheng, X. Hui, X. Jin, H. Chi, and X. Zhang, "Transmission characteristics of a twisted radio wave based on circular traveling-wave antenna," *Antennas and Propagation, IEEE Transactions on*, vol. 63, no. 4, pp. 1530–1536, 2015.

[77] E. Karimi, B. Piccirillo, E. Nagali, L. Marrucci, and E. Santamato, "Efficient generation and sorting of orbital angular momentum eigenmodes of light by thermally tuned q-plates," *Applied Physics Letters*, vol. 94, no. 23, p. 231124, 2009.

[78] S. Slussarenko, A. Murauski, T. Du, V. Chigrinov, L. Marrucci, and E. Santamato, "Tunable liquid crystal q-plates with arbitrary topological charge," *Optics express*, vol. 19, no. 5, pp. 4085–4090, 2011.

[79] J. Courtial and M. Padgett, "Performance of a cylindrical lens mode converter for producing laguerre–gaussian laser modes," *Optics communications*, vol. 159, no. 1, pp. 13–18, 1999.

[80] M. Beijersbergen, L. Allen, H. Van der Veen, and J. Woerdman, "Astigmatic laser mode converters and transfer of orbital angular momentum," *Optical angular momentum*, vol. 96, pp. 123–132, 2003.

[81] G. Xie, L. Li, Y. Ren, H. Huang, Y. Yan, N. Ahmed, Z. Zhao, M. P. Lavery, N. Ashrafi, S. Ashrafi, *et al.*, "Performance metrics and design considerations for a free-space optical orbital-angular-momentum–multiplexed communication link," *Optica*, vol. 2, no. 4, pp. 357–365, 2015.

[82] A. Demeter and C.-Z. Kertesz, "Simulation of free-space communication using the orbital angular momentum of radio waves," in *Optimization of Electrical and Electronic Equipment (OPTIM), 2014 International Conference on*, pp. 846–851, IEEE, 2014.

[83] E. Cano, B. Allen, Q. Bai, and A. Tennant, "Generation and detection of oam signals for radio communications," in *Antennas and Propagation Conference (LAPC), 2014 Loughborough*, pp. 637–640, IEEE, 2014.

[84] C. Dieylar Diallo, D. K. Nguyen, A. Chabory, and N. Capet, "Estimation of the orbital angular momentum order using a vector antenna in the presence of noise," in *Antennas and Propagation (EuCAP), 2014 8th European Conference on*, pp. 3248–3252, IEEE, 2014.

[85] A. Haskou, P. Mary, and M. Hélard, "Error probability on the orbital angular momentum detection," in *IEEE 25th Annual International Symposium on Personal Indoor and Mobile Radio Communications (PIMRC) 2014*, pp. 1–5, 2014.

[86] L. J. Hornbeck, "Digital light processing for high-brightness high-resolution applications," in *Electronic Imaging'97*, pp. 27–40, International Society for Optics and Photonics, 1997.

[87] H. Huang, G. Xie, Y. Yan, N. Ahmed, Y. Ren, Y. Yue, D. Rogawski, M. J. Willner, B. I. Erkmen, K. M. Birnbaum, *et al.*, "100 tbit/s free-space data link enabled by three-dimensional multiplexing of orbital angular momentum, polarization, and wavelength," *Optics letters*, vol. 39, no. 2, pp. 197–200, 2014.

[88] J. Lin, X.-C. Yuan, and S. Tao, "Orbital angular momentum (oam) multiplexing in free-space optical data transfer," in *SPIE Optics+ Photonics*, pp. 630411–630411, International Society for Optics and Photonics, 2006.

[89] A. Gatto, M. Tacca, P. Martelli, P. Boffi, and M. Martinelli, "Free-space orbital angular momentum division multiplexing with bessel beams," *Journal of Optics*, vol. 13, no. 6, p. 064018, 2011.

[90] M. Krenn, R. Fickler, M. Fink, J. Handsteiner, M. Malik, T. Scheidl, R. Ursin, and A. Zeilinger, "Communication with spatially modulated light through turbulent air across vienna," *New Journal of Physics*, vol. 16, no. 11, p. 113028, 2014.

[91] N. Bozinovic, Y. Yue, Y. Ren, M. Tur, P. Kristensen, H. Huang, A. E. Willner, and S. Ramachandran, "Terabit-scale orbital angular momentum mode division multiplexing in fibers," *Science*, vol. 340, no. 6140, pp. 1545–1548, 2013.

[92] Y. Yue, Y. Yan, N. Ahmed, J.-Y. Yang, L. Zhang, Y. Ren, H. Huang, K. M. Birnbaum, B. Erkmen, S. Dolinar, *et al.*, "Mode properties and propagation effects of optical orbital angular momentum (oam) modes in a ring fiber," *Photonics Journal, IEEE*, vol. 4, no. 2, pp. 535–543, 2012.

[93] S. Li and J. Wang, "A compact trench-assisted multi-orbital-angular-momentum multi-ring fiber for ultrahigh-density space-division multiplexing (19 rings$\times$ 22 modes)," *Scientific reports*, vol. 4, 2014.

[94] F. Tamburini, E. Mari, B. Thidé, C. Barbieri, and F. Romanato, "Experimental verification of photon angular momentum and vorticity with radio techniques," *Applied Physics Letters*, vol. 99, no. 20, p. 204102, 2011.

[95] F. Tamburini, B. Thidé, V. Boaga, F. Carraro, M. del Pup, A. Bianchini, C. Someda, and F. Romanato, "Experimental demonstration of free-space information transfer using phase modulated orbital angular momentum radio," *arXiv preprint arXiv:1302.2990*, 2013.

[96] F. E. Mahmouli and S. D. Walker, "4-gbps uncompressed video transmission over a 60-ghz orbital angular momentum wireless channel," *Wireless Communications Letters, IEEE*, vol. 2, no. 2, pp. 223–226, 2013.

[97] X. Gao, S. Huang, Y. Wei, W. Zhai, W. Xu, S. Yin, J. Zhou, and W. Gu, "An orbital angular momentum radio communication system optimized by intensity controlled masks effectively: Theoretical design and experimental verification," *Applied Physics Letters*, vol. 105, no. 24, p. 241109, 2014.

[98] S. Koenig, D. Lopez-Diaz, J. Antes, F. Boes, R. Henneberger, A. Leuther, A. Tessmann, R. Schmogrow, D. Hillerkuss, R. Palmer, *et al.*, "Wireless sub-thz communication system with high data rate," *Nature Photonics*, vol. 7, no. 12, pp. 977–981, 2013.

[99] M. Salem, C. Caloz, *et al.*, "Precision orbital angular momentum (oam) multiplexing communication using a metasurface," in *Advanced Electromagnetic Materials in Microwaves and Optics (METAMATERIALS), 2013 7th International Congress on*, pp. 94–96, IEEE, 2013.

[100] D. K. Nguyen, O. Pascal, J. Sokoloff, A. Chabory, B. Palacin, and N. Capet, "Discussion about the link budget for electromagnetic wave with orbital angular momentum," in *Antennas and Propagation (EuCAP), 2014 8th European Conference on*, pp. 1117–1121, IEEE, 2014.

[101] M. Tamagnone, C. Craeye, and J. Perruisseau-Carrier, "Comment on reply to comment on encoding many channels on the same frequency through radio vorticity: first experimental test," *New Journal of Physics*, vol. 15, no. 7, p. 078001, 2013.

[102] M. Tamagnone, C. Craeye, and J. Perruisseau-Carrier, "Comment on encoding many channels on the same frequency through radio vorticity: first experimental test," *New Journal of Physics*, vol. 14, 2012.

[103] F. Tamburini, B. Thidé, E. Mari, A. Sponselli, A. Bianchini, and F. Romanato, "Reply to comment on encoding many channels on the same frequency through radio vorticity: first experimental test," *New Journal of Physics*, vol. 14, no. 11, p. 118002, 2012.

[104] M. Andersson, E. Berglind, and G. Björk, "Orbital angular momentum modes do not increase the channel capacity in communication links," *New Journal of Physics*, vol. 17, no. 4, p. 043040, 2015.

[105] J. R. Hampton, *Introduction to MIMO Communications*. Cambridge University Press, 2013.

[106] K. Willig, J. Keller, M. Bossi, and S. Hell, "Sted microscopy resolves nanoparticle assemblies," *New Journal of Physics*, vol. 8, no. 6, p. 106, 2006.

[107] S. Fürhapter, A. Jesacher, S. Bernet, and M. Ritsch-Marte, "Spiral phase contrast imaging in microscopy," *Optics Express*, vol. 13, no. 3, pp. 689–694, 2005.

[108] E. Mari, F. Tamburini, G. Swartzlander, A. Bianchini, C. Barbieri, F. Romanato, and B. Thidé, "Sub-rayleigh optical vortex coronagraphy," *Optics express*, vol. 20, no. 3, pp. 2445–2451, 2012.

[109] F. Tamburini, B. Thidé, G. Molina-Terriza, and G. Anzolin, "Twisting of light around rotating black holes," *Nature Physics*, vol. 7, no. 3, pp. 195–197, 2011.

[110] T. Kuga, Y. Torii, N. Shiokawa, T. Hirano, Y. Shimizu, and H. Sasada, "Novel optical trap of atoms with a doughnut beam," *Physical Review Letters*, vol. 78, no. 25, p. 4713, 1997.

[111] D. G. Grier, "A revolution in optical manipulation," *Nature*, vol. 424, no. 6950, pp. 810–816, 2003.

[112] S. Sato, M. Ishigure, and H. Inaba, "Optical trapping and rotational manipulation of microscopic particles and biological cells using higher-order mode nd: Yag laser beams," *Electronics letters*, vol. 27, no. 20, pp. 1831–1832, 1991.

[113] J. T. Barreiro, N. K. Langford, N. A. Peters, and P. G. Kwiat, "Generation of hyperentangled photon pairs," *Physical review letters*, vol. 95, no. 26, p. 260501, 2005.

[114] S. K. Goyal and T. Konrad, "Teleporting photonic qudits using multimode quantum scissors," *Scientific reports*, vol. 3, 2013.

[115] F. Tonolini, S. Chan, M. Agnew, A. Lindsay, and J. Leach, "Reconstructing high-dimensional two-photon entangled states via compressive sensing," *Scientific reports*, vol. 4, 2014.

[116] C. J. Sletten and P. Blacksmith, "The paraboloid mirror," *Applied Optics*, vol. 4, no. 10, pp. 1239–1251, 1965.

[117] J. R. Trinder, "Parabolic reflector," *patent*, vol. WO 2005/069443, 07 2005.

[118] "Alfoplus siae microelectonics equipment." `https://www.siaemic.com/index.php/products-services/telecomsystems/microwave-product-portfolio?id=279`. Accessed: 2015-06-05.

[119] R. G. Gallager, "Low-density parity-check codes," *Information Theory, IRE Transactions on*, vol. 8, no. 1, pp. 21–28, 1962.

[120] G. Parisi, E. Mari, F. Spinello, F. Romanato, and F. Tamburini, "Manipulating intensity and phase distribution of composite laguerre-gaussian beams," *Optics express*, vol. 22, no. 14, pp. 17135–17146, 2014.

[121] N. Benvenuto, R. Corvaja, T. Erseghe, and N. Laurenti, *Communication systems: fundamentals and design methods*. John Wiley, 2007.

[122] D. Zwillinger, *Table of integrals, series, and products*. Elsevier, 2014.

[123] W. H. Carter, "Spot size and divergence for hermite gaussian beams of any order," *Applied optics*, vol. 19, pp. 1027–1029, 1980.

[124] R. L. Phillips and L. C. Andrews, "Spot size and divergence for laguerre gaussian beams of any order," *Appl. Opt*, vol. 22, no. 5, pp. 643–644, 1983.

[125] V. Lakshminarayanan, M. L. Calvo, and T. Alieva, *Mathematical Optics: Classical, Quantum, and Computational Methods*. CRC Press, 2012.

[126] D. Dragoman, "I: The wigner distribution function in optics and optoelectronics," *Progress in Optics*, vol. 37, pp. 1–56, 1997.

[127] R. Simon and N. Mukunda, "Twisted gaussian schell-model beams," *JOSA A*, vol. 10, no. 1, pp. 95–109, 1993.

[128] K. Sundar, N. Mukunda, and R. Simon, "Coherent-mode decomposition of general anisotropic gaussian schell-model beams," *JOSA A*, vol. 12, no. 3, pp. 560–569, 1995.

[129] R. Simon, E. Sudarshan, and N. Mukunda, "Gaussian-wigner distributions in quantum mechanics and optics," *Physical Review A*, vol. 36, no. 8, pp. 3868–3880, 1987.

[130] M. A. Alonso, "Wigner functions in optics: describing beams as ray bundles and pulses as particle ensembles," *Advances in Optics and Photonics*, vol. 3, no. 4, pp. 272–365, 2011.

[131] Y. A. Anan'ev and A. Y. Bekshaev, "Theory of intensity moments for arbitrary light beams," *Optics and spectroscopy*, vol. 76, pp. 558–568, 1994.

[132] A. Y. Bekshaev, "Intensity moments of a laser beam formed by superposition of hermite-gaussian modes," *Fotoelektronika*, vol. 8, pp. 2–13, 1999.

[133] R. Simon and G. Agarwal, "Wigner representation of laguerre–gaussian beams," *Optics letters*, vol. 25, no. 18, pp. 1313–1315, 2000.

[134] A. Cámara and T. Alieva, "Second order moments of superpositions of hermite-laguerre-gauss modes," *Session 2A5 Phase-Space Optics*, p. 279, 2010.

[135] J. Alda, "Laser and gaussian beam propagation and transformation," *Encyclopedia of optical engineering*, pp. 999–1013, 2003.

[136] S. Baumann, D. Kalb, L. MacMillan, and E. Galvez, "Propagation dynamics of optical vortices due to gouy phase," *Optics Express*, vol. 17, no. 12, pp. 9818–9827, 2009.

[137] T. Ando, N. Matsumoto, Y. Ohtake, Y. Takiguchi, and T. Inoue, "Structure of optical singularities in coaxial superpositions of laguerre–gaussian modes," *JOSA A*, vol. 27, no. 12, pp. 2602–2612, 2010.

[138] N. Matsumoto, T. Ando, T. Inoue, Y. Ohtake, N. Fukuchi, and T. Hara, "Generation of high-quality higher-order laguerre-gaussian beams using liquid-crystal-on-silicon spatial light modulators," *JOSA A*, vol. 25, no. 7, pp. 1642–1651, 2008.

[139] G. Ruffato, M. Massari, and F. Romanato, "Generation of high-order laguerre–gaussian modes by means of spiral phase plates," *Optics letters*, vol. 39, no. 17, pp. 5094–5097, 2014.

[140] E. Karimi, R. Boyd, P. de la Hoz, H. de Guise, J. Řeháček, Z. Hradil, A. Aiello, G. Leuchs, and L. L. Sánchez-Soto, "Radial quantum number of laguerre-gauss modes," *Physical Review A*, vol. 89, no. 6, p. 063813, 2014.

[141] J. W. Goodman, *Introduction to Fourier optics*. Roberts and Company Publishers, 2005.

[142] J. Arlt, R. Kuhn, and K. Dholakia, "Spatial transformation of laguerre–gaussian laser modes," *journal of modern optics*, vol. 48, no. 5, pp. 783–787, 2001.

[143] H. Yanai, K. Takeuchi, and Y. Takane, *Projection Matrices, Generalized Inverse Matrices, and Singular Value Decomposition*. Springer New York, 2011.

[144] G. Vallone, "On the properties of circular beams: normalization, laguerre–gauss expansion, and free-space divergence," *Optics letters*, vol. 40, no. 8, pp. 1717–1720, 2015.

[145] A. E. Siegman, "Lasers. mill valley," 1986.

[146] A. Wünsche, "Generalized gaussian beam solutions of paraxial optics and their connection to a hidden symmetry," *JOSA A*, vol. 6, no. 9, pp. 1320–1329, 1989.

[147] J. C. Gutiérrez-Vega, M. A. Bandres, *et al.*, "Helmholtz–gauss waves," *JOSA A*, vol. 22, no. 2, pp. 289–298, 2005.

[148] M. A. Khamsi and W. A. Kirk, *An introduction to metric spaces and fixed point theory*, vol. 53. John Wiley & Sons, 2011.

[149] G. C. Corazza, A. Manimpietri, and C. Montebello, *Circuiti a microonde*. R. Patron, 1965.

[150] T. Chu, "Geometrical representation of gaussian beam propagation," *Bell System Technical Journal*, vol. 45, no. 2, pp. 287–299, 1966.

[151] C. G. Someda, *Electromagnetic waves*. CRC Press, 2010.

[152] Y. Zhang, W. Feng, and N. Ge, "On the restriction of utilizing orbital angular momentum in radio communications," in *Communications and Networking in China (CHINACOM), 2013 8th International ICST Conference on*, pp. 271–275, IEEE, 2013.

[153] P. Schemmel, G. Pisano, and B. Maffei, "A modular spiral phase plate design for orbital angular momentum generation at millimetre wavelengths," *Optics express*, vol. 22, no. 12, pp. 14712–14726, 2014.

[154] F. E. Mahmouli and S. Walker, “Orbital angular momentum generation in a 60ghz wireless radio channel,” in *Telecommunications Forum (TELFOR), 2012 20th*, pp. 315–318, IEEE, 2012.

[155] F. Ricci, W. Löffler, and M. van Exter, “Instability of higher-order optical vortices analyzed with a multi-pinhole interferometer,” *Optics express*, vol. 20, no. 20, pp. 22961–22975, 2012.

[156] P. C. Chaumet, “Fully vectorial highly nonparaxial beam close to the waist,” *JOSA A*, vol. 23, no. 12, pp. 3197–3202, 2006.

[157] O. E. Gawhary and S. Severini, “Degree of paraxiality for monochromatic light beams,” *Optics letters*, vol. 33, no. 12, pp. 1360–1362, 2008.

[158] P. Vaveliuk, B. Ruiz, and A. Lencina, “Limits of the paraxial approximation in laser beams,” *Optics letters*, vol. 32, no. 8, pp. 927–929, 2007.

[159] C. D. Meyer, *Matrix analysis and applied linear algebra*. Siam, 2000.

List of Figures

List of Tables